Study of Advanced TiO_2-based Materials towards Superior Photocatalytic Properties

（高活性酸化チタン光触媒の研究開発）

Hua XU

Photo Functional Materials Chemistry Laboratory

Graduate School of Chemical Sciences and Engineering

Hokkaido University

2013

CONTENTS

Abstract

Semiconductor photocatalysis has attracted considerable attention as a promising solution to the environmental pollution and energy crisis. Among the various photocatalysts, TiO_2 has been proven to be the benchmark photocatalyst because of its superior photoreactivity, nontoxicity, long-term stability, low cost, and environmental friendly features. Nevertheless, there are still some limitations in the aspects of light absorption, charge recombination, and surface reactivity for TiO_2 photocatalysis, which need to be further improved for the practical application.

In this thesis, the topic is design and development of advanced TiO_2 based materials for the superior photocatalytic properties via enhancing the light absorption, charge separation, and surface reactivity. Firstly, via adopting Mie's scattering effect into the light absorption region of TiO_2, the light utilization efficiency is largely enhanced, accompanied with higher activity in H_2 evolution. Next, to enhance the charge separation efficiency, Cu_2O/TiO_2 nanojunction material is fabricated; this material exhibits much higher photocatalytic activity than pure TiO_2 because of its modified nanojunction structure. Furthermore, considering many physical and chemical processes take place on the surface of TiO_2 in the photocatalytic reaction, TiO_2 single crystals exposed with high-active facets are prepared; via optimization of the surface reactivity, the photocatalytic performance is largely enhanced.

Chapter 1 provides an overview of the photocatalysis, photocatalytic water splitting, CO_2 photoreduction. This chapter also summarizes the TiO_2 based photocatalysis, and strategies of achieving high photocatalytic activities for TiO_2.

In Chapter 2, to enhance the light utilization efficiency, a novel strategy of coupling

Mie's scattering effect into the light-absorption region of TiO_2 was developed. TiO_2 spheres with different diameters (330-750 nm) were controllably fabricated. It was found that both the scattering effect and the photocatalytic activity vary with the size of the TiO_2 spheres. Among them, TiO_2 spheres with diameter of 380 nm exhibited the highest photocatalytic activity, which is attributed to its highly efficient scattering happened in the light-absorption region of TiO_2 ($\lambda < 387$ nm).

In Chapter 3, to enhance the charge separation efficiency, porous-structured Cu_2O/TiO_2 nanojunction materials were successfully fabricated. The well-designed nanojunction structure between Cu_2O and TiO_2 is beneficial for the charge separation. In parallel, the porous structure of the material can facilitate the CO_2 adsorption and offer more reaction active sites. Thus, both the charge separation efficiency and the CO_2 adsorption simultaneously enhanced, leading to the excellent photocatalytic performance in the CO_2 photoreduction.

In Chapter 4, anatase TiO_2 nanosheets with 95% active {100} facets exposed and a relatively large surface area of 57.1 m^2/g were successfully prepared. This percentage (95%) is the highest among previously reported {100} facet exposed anatase TiO_2. Both the higher percentage of exposed {100} facets and larger surface area can offer more surface active sites in the photocatalytic reaction. On the other hand, the superior electronic band structure which is resulted from the higher percentage of {100} facet is also beneficial for the higher activity in both H_2 evolution and CO_2 photoreduction.

In Chapter 5, for the first time, {111} facet exposed anatase TiO_2 single crystals were prepared via both F^- and ammonia as the capping reagents. In comparison with the intensively investigated {001}, {100}, and {101} facets for anatase TiO_2, {111} facet owns a much higher surface energy of 1.61 J/m^2 and more under-coordinated Ti and O

atoms, in addition with a superior electronic structure. Both the superior surface atomic structure and electronic band structure make the great contribute to the marked photocatalytic activity.

Chapter 6 summarizes the importance and originality of this research, and provides future prospects of this work. This thesis revealed that the photocatalytic properties of TiO_2 are largely affected by the light absorption, charge separation, and surface reactivity. Mie's scattering effect happened in the light absorption region of TiO_2 can greatly enhance the light utilization efficiency in the H_2 evolution. Porous-structured nanojunction material is beneficial for both the charge separation efficiency and CO_2 adsorption in the CO_2 photoreduction test. Furthermore, fabrication of TiO_2 single crystals with high-active crystal facet exposed can largely promote the surface reactivity and offer more reaction sites in the photocatalytic reaction, is proved to be an effective approach to achieve advanced and excellent performance over photocatalysts.

Chapter 1 Introduction

1.1 Photocatalysis

Semiconductor photocatalysis has attracted considerable attention as a promising solution to the worldwide energy shortage and environmental pollution.[1] The prospective applications of photocatalysis are mainly in the following aspects: photocatalytic splitting water into hydrogen,[2] photoreduction of CO_2 into hydrocarbons,[3] photodecomposition of hazardous substances,[4] photocatalytically induced super-hydrophilicity,[5-7] and photoelectrochemical conversion,[8] etc.

In general, as shown in Figure 1.1, the semiconductor photocatalysis cycle comprises three steps: firstly, light illumination induces a transition of electrons (e^-) from the valence band (VB) to the conduction band (CB), leaving an equal number of holes (h^+); then, the excited electrons and holes migrate to the surface of the photocatalyst; finally, they react with the adsorbed electron acceptors and electron donors, respectively, to finish the whole photocatalytic reaction.[9-11] To give a better understanding, we will discuss every step of the photocatalytic reaction process in detail as below:

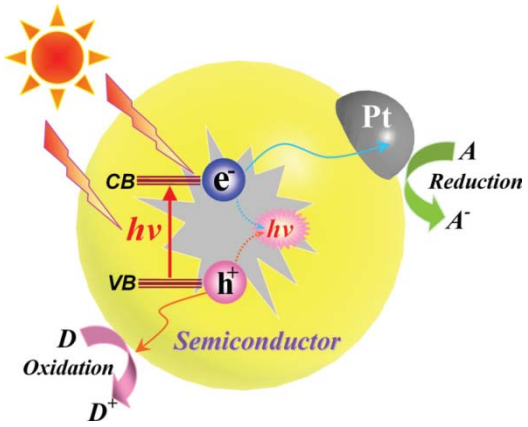

Figure 1.1 Schematic illustration of the basic mechanism of the semiconductor photocatalytic reaction process. Reproduced from Ref. 9.

Firstly, light excitation. When the energy of the incident light matches or exceeds the band gap of semiconductor photocatalyst, the light absorption and the consequent photoexcitation of electron-hole pairs take place. Initially, the energy of the incident photons is stored in the semiconductor by photoexcitation; it is then converted into chemical form by a series of electronic processes and surface/interface reactions. In contrast to the thermodynamics of conventional catalysis, not only spontaneous reactions ($\Delta G < 0$, ΔG means the Gibbs free energy) but also non-spontaneous reactions ($\Delta G > 0$) can be promoted by photocatalysis. In the former case, the input energy is used to overcome the activation barrier so as to facilitate photocatalysis at an increased rate or under milder conditions. In the latter case, part of the input high energy is converted into chemical energy that is accumulated in the reaction products.[9] In the real photocatalytic reaction, more photons absorb by the photocatalyst, more charge carriers (e^--h^+) can be photogenerated. In order to make semiconductor photocatalyst absorb more light or photons, one is to modify the electronic structure of the photocatalyst to extend its light absorption region via doping;[4,12] another way is to improve the light utilization efficiency via the spatial structuring[13] (e.g. stop-band effect in the photonic crystals,[8] and multiple reflections of light in the unique sphere-in-sphere chamber structure[14]).

Secondly, charge migration. The photogenerated electrons and holes need to transfer to the surface of the photocatalyst to take part in the photocatalytic reaction. However, a large proportion of charge carriers (e^--h^+ pairs) recombine together in the bulk or surface, dissipating the input energy in the form of heat or emitted light. To prevent the recombination of electron-hole pairs, the approach that has been applied generally is to load co-catalysts such as Pt, Pd, and RuO_2 on the semiconductor surface. The junctions

which are formed between the host semiconductor and the co-catalyst provide an internal electric field that facilitates the charge separation and induces faster carrier migration. Moreover, those co-catalysts exhibit better conductivity, lower over-potential, and higher catalytic activity than the host semiconductor, thus they can act as ideal active sites for photocatalytic reaction to proceed.[9] Besides loading co-catalyst on the surface of semiconductor photocatalyst, fabrication of composite photocatalysts is another effective method to enhance the charge separation efficiency, such as TiO_2/CdS,[15] TiO_2/Ag_3PO_4,[16] TiO_2/Cu_2O,[17] and so on.

Thirdly, photo-oxidation/reduction process. Herein, the mechanism of three kinds of photocatalytic reaction will be described as follows.

Ⅰ) IPA (isopropyl alcohol) photo-oxidization. Firstly, $h^+ + OH^- \rightarrow {}^{\bullet}OH$, or $h^+ + H_2O \rightarrow {}^{\bullet}OH + H^+$; $e^- + O_2 \rightarrow O_2^{\bullet-}$, $O_2^{\bullet-} + H^+ \rightarrow HO_2^{\bullet}$; then, the generated ${}^{\bullet}OH$ radical reacts with IPA, abstracting its hydrogen atom to form a radical: $CH_3CH(OH)CH_3 + {}^{\bullet}OH \rightarrow CH_3C{\bullet}(OH)CH_3 + H_2O$; finally, this $CH_3C{\bullet}(OH)CH_3$ radical is decompsoed to acetone through several reaction pathways, such as $CH_3C{\bullet}(OH)CH_3 \rightarrow CH_3COCH_3 + H^+ + e^-$.[4]

Ⅱ) Photocatalytic splitting of water. $2H^+ + 2e^- \rightarrow H_2$ (E^0_{red} = 0 V vs. NHE) or $2H_2O + 4h^+ \rightarrow O_2 + 4H^+$ (E^0_{ox} = 1.23 V vs. NHE); thus, the total amount of H_2 or O_2 evolution is primarily determined by the amount of excited electrons or holes in the water/photocatalyst interface, respectively.[18-20]

Ⅲ) CO_2 Photoreduction. The photogenerated holes in the valence band oxidize water to produce hydrogen ions ($H_2O + 2h^+ \rightarrow 1/2\ O_2 + 2H^+$, E^0_{ox} = 1.23 V vs. NHE), and the photogenerated electrons in the conduction band reduce CO_2 into CH_4 ($CO_2 + 8e^- + 8H^+ \rightarrow CH_4 + 2H_2O$, E^0_{red} = - 0.24 V vs. NHE);[3,21,22] More reductive of the electrons, more solar fuels (e.g. CH_4) can be generated. In my PhD study, I focus on the latter two

topics: photocatalytic H_2 evolution and CO_2 photoreduction.

1.2 Photocatalytic Water Splitting

Hydrogen (H_2) is considered to be a promising energy carrier because of its high energy capacity and environmental friendliness.[23,24] To date, the dominant technology for direct H_2 production is steam reforming from hydrocarbons (such as fossil fuels and biomass). Specifically, bulk H_2 (95% of the total production amounts) is usually produced by the steam reforming of methane or natural gas at high temperatures (700-1100 ^oC)[25]: 1) $CH_4 + H_2O \rightarrow CO + 3H_2$ +191.7 kJ/mol, 2) $CO + H_2O \rightarrow CO_2 + H_2$ -40.4 kJ/mol.[26] However, this method requires much higher reaction temperature and is considered to be heavily energy-exhausting.[27-29] Electrolysis is another way to produce H_2, in which the solid oxide electrolysis cells (SOEC's) operate at high temperature (around 800 ^oC), alkaline electrolysis cells (AEC's) work at high concentrated alkaline electrolyte (KOH or K_2CO_3) and the temperature of 200 ^oC, while polymer electrolyte membrane cells (PEM) can be conducted below 100 ^oC thus becoming more commercial. However, all those electrolysis process requires large amounts of electrical energy. Therefore, it is eager to pursue some environmental-friendly and low-cost strategy to obtain hydrogen.

In comparison, photocatalytic water splitting might be a promising way to produce hydrogen from solar energy. In 1972, Fujishima and Honda discovered the hydrogen evolution through the photoelectrochemical splitting of water on n-type TiO_2 electrode under UV-visible light irradiation.[18] The schematic illustration of the electrochemical cell is shown in Figure 1.2. It is consisting of an n-type TiO_2 anode and a Pt black cathode. When the surface of TiO_2 electrode was irradiated by the UV light from a 500

W Xe lamp, O_2 evolution occurred at the TiO_2 anode under applying of some bias. Concomitant reduction led to the H_2 evolution at the Pt counter electrode. This important discovery, which emerged from the use of photoelectrochemical cells with semiconductor electrodes, later inspired Bard to design the photocatalytic system by using semiconductor particles or powders as photocatalysts.[30-32] In my PhD study, I focus on the semiconductor powders as the photocatalysts in the photocatlaytic reaction system.

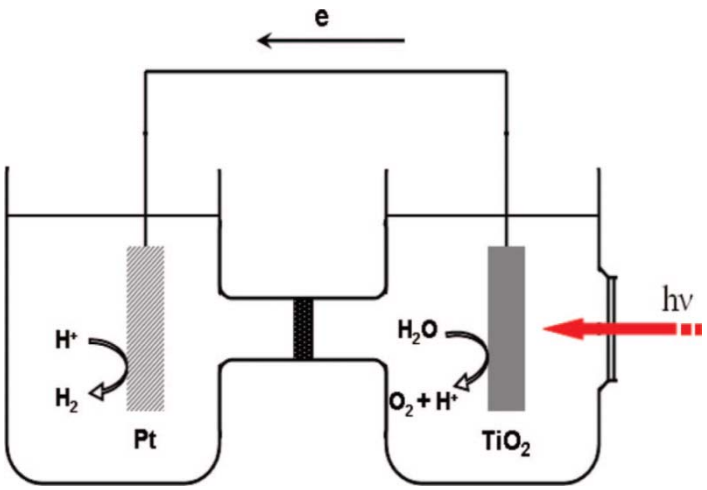

Figure 1.2 Schematic illustration of the photoelectrochemical cell (PEC). Reproduced from Ref. 18, 33.

Water splitting into H_2 and O_2 is an uphill reaction. It requires the standard Gibbs free energy charge ΔG^0 of 237 kJ/mol or 1.23 eV, as shown in eq 1.

$$H_2O \rightarrow \frac{1}{2} O_2 + H_2; \Delta G = +237 \text{ kJ/mol} \qquad (1)$$

Therefore, the band gap energy (E_g) of the photocatalyst should be > 1.23 eV ($\lambda <$ 1000 nm) to realize water splitting.[33] To facilitate both the reduction and oxidation of H_2O by the photoexcited electrons and holes, respectively, the match of the band gap

and the potentials of the conduction/valence bands are important. Particularly, for a semiconductor photocatalyst, the bottom level of the conduction band should be more negative than the reduction potential of H^+/H_2 (0 V vs. NHE), whereas the top level of the valence band should be more positive than the oxidation potential of O_2/H_2O (1.23 V).

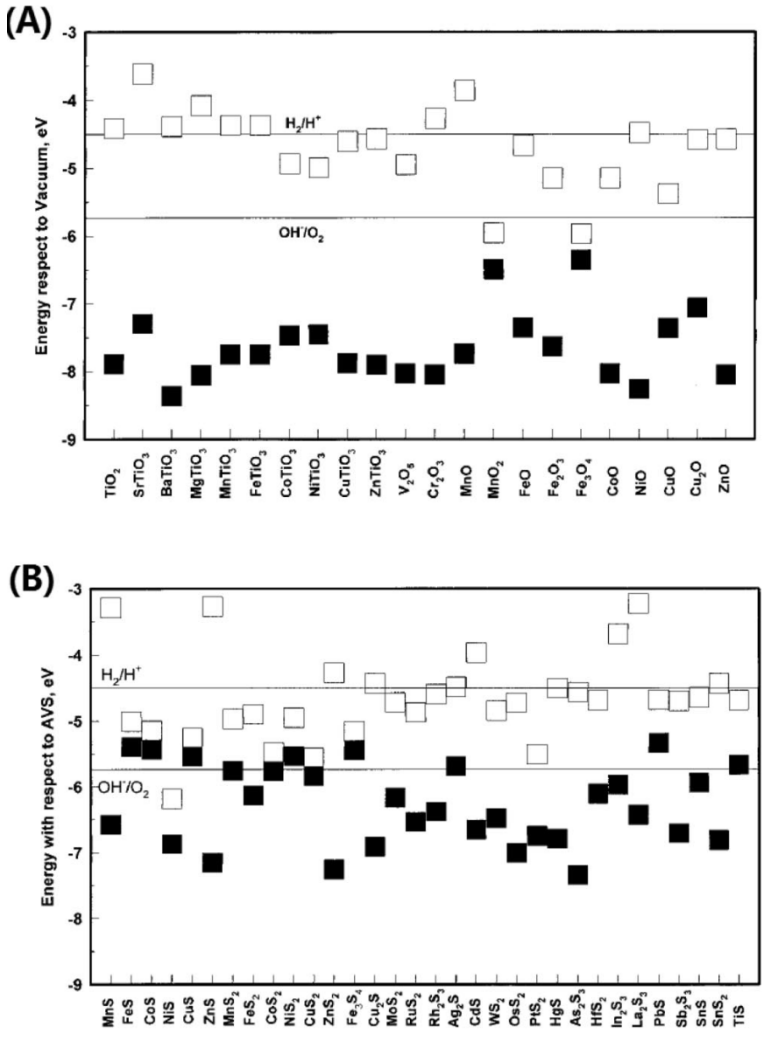

Figure 1.3 Calculated energy positions of conduction band edges and valence band edges at pH = 0 for selected semiconductors. The bottom of open squares represent conduction band edges, and the top of solid squares represent valance band edges. The solid lines indicate water stability limits. Reproduced from Ref. 33, 34.

Figure 1.3 shows the conduction band edge and valence band edge of some semiconductor photocatalyst candidates.[34] There are many semiconductor materials whose electronic structures match well with the redox potential of water into H_2 and O_2. However, the band structure requirement is only the thermodynamic requirement for water splitting. Other factors, such as over-potentials, charge separation, mobility, and lifetime of photogenerated electrons and holes, can also affect the photocatalytic water splitting.[33]

1.2.1 Overall Water Splitting

The phenomenon of overall water (vapor) splitting over photocatalyst powders were firstly reported on Pt-TiO_2 by Sato et al.[35] and NiO-$SrTiO_3$ by Domen et al.[36] in 1980. In the former work, Pt-TiO_2 exhibits little activity because of the rapid water formation from H_2 and O_2 ($H_2 + O_2 \rightarrow H_2O$); thus, both the adsorption of water molecular on the surface of Pt-TiO_2 photocatalyst and the suppression of the back reaction ($H_2 + O_2 \rightarrow H_2O$) on Pt site are essential for the H_2/O_2 evolution. To solve this problem, Sato et al. used NaOH coating on Pt-TiO_2, it is believed that NaOH can suppress the H_2-O_2 recombination on Pt site and hold water molecules on the surface of the photocatalyst.[37] Later, since the reaction rate in aqueous solution is faster than that in gaseous phase, more and more reaction system is designed in the aqueous solution. It is marked that Domen et al. adopted the aqueous solution system to split water on NiO-$SrTiO_3$ in 1982, and the photocatalytic activity is largely enhanced in the NaOH solution.[38]

After that, many efforts have been concentrated on the pure water splitting. In 1989, Kudo and his co-workers found that $K_4Nb_6O_{17}$ with an ion-exchangeable layered structure can evolve H_2 and O_2 at different layers.[39] In 2000, a series of layered

perovskite tantalite $RbLnTa_2O_7$ (Ln = La, Pr, Nd, and Sm) were developed to split water into stoichiometric H_2/O_2 mixtures, and the H_2/O_2 evolution rate are largely dependent on the lanthanoids in the sequence of La ≈ Pr « Sm < Nd, indicating that the partly filled 4f shells play important roles in the photocatalytic activity.[40] However, all those reported photocatalyst can only be excited by the ultraviolet (UV) light, which accounts for 5% of the incoming solar spectrum as shown in Figure 1.4.

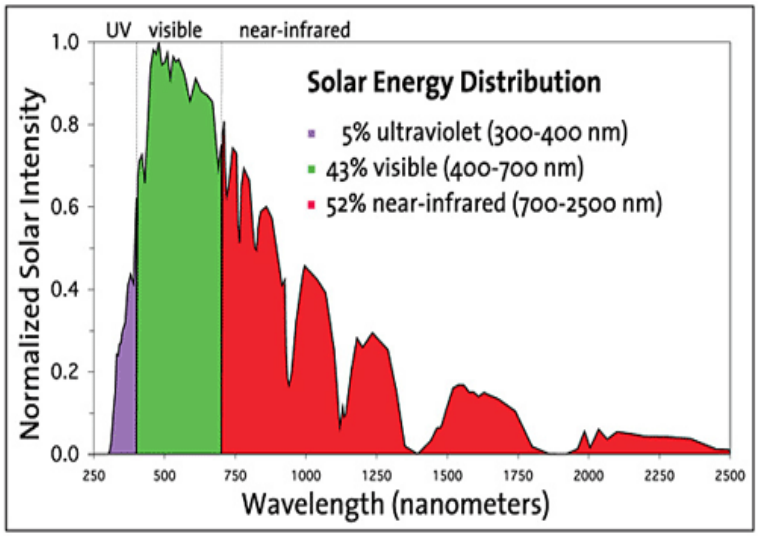

Figure 1.4 The distribution spectra of the solar energy.

To achieve a high utilization efficiency of visible light (about 43% of the solar energy), a breakthrough had been made by Zou and Ye in 2001, who firstly reported that doping of indium-tantalum-oxide with nickel yields a series of photocatalyst ($In_{1-x}Ni_xTaO_4$ (x = 0-0.2)) for the direct splitting of water into stoichiometric amounts of O_2 and H_2 under visible light irradiation with a quantum yield of 0.66%. Over the past decade, several photocatalysts have been successfully developed for the pure water splitting, such as NiO loaded $NaTaO_3$,[41] La_2TiO_7,[42] RuO_2-Ge_3N_4,[43] and $(Ga_{1-x}Zn_x)(N_{1-x}O_x)$ et al. Among which, $(Ga_{1-x}Zn_x)(N_{1-x}O_x)$ exhibits steady and

stoichiometric H_2 and O_2 evolution under visible light (λ > 400 nm), thus attracted much attention recently.[44,45] However, the maximum quantum efficiency obtained over the $Rh_{2-y}Cr_yO_3/(Ga_{1-x}Zn_x)(N_{1-x}O_x)$ is ca. 5.9% at 420-440 nm, which can not satisfy the practical application. Most importantly, the pure water splitting requires the semiconductor photocatalysts meet the rigid limitations of the band potentials in both the conduction band (more negative than E^0_{red} = 0 V vs. NHE) and the valence band (more positive than E^0_{ox} = 1.23 V vs. NHE), such kind of semiconductor is rarely to obtain.

1.2.2 Z-Scheme System Overall Water Splitting

The biomimetic Z-scheme system mechanism using reversible redox mediators has also been investigated for the overall water splitting.[46] The Z-scheme system requires to couple a first photocatalyst for H_2 generation and another photocatalyst for O_2 evolution with an electron mediator.[47] The photocatalysts which either meet the conduction band potentials for H_2 production or the valence band potentials for O_2 evolution is possible to be used in the Z-scheme system. Therefore, different from the pure water splitting, it has more options to choose the semiconductor photocatalysts.

In 1998, Fujihara et al. constructed a Z-scheme water splitting system over TiO_2 with two mediators (Br_2/Br^- and Fe^{3+}/Fe^{2+}), in which the reduction of water to H_2 using Br^- ions, and oxidation of water into O_2 using Fe^{3+} ions. The H_2 and O_2 evolution were carried out in separated compartments and combined via Pt electrodes and cation-exchange membranes, thus the back-reactions were largely prevented.[48] Later, in 2001, Abe et al. used newly designed Z-scheme system by a two-step photoexcitation system composed of a IO_3^-/I^- shuttle redox mediator (NaI aqueous suspension with pH =

11) and two different TiO_2 photocatalysts: Pt-loaded anatase TiO_2 for H_2 evolution and rutile TiO_2 for O_2 evolution as shown in Figure 1.5.[49]

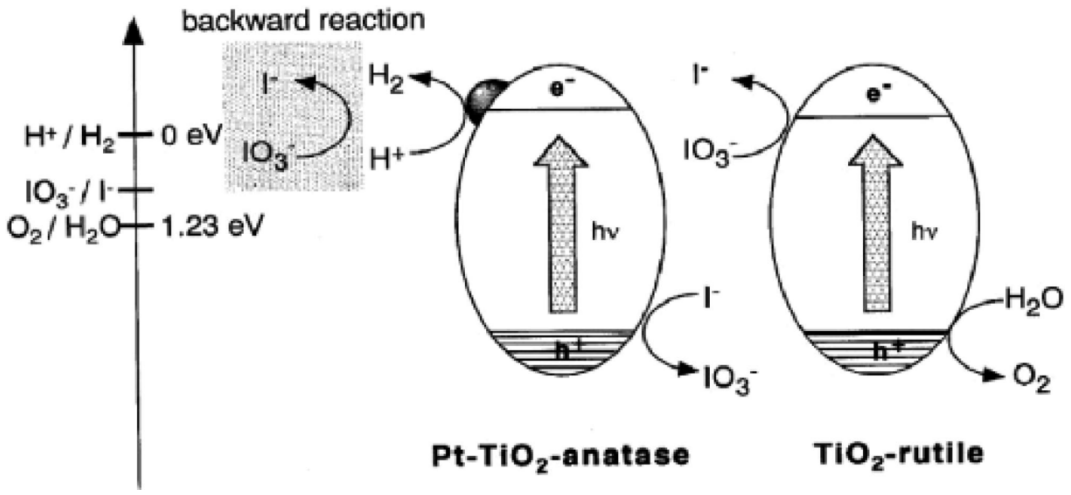

Figure 1.5 Proposed photocatalytic reaction mechanism for Z-scheme water-splitting system using an IO_3^-/I^- redox mediator and a mixture of Pt-TiO_2-antase and TiO_2-rutile photocatalysts. Reproduced from Ref. 49.

After that, more Z-scheme overall water-spitting system have been reported to evolve H_2 and O_2.[50] In 2010, Maeda et al. reported that a quantum efficiency of ca. 6.3% at 420.5 nm was achieved over the (Pt/ZrO_2-TaON)-(Pt/WO_3)-(IO_3^-/I^-) system for the overall water splitting as shown in Figure 1.6.[51] However, with the Z-scheme, every two photons are used to complete one electron reaction, thus the light utilization efficiency is quite low. Meanwhile, in the real photoreaction process, parts of the photogenerated electrons and holes will react with the redox mediator directly; those competition reactions will decrease the amounts of charge carriers to split water to some extent, thus resulting in lower quantum efficiency.

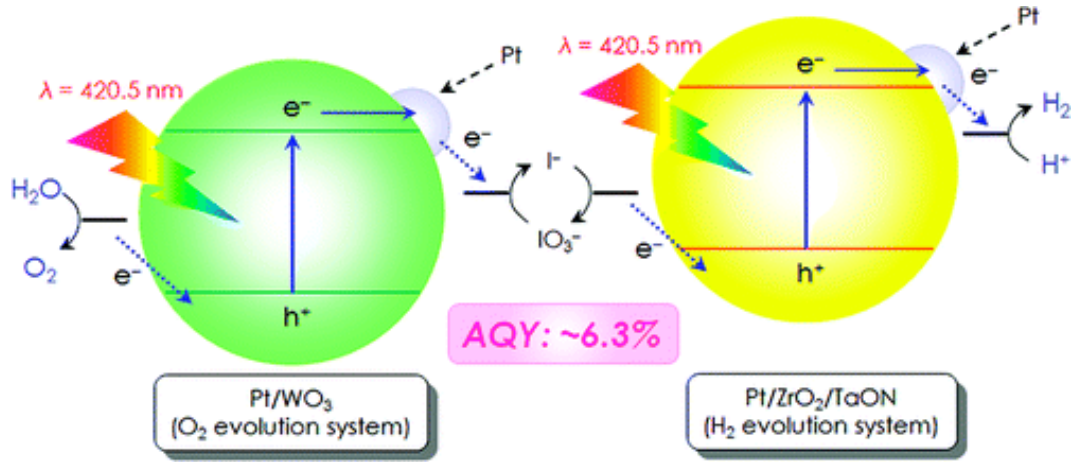

Figure 1.6 Schematic illustration of the water splitting process using the Z-scheme photocatalysis system. Reproduced from Ref. 51.

1.2.3 Water Splitting with Sacrificial Reagents

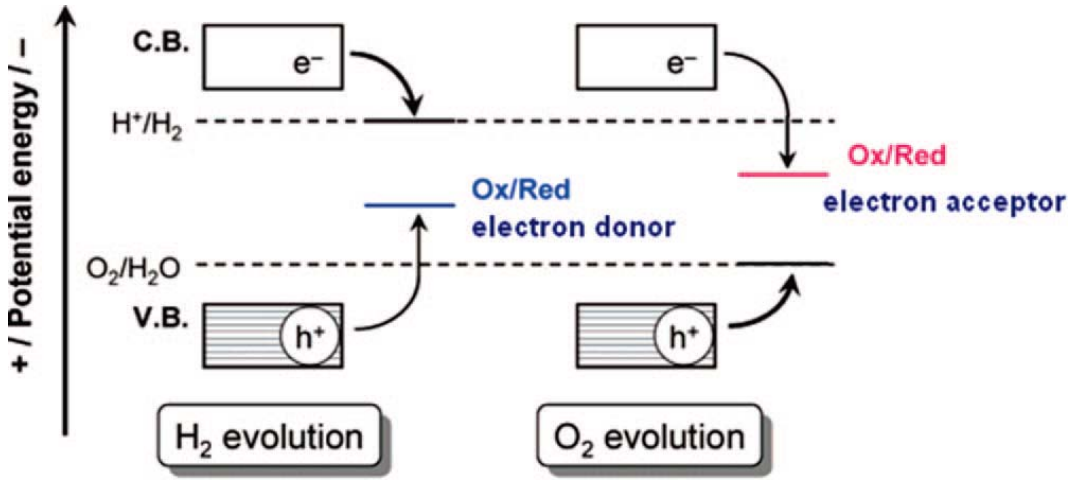

Figure 1.7 Basic principle of photocatalytic reaction in the presence of sacrificial reagents. Reproduced from Ref. 33.

In spite of that it is more attractive to split water into H_2 and O_2 simultaneously in one system, the low efficiency is really hard to satisfy the practical application. As shown in Figure 1.7, when the photocatalytic H_2 evolution is carried out in an aqueous solution containing sacrificial reagents (electron donors or hole scavengers), the photogenerated

holes will be irreversibly trapped by the hole scavengers instead of water; thus, the electrons will be enriched in the photocatalysts, and the H_2 evolution process will be promoted. The most advantage of this approach is that the photogenerated electrons and holes can be irreversibly separated, and the maximum electrons can participate in the photocatalytic reaction to reduce H_2O into H_2, thus resulting in a higher quantum efficiency.[33]

S^{2-}/SO_3^{2-} are the most widely-used electron donors, which can enhance both the photocatalytic activity and stability for H_2 evolution from water. A quantum yield of ~ 93% at 420 nm has been reported over Pt-PdS/CdS for the H_2 evolution in the presence of S^{2-}/SO_3^{2-} under visible light irradiation.[52] However, those materials contained S are easily photo-corroded under light irradiation and exhibit poor photocatalytic stability. Besides S based sacrificial reagents, other inorganic ions, such as Br^-,[48] CN^-,[53] and I^-[54] were also used as sacrificial reagents for H_2 evolution.

Organic compounds, such as alcohols (methanol over TiO_2,[55] ethanol over Pt-Ru/$Y_2Ta_2O_5N_2$,[56] isopropanol over Ni/NiO/$KNbO_3$/CdS[57]), acids (formic acid over Cu_2O,[58] acetic acid over Pt-TiO_2[59]), and aldehydes (formaldehyde over $LaNiO_3$[60]) can all be used as electron donors. Among them, methanol (CH_3OH) is the most widely used, which will finally be oxidized into CO_2 by photogenerated holes; while the remaining photogenerated electrons reduce H_2O into H_2. Inspired by the oxidation of toxic CH_3OH into CO_2, scientists designed a bi-functional photocatalytic system, in which both the degradation of organic pollutants into CO_2 and the H_2 evolution can be simultaneously processed. Those organic compounds can act as sacrificial electron donors and be oxidized into CO_2 by the photogenerated holes; while the photogenerated electrons reduce H_2O into H_2.[61] In Patsoura et al.'s study, the production of H_2 from

aqueous Pt/TiO_2 suspensions has been achieved in the presence of azo-dyes (e.g. Acid Orange 7, Basic Red 46, and Basic Blue 41) in the solution.[62] In this case, not only the clean hydrogen energy can be obtained, but also the target organic pollutants can be degraded, which makes a great progress in the renewable energy and environmental-protection. Besides dyes, other toxic organic compounds, such as 2,4-dichlorophenoxyacetic acid and 4-chlorophenol can also act as electron donors and be degraded over WO_x/TiO_2 under visible light irradiation, exhibiting promising route to solve the industry pollution.[63] Herein, in my PhD study, I mainly focus on the methanol as sacrificial reagent for the H_2 evolution.

1.3 CO_2 Photoreduction

Scientists now agree that the rise in atmospheric CO_2, the most abundant green house gas, comes from anthropogenic sources such as the burning of fossil fuels. This atmospheric rise in CO_2 results in global climate change.[64] Meanwhile, the energy shortage is also a big problem for all the human beings. Photoreduction of CO_2 into hydrocarbons might be an effective way to solve both the global warming and energy shortage. In particular, the reduction of CO_2 into $CO_2^{\bullet -}$ needs a relatively negative reduction potential of -1.9 V vs. NHE by one electron.[65,66] In addition, the rapid reduction requires an over-potential of 0.1-0.6 eV due to the kinetic restrictions imposed by the structure difference between liner CO_2 and bent $CO_2^{\bullet -}$.[67] Thus, it is unfavorable to reduce CO_2 via one-electron reaction, and the alternative and more favorable pathway for CO_2 photoreduction is through the proton-assisted multiple-electron transfer.[66]

$$CO_2 + 2H^+ + 2e^- \rightarrow HCOOH \qquad E^0 = -0.61\ V$$

$$CO_2 + 2H^+ + 2e^- \rightarrow CO + H_2O \qquad E^0 = -0.53\ V$$

$$CO_2 + 4H^+ + 4e^- \rightarrow C + 2H_2O \qquad E^0 = -0.20\ V$$

$$CO_2 + 4H^+ + 4e^- \rightarrow HCHO + H_2O \qquad E^0 = -0.48\ V$$

$$CO_2 + 6H^+ + 6e^- \rightarrow CH_3OH + H_2O \qquad E^0 = -0.38\ V$$

$$CO_2 + 8H^+ + 8e^- \rightarrow CH_4 + H_2O \qquad E^0 = -0.24\ V$$

To date, the light assisted CO_2 reduction is normally in three ways: organometallic complex compounds based photocatalysis, photoelectrochemical CO_2 reduction, and semiconductor based CO_2 photoreduction. In natural plant photosynthesis, water molecules are photo-oxidized to release oxygen and protons. The second stage is a light-independent reaction that converts carbon oxide into glucose. However, in the lab, the situation is a little different, which will be described in detail as below.

1.3.1 Organometallic Complex Compounds based CO_2 Photoreduction

Organometallic complex compounds have multiple and accessible redox states, and their reduction potentials can be systematically tuned via the ligand modification to better match the potential required for CO_2 reduction. Therefore, they are the most investigated and more commercially-available materials for CO_2 reduction to date. On the basis of the function of the catalyst acted in the photocatalytic reaction, the organometallic complex compounds based photocatalysis is classified as two types: in Type I photocatalysis, a molecular light absorber and a transition metal catalyst work combined together; in Type Ⅱ photocatalysis, the light absorber and the catalyst are the same molecular.

In Type I photocatalysis (Figure 1.8): the molecular light absorber P (e.g. ruthenium (Ⅱ) trisbipyridine, $[Ru(bpy)_3]^{2+}$) is firstly promoted to an excited state P* upon the light excitation. Then, this excited state is reductively quenched by a sacrificial amine donor

D (e.g. triethylamine) to yield a reduced sensitizer P^- and an oxidized amine donor $D^{\bullet+}$. The oxidized amines ($D^{\bullet+}$) are reactive, which will undergo the H atom abstraction and radical rearrangements, resulting in the production of a highly reduced carbon-centered radical species (D•). D• can further reduce a second photosensitizer under certain conditions.[68] After that, the reduced sensitizer P^- transfer the electron to the organometallic complex compounds catalyst to create the reductive active sites to reduce CO_2.[69-71] The first record is related to the $[Ru(bpy)_3]^{2+}$ sensitized transition-metal (Co or Ni) tetraazamacrocylic compounds toward CO_2 reduction into carbon monoxide and formate by Tinnemans et al. in 1984.[69]

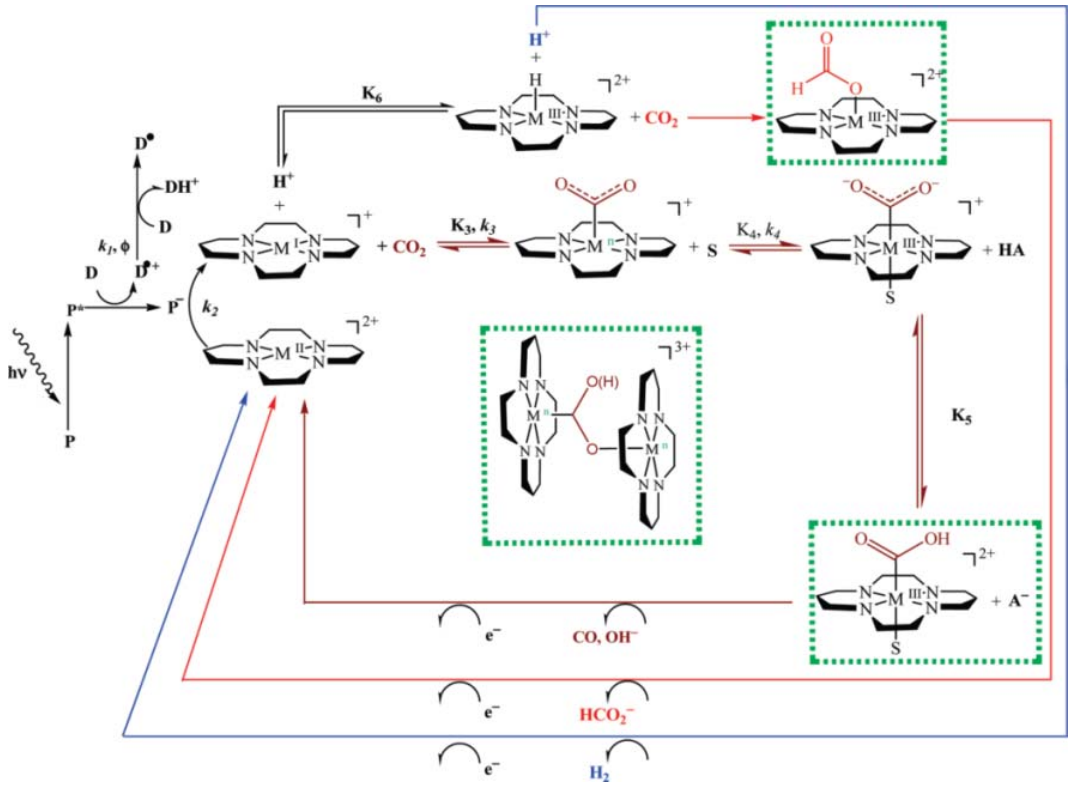

Figure 1.8 Schematic illustration of the proposed reaction mechanism of CO_2 reduction (Type I) over metal tetraazamacrocycles. Reproduced from Ref. 64.

Type Ⅱ catalysis occurs when the single compound act as both the light absorber

and the catalyst. As shown in Figure 1.9, the photocatalyst P_{cat} (e.g. $Re(bpy)(CO)_3X$) is firstly excited as the excitation state P_{cat}^* upon light excitation, then reductively quenched by the sacrificial amine donor D to yield a reduced P_{cat}^-, which is an active state of the catalyst and finally reduce CO_2 directly.

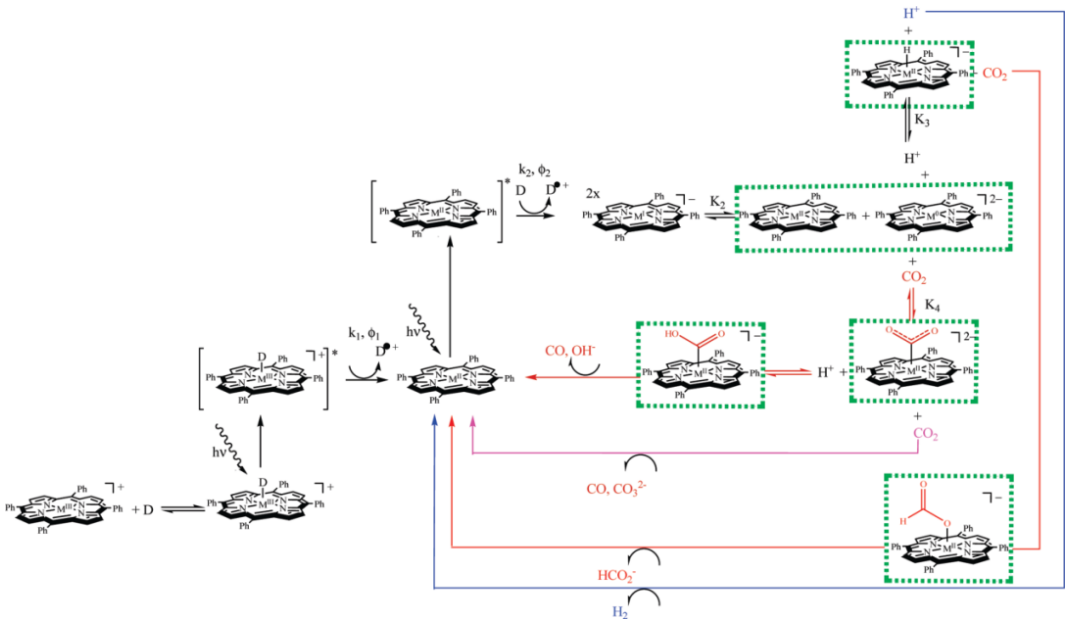

Figure 1.9 Schematic illustration of the proposed reaction mechanism of CO_2 reduction (Type Ⅱ) over metal porphyrin derivatives (M = Fe or Co). Reproduced from Ref. 64.

The organometallic complex compounds based photocatalysis can achieve a high turnover number. However, every organometallic complex compound only accepts one electron from the light absorber, so the CO_2 photoreduction is mainly one-electron transfer reaction with the product of CO. To achieve the hydrocarbon fuels, which are generally produced via the multiple-electron transfer reaction, more investigation should be carried out.

1.3.2 Photoelectrochemical CO_2 Reduction

In 1978, Halmann reported that CO_2 can be photocatalytically reduced into HCOOH, HCHO, and CH_3OH under the irradiation of mercury lamp via an electrochemical cell, which is composed of a p-type GaP single crystal cathode, carbon anode, and a buffered aqueous electrolyte.[72] After that, lots of study have been focused on the photoelectrochemical reduction of CO_2. In 1983, Canfield and Frese reported CO_2 can be reduced into methanol by using p-type GaAs and p-type InP photoelectrodes in a CO_2 saturated Na_2SO_4 solution under visible light irradiation.[73] In 1988, Eggins et al. carried out the CO_2 photoreduction in an aqueous solution of tetramethylammonium chloride via CdS electrode; glyoxylic acid, formic acid, acetic acids, as well as formaldehyde can be produced.[74] Later, in 1998, Fujiwara et al. investigated the ZnS nanocrystallites as photocatalyst for CO_2 reduction via triethylamine as electron donnor, it was found that the formation of sulfur vacancies which are resulted from the excess of metal ions can act as catalytic sites for the CO_2 reduction.[75]

Photoelectrochemical CO_2 reduction is a potential method to convert CO_2 into hydrocarbon fuels, because of its easy-fabrication and highly efficiency. However, the parameters (e.g. CO_2 concentration, pH values, and starting voltage) which can affect the photocatalytic activity are hard to reproduce, largely limiting the practical application.

1.3.3 Semiconductor based CO_2 Reduction

The benchmark event for CO_2 photoreduction over semiconductor powders happened in 1979, Inoue and Fujishima carried the CO_2 photoreduction tests on various semiconductor photocatalyst such as WO_3, TiO_2, ZnO, CdS, GaP, and SiC (Figure 1.10).[21] In detail, 1.0~2.0 g of powders (200-400 mesh) were suspended in the 100 mL

of purified water in a glass cell. Then, highly purified CO_2 gas was bubbled at 3 L/min through a water-suspended catalyst shaken by a magnetic stirrer. After that, the suspensions were illuminated through a quartz window of the glass cell by a 500 W Xe lamp or high pressure mercury arc lamp. It revealed that formic acid, formaldehyde, and methyl alcohol can be obtained from TiO_2, ZnO, CdS, GaP, and SiC suspensions; among which, SiC with the most negative conduction band potential produced the most products such as formaldehyde and methanol after illumination in 7 hours, and no methanol can be detected for WO_3 photocatalyst because of its more positive conduction band position than that of the redox potential of H_2CO_3/CH_3OH.[21]

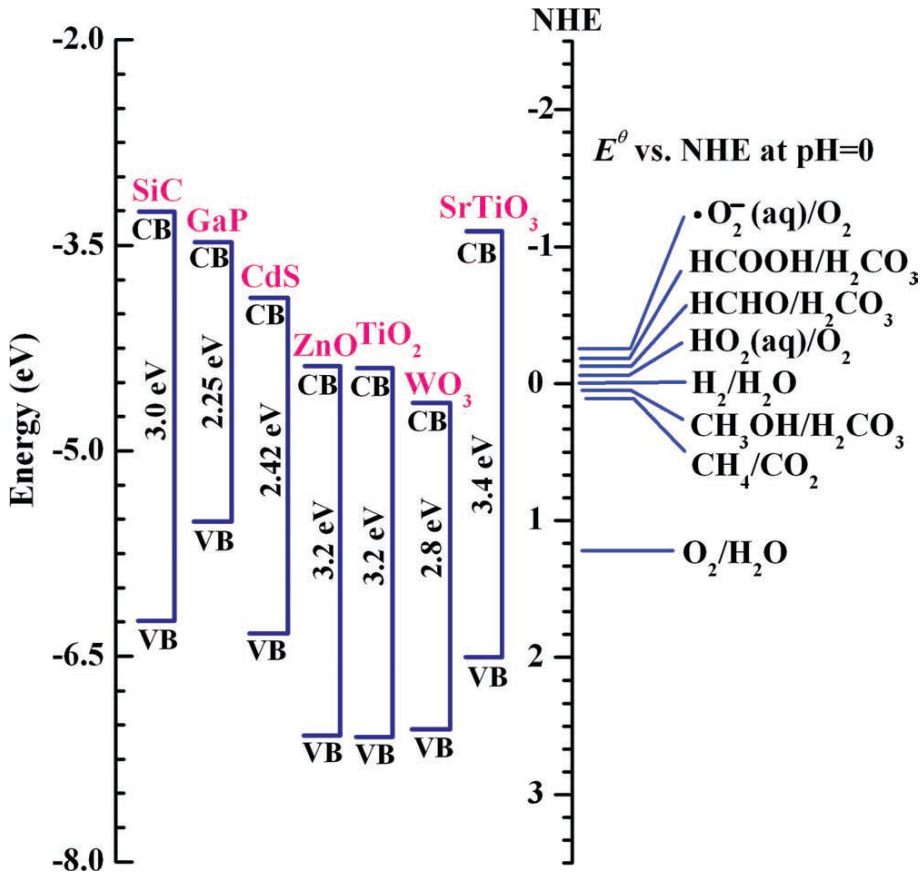

Figure 1.10 Schematic illustration of the energy correlation between semiconductor catalysts and redox couples in water. Reproduced from Ref. 9.

Recently, special attention has been paid on the meso-porous structured semiconductor photocatalysts, such as Zn_2GeO_4[3] and $ZnGa_2O_4$[76]. Because the porous structure is beneficial for the CO_2 adsorption, and the CO_2 must firstly adsorb on the surface of the photocatalysts in the CO_2 photoreduction process; thus the materials with porous structure exhibited much better photocatalytic performance. After N-doping, the photocatalyst can even photoreduce CO_2 into methane under visible light irradiation.[77]

1.4 TiO_2 Photocatalysis

Among lots of investigated photocatalysts, TiO_2 is almost the only material suitable for industrial use at present, because it has so many advantages, such as high photoreactivity, long-time stability, low lost, and environmental friendly properties. Nowadays, TiO_2 photocatalysis has been commercially-used in the application of detoxification of effluents, disinfection, super-hydrophilic self-cleaning, and the elimination of inorganic/organic gaseous pollutants in Japan.[78] More importantly, TiO_2 used as a white pigment from ancient times, therefore, its safety to humans and the environmental is guaranteed by history.[79]

The evolution of the scientific studies related to the photoactivity of TiO_2 is arisen from the early part of the 20th century. In 1938, Doodeve et al. reported that the UV absorption produces active oxygen species on the TiO_2 surface to bleach the dyes in both *vacuo* and oxygen.[80] Additionally, in that literature, TiO_2 is called as "photosensitizer". It is not very clear when and who firstly used the terminology of "photocatalyst", according to Hashimoto et al.'s review, in Japan, there were a series of reports described as "Autooxidation by TiO_2 as a photocatalyst" by Mashio et al. from 1956.[81] They dispersed TiO_2 powders into various organic solvents such as alcohols and

hydrocarbons followed by the UV irradiation with an Hg lamp. The autooxidation of solvents and the simultaneous formation of H_2O_2 under ambient conditions can be observed.[81] The possibility of solar photoelectrolysis is firstly reported in 1969 by using a single crystal n-type rutile TiO_2 as the electrode connected with a platinum black counter electrode under the near-UV light irradiation.[82]

In 1972, Fujishima and Honda discovered the photocatalytic splitting of water on TiO_2 electrodes.[18] This event is recognized as the landmark event which stimulated the study of solar energy conversion via photocatalysis. Since then, intense research has been carried out on TiO_2 photocatalysis, which has been focused on understanding the fundamental principles,[83,84] enhancing the photocatalytic efficiency,[85] and expanding the scope of applications.[78]

1.4.1 Properties of TiO_2

Titanium dioxide (TiO_2) has three main polymorphs, namely anatase, rutile, and brookite. Both of anatase and rutile are in distorted octahedron (TiO_6) classes, in which each Ti^{4+} ion is surrounded by an octahedron of six O^{2-} ions. However, the distortion of each octahedron are obviously different in the two different crystal structure: the octahedron shows a slight orthorhombic distrotion in rutile; while in anatase, the octahedron is significantly distorted, leading to a less orthorhombic symmetry as shown in Figure 1.11.[84] The Ti-Ti distances in antase are larger (3.79 and 3.04 Å for anatase vs. 3.57 and 2.96 Å for rutile), while the Ti-O distances are shorter (1.93 and 1.98 Å for anatase vs. 1.95 and 1.98 Å for rutile).[86] In the rutile structure, each octahedron is in contact with ten neighbor octahedrons (two sharing edge oxygen pairs and 8 sharing corner oxygen atoms); whereas, in the anatase structure, each octahedron is connected

with eight neighbors (four sharing an edge and four sharing a corner). These differences in lattice structure result in different mass densities and electronic band structures between anatase and rutile TiO_2.[83]

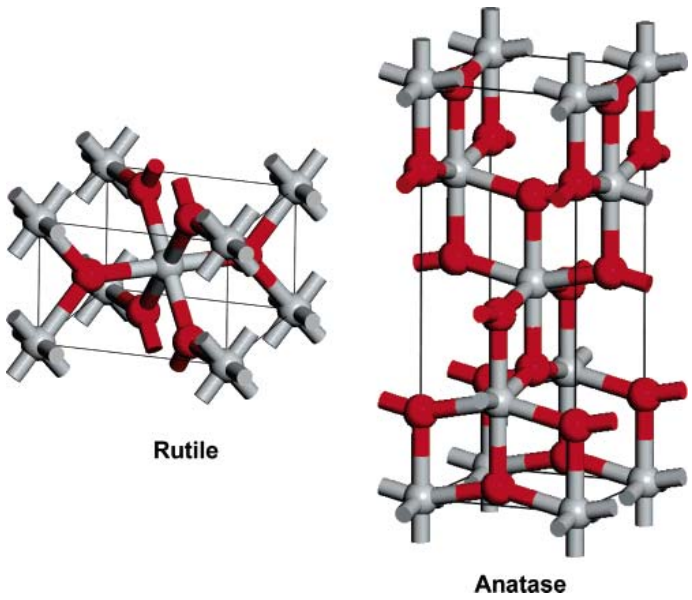

Figure 1.11 Crystal structures of the rutile and anatase TiO_2 (gray ball means Ti atom and red ball means O atom). Reproduced from Ref. 84.

1.4.2 Fundamentals of TiO_2 Photocatalysis

The utility of TiO_2 as a photocatalyst lies in its strong ability to convert solar energy into chemical energy. The bandgap of anatase TiO_2 is about 3.2 eV, it can only absorb and be excited by the light with wavelength smaller than 387 nm. Under the UV light irradiation, the electrons (e^-) will be firstly excited and move to the conduction band, leaving equal number of positive holes (h^+) on the valence band. Then, the photogenerated charge carriers (e^- and h^+) move to the TiO_2 surface; however, in this process, large amounts of charge carriers can not migrate to the surface and will recombine together in the formation of emitting light or phonons. Finally, the electrons

and holes on the surface to react with the adsorbed reactant to finish the whole photocatalytic reaction.[79]

1.4.3 Modification of TiO_2 toward Efficient Photocatalytic Activity

Generally, the photocatalytic activity of TiO_2 is affected by many factors, such as light absorption, crystallinity, surface area, surface reactivity,[87] and defect contents,[84] et al. In order to enhance the photocatalytic efficiency, the previous work are mainly focused on three aspects: improving the light utilization efficiency or light absorption of TiO_2 photocatalyst, enhancing the charge separation efficiency of the charge carriers, and promoting the surface reactivity or offering more surface reactive sites on the TiO_2 surface.[85]

1). Enhancing the light utilization efficiency of TiO_2 photocatalyst.

Because of its large band gap, TiO_2 can only be activated with the light with wavelength smaller than 387 nm (5% of the solar spectrum). To make better utility of the visible light, which occupies 43% of the solar spectrum, much work has been carried out to develop visible-light-driven TiO_2 photocatalyst.[85] Sensitization of TiO_2 with organic dyes or narrow band-gap inorganic semiconductors could realize the effective electron transfer from dyes or narrow band-gap semiconductors to TiO_2, thus enable the composite materials to absorb the visible light.[15,88] An overall solar to current conversion efficiency of 10.6% has been achieved for the dye-sensitized solar cells (DSSCs) reported by Gratzel et al. as shown in Figure 1.12.[88]

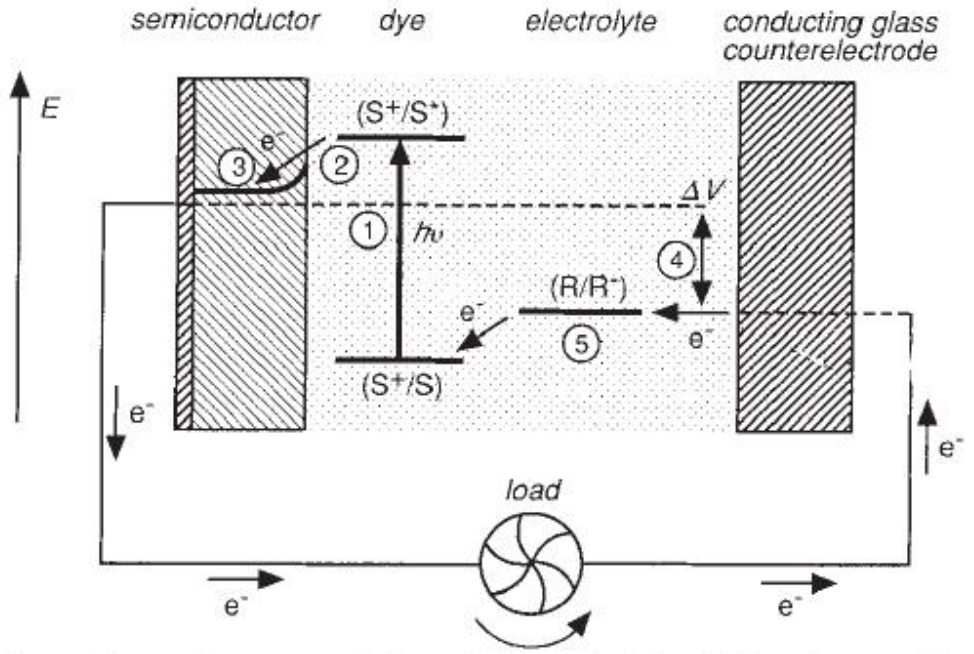

Figure 1.12 Schematic illustration of the principle of the dye-sensitized photovoltaic cell. The cell voltage observed under illumination is corresponding to the difference, △ *V*, between the quasi-Fermi level of TiO_2 under illumination and the electrochemical potential of the electrolyte. (S: sensitizer; S*: electronically excited sensitizer; S^+: oxidized sensitizer.) Reproduced from Ref. 88.

On the other hand, doping TiO_2 is an effective method to extend the light absorption of TiO_2 into visible light region.[78,89-91] Generally, the optical response of a semiconductor primarily depends on its internal electronic structure, which is closely related to its chemical composition, atomic arrangement, and crystal sizes. Doping of TiO_2 can not only maintain the integrity of the crystal structure but also produce favorable changes in the electronic structure to make TiO_2 visible-light-driven.[85] The photocatalytic activity of metal-doped TiO_2 is largely affected by the dopant concentration, the energy level of dopants in the TiO_2 lattice, their *d* electronic configuration, the distribution of the dopants, the electron donor concentration, the light

absorption intensity, and so on.[85] However, the existence of metal dopants in the TiO_2 matrix plays important roles on both the charge recombination and interfacial transfer of the charge carriers (e^- and h^+).[92] There were contradictory reports reporting either the increase or decrease of the photocatalytic efficiency.[93]

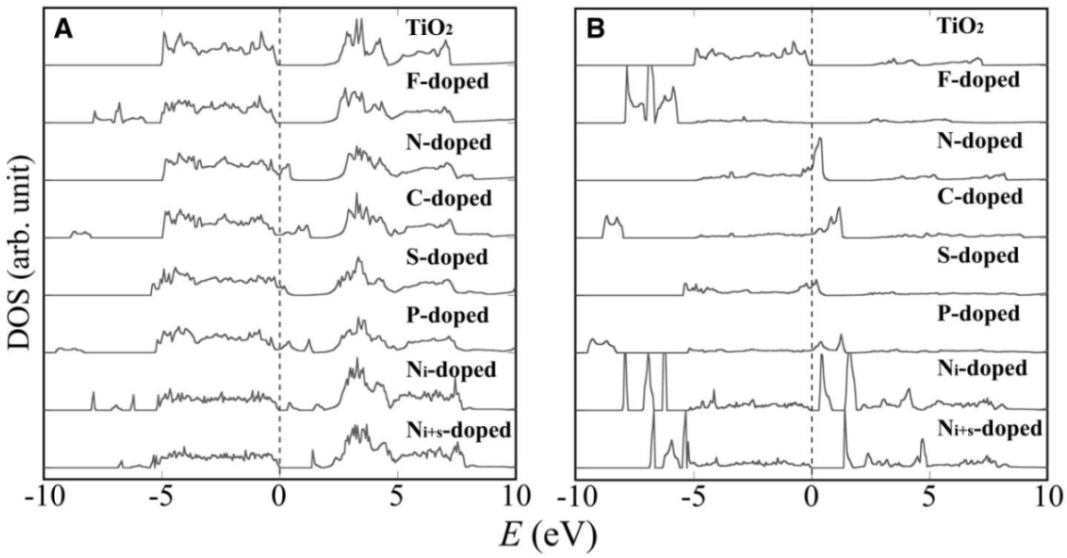

Figure 1.13 (a) Total DOSs of doped TiO_2 and (b) the projected DOSs into the doped anion sites, calculated by FLAPW. The dopants F, N, C, S, and P were located at a substitutional site for an O atom in the anatase TiO_2 crystal (the eight TiO_2 units per cell). The results for N doping at an interstitial site (N_i-doped) and that at both substitutional and interstitial sites (N_{i+s}-doped) are also shown. The energy is measured from the top of the valence bands of TiO_2, and the DOSs for doped TiO_2 are shifted so that the peaks of the O 2s states (at the farthest site from the dopant) are aligned with each other. (Arb. unit: arbitrary units.) Reproduced from Ref. 12.

In 2001, Asahi et al. firstly showed an absorption increase in the visible light region upon nitrogen-doped TiO_2 which can decompose methylene blue in the visible light

irradiation (λ > 420 nm).[12] As shown in Figure 1.13, they calculated the densities of states (DOSs) of the substitutional doping of C, N, F, P, or S for O in anatase TiO_2. It was found that the substitutional doping of N was the most effective, because the *p* states of the N contribute to the band-gap narrowing by mixing with O 2p states. In addition, the calculated imaginary parts of the dielectric functions of $TiO_{2-x}N_x$ indeed show a shift of the absorption edge to a lower energy by the N doping (Figure 1.14a). Later, the yellowish $TiO_{2-x}N_x$ films were obtained via sputtering the TiO_2 target in N_2 (40%) /Ar gas mixture, and the optical absorption spectra (Figure 1.14b) show that the $TiO_{2-x}N_x$ films noticeably absorb the light at less than 500 nm, whereas the TiO_2 films do not.[12] Besides N doping, other non-metal doping, such as Cl,[89] S,[94] F,[95] and C[96] were also studied in the past few years.

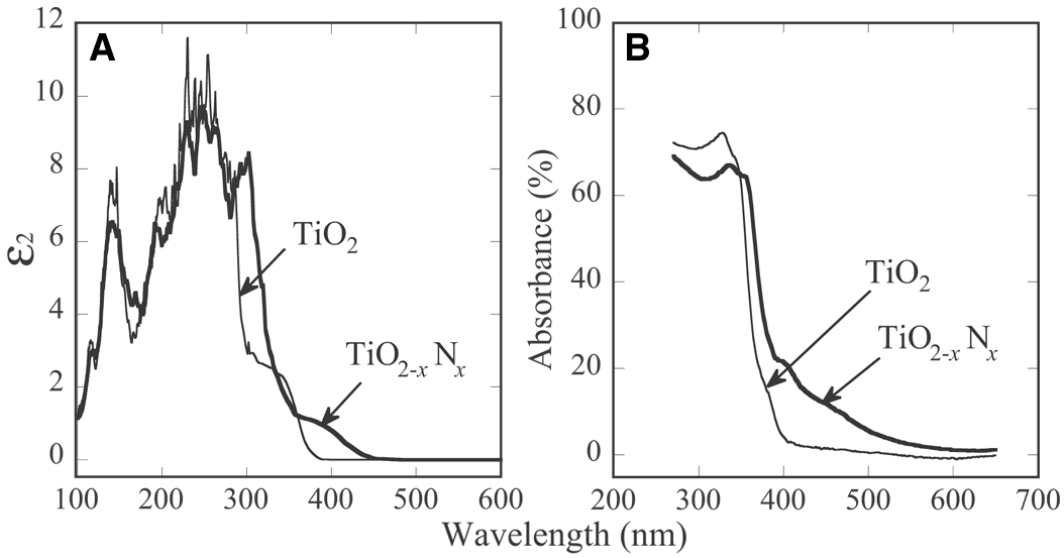

Figure 1.14 Optical properties of $TiO_{2-x}N_x$ (thick lines) compared with TiO_2 (thin lines). (a) Calculated imaginary parts of the dielectric functions (ε_2), which are averaged over three (x, y, and z) polarization vectors. (b) Experimental optical absorption spectra of $TiO_{2-x}N_x$ and TiO_2 films. Reproduced from Ref. 12.

Spatial structuring and size control of TiO_2 can also enhance the light utilization of TiO_2 without changing the chemical composition of TiO_2 photocatalyst.[13] For instance, as shown in Figure 1.15, photonic crystals with an inverse opal structure can promote light absorption by increasing the effective light path. The photonic crystal is consisting of the space creating a periodic dielectric constant field in the length around 300-800 nm.[97-99] This spatial structuring produces coherent Bragg diffraction patterns which forbid light to propagate trough the material. At the Bragg diffraction frequencies, photons propagate with strongly reduced velocity so they are called slow photons. If the energy of the slow photons overlaps with the absorption of the material, the light absorption will followed increased because of the increase of the effective optical path length.[8,13]

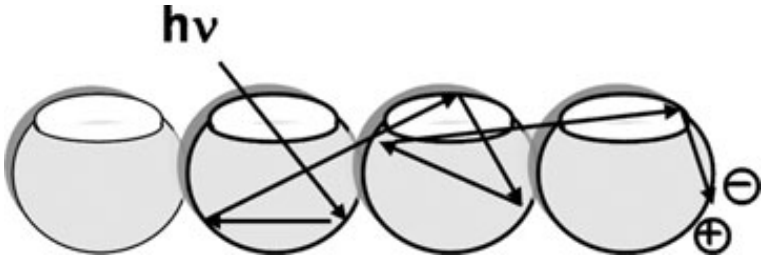

Figure 1.15 Application of the photonic crystal concept in an inverse opal configuration to increase the effective light path through the photocatalyst. Reproduced from Ref. 13.

Ozin et al. adopted this physical approach to slow down the photons and increase the light absorption for a higher photocatalytic activity. As shown in Figure 1.16, they prepared the inverse opal constituted by anatase TiO_2 ordered around monodisperse empty spheres of dimensions ranging from 280 to 500 nm. The dimension of the spheres creates a light stop band at the wavelength corresponding to the dimensions of the spheres (Figure 1.17). When the stop band is comparable to the light absorption

edge of TiO_2, the light absorption will be enhanced, leading to a higher photocatalytic activity.[100]

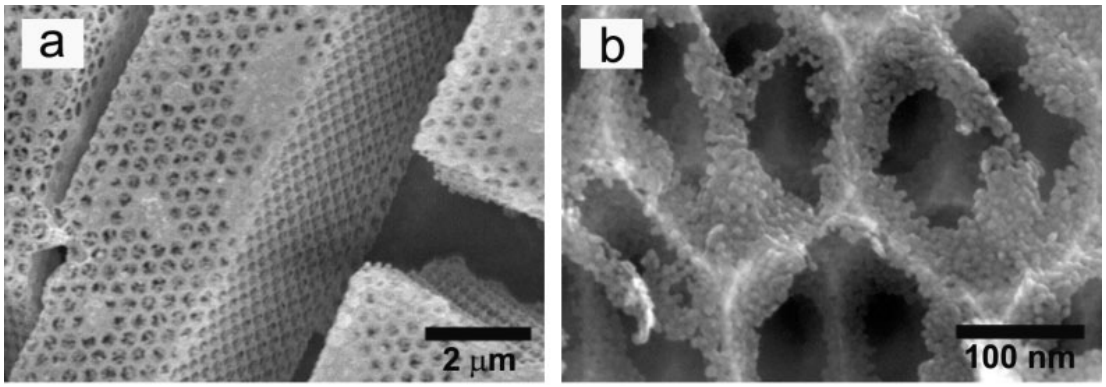

Figure 1.16 SEM images of TiO_2 inverse opals at lower (a) and higher (b) magnifications. Reproduced from Ref. 100.

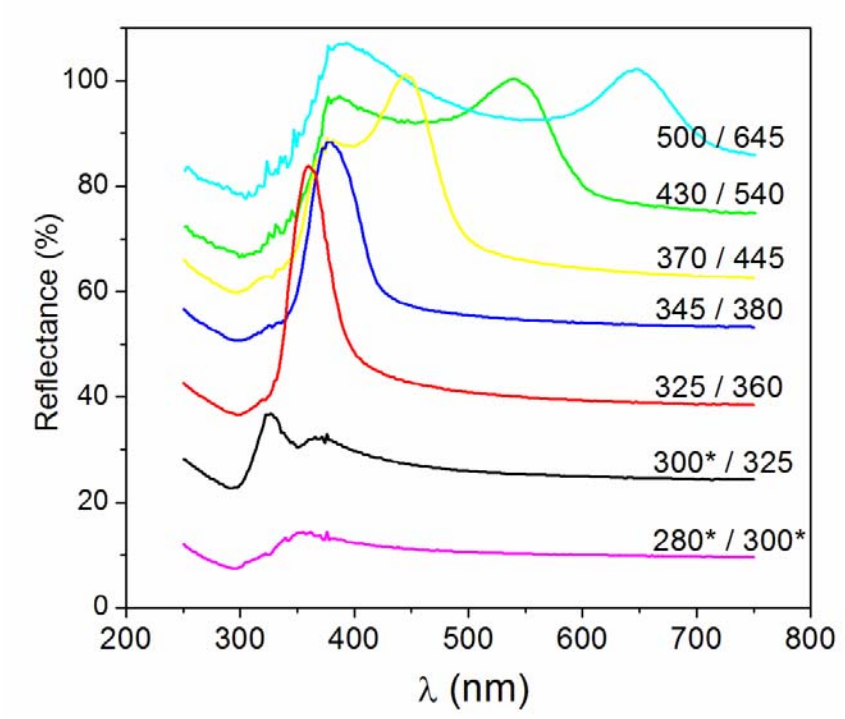

Figure 1.17 Reflectance spectra of TiO_2 in water. The stop-band positions in air (first number) and in water (second number) are indicated for each sample. Reproduced from Ref. 100.

2). Improving the charge separation efficiency.

Once excited, the electrons and holes need to move to the surface to take part in the photocatalytic reaction, however, large amounts of charge carriers can not migrate to the surface in time and recombine together in the bulk. Generally, TiO_2 with better crystallinity will exhibit higher photocatalytic activity, because the good crystallinity is beneficial for the inhibition of the charge recombination.[85] Meanwhile, reducing the particle size of the photocatalyst in several nanometers can enhance the charge separation, in that case the migration distance of the electrons and holes from bulk to the surface reactive sites can largely be shorten.[13,85]

Meanwhile, fabrication of photocatalyst with heterojunction structure can also enhance the charge separation efficiency and result in a promoted photocatalytic performance. In the previous study, numerous heterojunctions such as TiO_2/Ag_3PO_4,[16] TiO_2/Cu_2O,[17] and TiO_2/ZnO[101] junctions have been reported to enhance the photocatalytic properties. The main roles of the heterojunction are the matched band structure and the well-designed interface, which facilitate the charge transportation from one to another semiconductor. Figure 1.18 shows the schematic charge separation in the Ag_3PO_4/TiO_2 system. The conduction band of TiO_2 is more negative than that of Ag_3PO_4, while the valence band of Ag_3PO_4 is more positive than that of TiO_2. Under visible light irradiation, photon generated holes in the valence band of Ag_3PO_4 quickly transfer to the valence band of TiO_2, whereas photon generated electrons migrate from the conduction band of TiO_2 to that of Ag_3PO_4. The separation of electrons (in Ag_3PO_4) and holes (trapped in TiO_2) prevents the charge recombination, leading to higher photocatalytic activity.

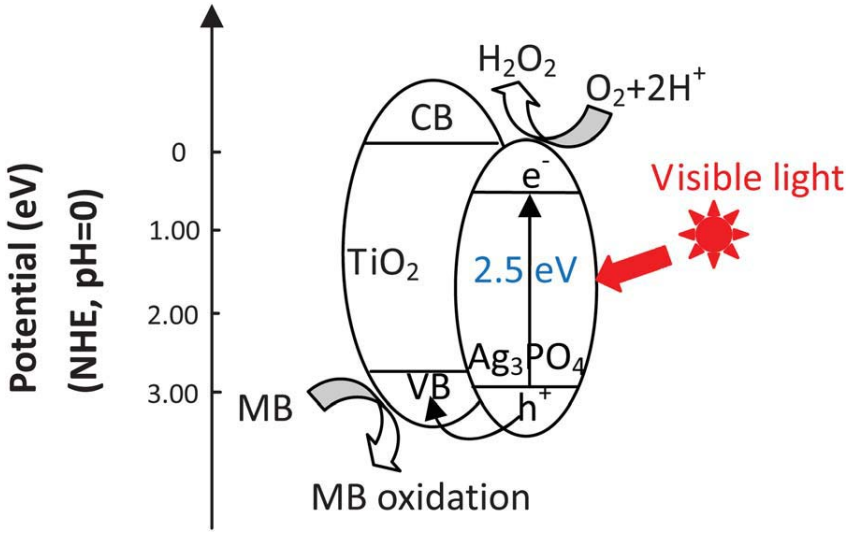

Figure 1.18 Schematic of the charge separation in TiO_2/Ag_3PO_4 composite under visible-light irradiation. Reproduced from Ref. 16.

3). Increasing surface reactive sites or promoting the surface reactivity.

Since many physical and chemical processes (e.g. adsorption of reactant molecules, surface transfer of photoexcited electrons to reactant molecules, and desorption of product molecules) happened on the surface during the photocatalytic reaction, thus more attention should be paid on the surface chemistry of TiO_2.[87,102] Due to their outstanding structural characteristics such as good adsorption ability and large surface area, which not only facilitate the reactant adsorption but also can offer more reaction sites in the photocatalytic reaction, porous-structure materials have been largely adopted in the field of photocatalysis.[90,103-105] On the other hand, for a crystalline TiO_2, the surface geometric (atomic arrangement and coordination) and electronic structures vary with crystal facets in different orientations, leading to various physical and chemical properties.[87,102,106] Therefore, tailored synthesis of TiO_2 single crystals with optimized high-reactive facets is another effective method to enhance the photocatalytic activity.

For anatase TiO_2, the surface energies of {001}, {100}, and {101} facets are

calculated to be 0.90, 0.53, and 0.44 J/m^2, respectively.[87] As shown in Figure 1.19, based on the Wulff construction and calculated surface energy, the shape of anatase under equilibrium conditions is a slightly truncated tetragonal bipyramid enclosed with the eight isosceles trapezoidal surfaces of {101} facet and two top squares of {001} facet. The percentage of {101} facet is predicted to be as high as 94%.

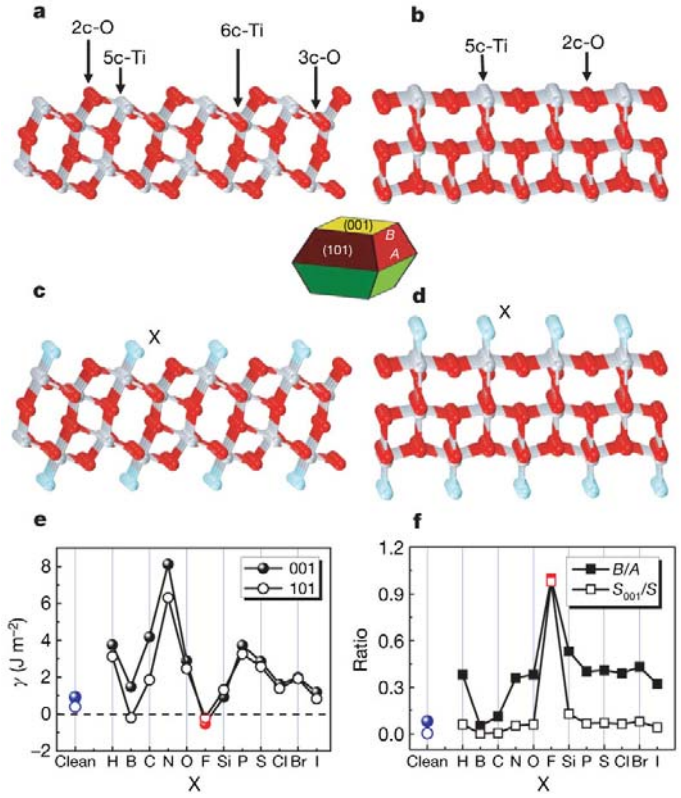

Figure 1.19 The optimized ratios of *B*/*A* and percentage of {001} facets (S_{001}/S), where *S* and S_{001} are respectively the total surface area and that contributed by the {001} facets, are also shown. (a, b): Unrelaxed, clean (001) and (101) surfaces. (c, d): Unrelaxed (001) and (101) surfaces surrounded by adsorbate X atoms. (e) Calculated energies of the (001) and (101) surfaces surrounded by X atoms. (f) Plots of the optimized value of *B*/*A* and percentage of {001} facets for anatase single crystals with various adsorbate atoms X. In (e and f), clean-surface results (denoted by blue spheres and circles) are used for reference. Reproduced from Ref. 102.

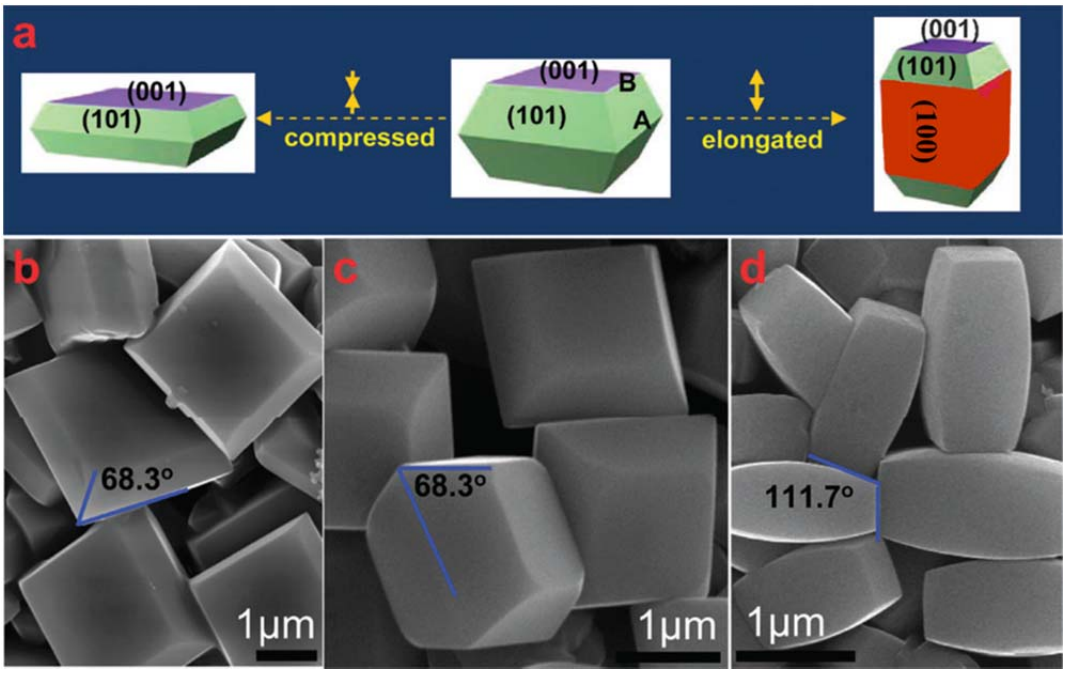

Figure 1.20 (a) Schematic of anatase TiO_2 with different percentages of {101}, {001} and {100} facets; (b)–(d): scanning electron microscopy (SEM) images of anatase crystals synthesized with different hydrofluoric acid (HF) aqueous solutions (120, 80 and 40 mM) containing different amounts of $TiOSO_4$ precursor (64, 32 and 32 mg) at 180 ^oC for different times (12, 12 and 2 h). Reproduced from Ref. 106.

In spite of that the surface energy of {100} facet was calculated to be between {001} and {101} facets, it is surprising that no {100} facet will appear in the equilibrium shape of anatase. However, Barnard et al. theoretically pointed out that the {100} facets would appear at the center of the anatase particles as the "belt".[87] In 2008, Yang et al. started the theoretical investigation about the influence of surface terminated non-metal atoms on the surface energies of anatase {101} and {001} facets, found that the surface terminated F can effectively reverse the stabilities of {101} and {001} facets. The maximum percentage of {001} facet was predicted to be more than 90% (Figure 1.19). Their subsequent experimental results further solidly confirmed the key role of the

surface fluorine in stabilizing {001} facet.[102] Besides {001} facet, {100} facet was also experimentally obtained via F as the capping reagents as shown in Figure 1.20.

It is generally accepted that the facet with a higher percentage of under-coordinated atoms are more active in the heterogeneous reactions, because these under-coordinated atoms may act as active reaction sites.[102] As shown in Figure 1.21a, in contrast to {101} facets with only 50% five-coordinate Ti (Ti_{5c}) atoms, both {001} and {100} facets owns 100% Ti_{5c} atoms on their surface. So, in terms of surface undercoordinated atoms (Ti_{5c}), both {001} and {100} facets would exhibit higher photoreactivity than {101} facet.

Nevertheless, the substantial role of the electronic structure can also affect the photocatalytic reactivity. Due to the differences in the surface atomic arrangements, TiO_2 exposed with various facets will exhibit different band gaps. This will correspondingly change the redox power of the photoexcited electrons and holes.[106] As shown in Figure 1.21 b-d, deduced from the UV-visible absorption spectra and valence band XPS spectra, T100 and T101 exhibit higher conduction band minimum than that of T001, indicating that more strongly reductive electrons can be generated on T101 and T100.

Apparently, {100} facet owns both favorable surface atomic structure and surface electronic structure, so that the more strongly reducing electrons in the conduction band can be transferred via the surface Ti_{5c} atoms as active reaction sites for T100. On the basis of the above analysis, we can conclude that both the electronic band structure and the surface atomic coordination will certainly affect the photocatalytic activity. Furthermore, the effect of the surface defects should be also considered in the photocatalytic reaction.[87]

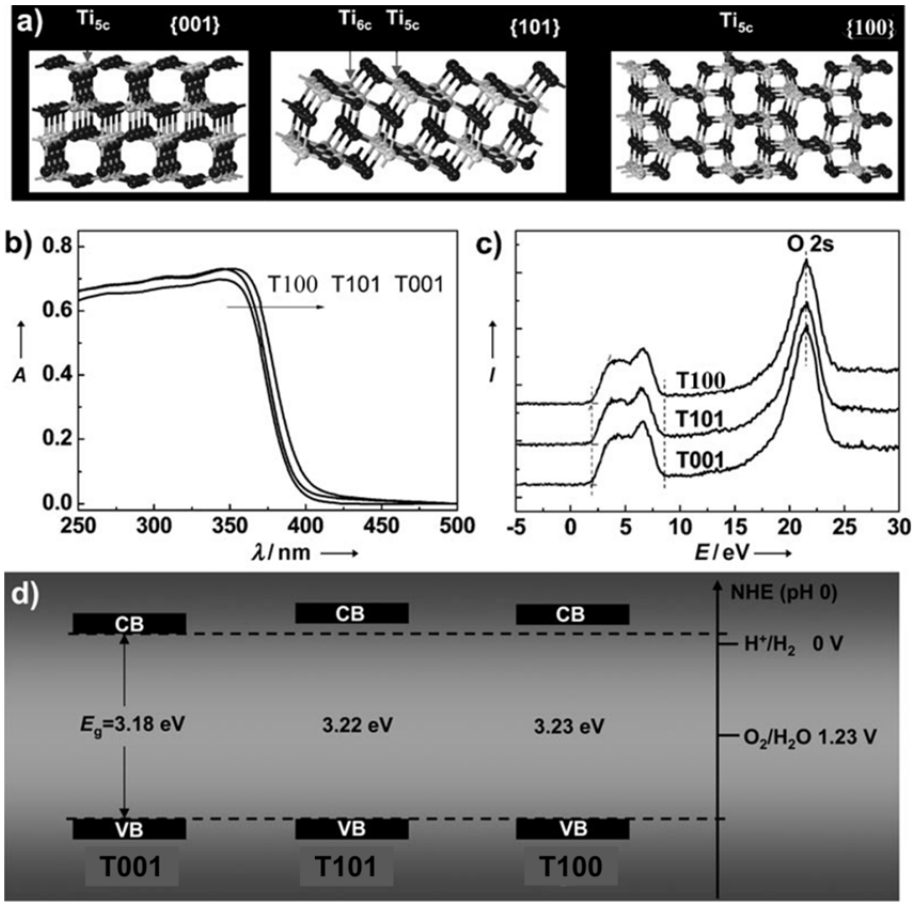

Figure 1.21 Surface atomic structure and electronic structure. (a) Schematic of atomic structure of {101}, {001}, and {100} faces. (b) UV/Vis absorption spectra of T001, T101, and T100. (c) Valence-band XP spectra of T001, T101, and T100. (d) Determined valence-band and conduction-band edges of T001, T101, and T100. (TiO_2 with dominant {001}, {101}, and {100} facets are denoted as T001, T101, and T100, respectively.) Reproduced from Ref. 106.

1.5 Research Motivations and Thesis Organization

On the basis of the above mentioned overview about the photocatalysis, photocatalytic water splitting, CO_2 photoreduction, and the related strategies for developing the superior photocatalytic properties of TiO_2, we can conclude that TiO_2 based photocatalysts are the good candidates in the fields of renewable energy. To find a

material with superior photocatalytic properties for the practical use is our goal, and TiO_2 might be such a promising material, thus my PhD work is to design and develop the advanced TiO_2 based materials towards efficient photocatalytic activity in both H_2 evolution and CO_2 photoreduction.

The photocatalysis is comprised of three steps: light excitation, charge migration, and the redox reactions on the surface. Therefore, regarding to each step of the photocatalysis, a series of studies were carried out over the TiO_2 based materials via enhancing the light utilization efficiency, charge separation, and surface reactivity, respectively to promote the photocatalytic activities.

Firstly, to enhance the light utilization efficiency, a physical phenomenon "Mie's scattering effect" was adopted over the TiO_2 spheres in the H_2 evolution for the first time. When the light collides with the TiO_2 spheres with size comparable to its wavelength, the Mie's scattering happens. The light scatters strongly along the forward direction; therefore, the path length of the incident light between the neighbored spheres will be increased, leading to the promoted light utilization efficiency. More light absorbed, more electrons and holes will be photo-generated.

After excitation, the electrons and holes need to migrate to the TiO_2 surface. However, large proportion of the charge carriers (e^--h^+ pairs) recombine together in the bulk of TiO_2. To enhance the charge separation efficiency, porous structured Cu_2O/TiO_2 nanojunction material is fabricated. The nanojunction structure can facilitate the charge separation process between Cu_2O and TiO_2. And the porous structure is beneficial for the CO_2 adsorption. Those combined properties can endow the Cu_2O/TiO_2 nanojunction exhibit marked photocatalytic activity in the CO_2 photoreduction.

Furthermore, since the redox reactions are taken place on the TiO_2 surface, thus

promoting the surface reactivity is also an effective method to enhance the photocatalytic activity. For anatase TiO_2, the {100} facet is considered to be the active facet in the photocatalysis. Thus, fabrication of TiO_2 single crystals exposed with more active {100} facets can facilitate to offer more active reactive sites on the TiO_2 surface. However, to date, the highest percentage of the {100} facet exposed on TiO_2 sample is reported to be 85.7% with a relatively small surface area of 5.8 m^2/g. To make more {100} facet exposed, both the percentage of the exposed {100} facets and the surface area are largely increased in our designed anatase TiO_2 nanosheets for a better photocatalytic performance.

Finally, a breakthrough has been made in the surface chemistry of TiO_2; for the first time, {111} facet exposed anatase TiO_2 single crystals are experimentally realized. In comparison to the previously reported {001}, {100}, and {101} facets, {111} facet owns superior surface properties in both surface atomic structure and electronic structure. More importantly, those superior surface properties make our prepared {111} facet exposed TiO_2 exhibit excellent photocatalytic properties in the H_2 evolution.

The dissertation is divided into six chapters. A summary of the remaining five chapters is listed as below:

Chapter 2: Size-Dependent Mie's Scattering Effect on TiO_2 Spheres for the Superior Photoactivity of H_2 Evolution

In chapter 2, a novel strategy of coupling Mie's scattering effect into the light-absorption region of TiO_2 was developed to enhance the light utilization efficiency. The light scattering efficiency is largely dependent on the size of the scattering spheres and the wavelength of the incident light. Hereby, TiO_2 spheres with different diameters (330–750 nm) were selectively fabricated to investigate the correlation between the

particle size and the scattering effect. Via optimization of the size of the TiO_2 spheres, the Mie's scattering effect could be efficient in the light absorption region of TiO_2, thus the light utilization efficiency will be enhanced, leading to higher photocatalytic performance in the H_2 evolution.

Chapter 3: Porous-Structured Cu_2O/TiO_2 Nanojunction Material toward Efficient CO_2 Photoreduction

In Chapter 3, porous-structured Cu_2O/TiO_2 nanojunction materials for efficient CO_2 photoreduction were successfully fabricated. The well-designed nanojunction structure can effectively inhibit the charge recombination process. In addition, the porous structure of the nanojunction is beneficial for the CO_2 adsorption. Most importantly, this material exhibited excellent photocatalytic performance in the CH_4 evolution, which is attributed to its well-designed nanojunction structure combined with the porous structure, which can simultaneously enhance the charge separation efficiency and facilitate the CO_2 adsorption.

Chapter 4: High-Active Anatase TiO_2 Nanosheets Exposed with 95% {100} Facets toward Efficient H_2 Evolution and CO_2 Photoreduction

In chapter 4, anatase TiO_2 nanosheets with 95% high-active {100} facets exposed and a relatively large surface area of 57.1 m^2/g were successfully prepared. {100} facet is considered to be the active facet in H_2 evolution, on which the under-coordinated Ti atoms (Ti_{5c}) can act as active sites in the photocatalytic reaction. Herein, via increasing both the percentage of the exposed {100} facet and the surface area, more {100} facet will be exposed on the TiO_2 photocatalyst, thus the reactivity of the sample is largely enhanced.

Chapter 5: Anatase TiO_2 Single Crystals Exposed with High-Reactive {111} Facets

towards Efficient H_2 Evolution

In chapter 5, for the first time, {111} facet exposed anatase TiO_2 single crystals were prepared. In comparison with the intensively investigated {001}, {100}, and {101} facets for anatase TiO_2, {111} facet owns a much higher surface energy of 1.61 J/m^2, in addition with the superior surface atomic structure and electronic structure. Experimentally, the large amounts of under-coordinated atoms on the TiO_2 surface can act as active sites for the photoreaction, and the superior electronic band structure can facilitate to produce more reductive electrons to reduce H^+ into H_2; all those superior properties happened on our developed {111} facets exposed TiO_2 make it exhibit excellent photocatalytic performance in the H_2 evolution.

Chapter 6: General Conclusion and Future Prospects

In chapter 6, an overall summary of the achievements of the dissertation work is given. And the recommendations for the further work are also suggested.

Reference:

(1) Hoffmann, M. R.; Martin, S. T.; Choi, W. Y.; Bahnemann, D. W. *Chem. Rev.* **1995**, *95*, 69.

(2) Ouyang, S. X.; Tong, H.; Umezawa, N.; Cao, J. Y.; Li, P.; Bi, Y. P.; Zhang, Y. J.; Ye, J. H. *J. Am. Chem. Soc.* **2012**, *134*, 1974.

(3) Yan, S. C.; Ouyang, S. X.; Gao, J.; Yang, M.; Feng, J. Y.; Fan, X. X.; Wan, L. J.; Li, Z. S.; Ye, J. H.; Zhou, Y.; Zou, Z. G. *Angew. Chem. Int. Ed.* **2010**, *49*, 6400.

(4) Ouyang, S. X.; Ye, J. H. *J. Am. Chem. Soc.* **2011**, *133*, 7757.

(5) Wang, R.; Hashimoto, K.; Fujishima, A.; Chikuni, M.; Kojima, E.; Kitamura, A.; Shimohigoshi, M.; Watanabe, T. *Nature* **1997**, *388*, 431.

(6) Tang, J. W.; Quan, H. D.; Ye, J. H. *Chem. Mater.* **2007**, *19*, 116.

(7) Yu, J. C.; Ho, W. K.; Lin, J.; Yip, K. Y.; Wong, P. K. *Environ. Sci. Technology* **2003**, *37*, 2296.

(8) Chen, X. Q.; Ye, J. H.; Ouyang, S. X.; Kako, T.; Li, Z. S.; Zou, Z. G. *ACS Nano* **2011**, *5*, 4310.

(9) Tong, H.; Ouyang, S. X.; Bi, Y. P.; Umezawa, N.; Oshikiri, M.; Ye, J. H. *Adv. Mater.* **2012**, *24*, 229.

(10) Fox, M. A.; Dulay, M. T. *Chem. Rev.* **1993**, *93*, 341.

(11) Hagfeldt, A.; Gratzel, M. *Chem. Rev.* **1995**, *95*, 49.

(12) Asahi, R.; Morikawa, T.; Ohwaki, T.; Aoki, K.; Taga, Y. *Science* **2001**, *293*, 269.

(13) Aprile, C.; Corma, A.; Garcia, H. *Phys. Chem. Chem. Phys.* **2008**, *10*, 769.

(14) Li, H.X.; Bian, Z.F.; Zhu, J.; Zhang, D.Q.; Li, G.S.; Huo, Y.N. Li, H.; Lu, Y.F. *J. Am. Chem. C* **2007**, *129*, 8406.

(15) Jia, H. M.; Xu, H.; Hu, Y.; Tang, Y. W.; Zhang, L. Z. *Electrochem. Commun.* **2007**, *9*, 354.

(16) Yao, W. F.; Zhang, B.; Huang, C. P.; Ma, C.; Song, X. L.; Xu, Q. J. *J. Mater. Chem.* **2012**, *22*, 4050.

(17) Chu, S.; Zheng, X. M.; Kong, F.; Wu, G. H.; Luo, L. L.; Guo, Y.; Liu, H. L.; Wang, Y.; Yu, H. X.; Zou, Z. G. *Mater. Chem. Phys.* **2011**, *129*, 1184.

(18) Fujishima, A.; Honda, K. *Nature* **1972**, *238*, 37.

(19) Zou, Z. G.; Ye, J. H.; Sayama, K.; Arakawa, H. *Nature* **2001**, *414*, 625.

(20) Yi, Z. G.; Ye, J. H.; Kikugawa, N.; Kako, T.; Ouyang, S. X.; Stuart-Williams, H.; Yang, H.; Cao, J. Y.; Luo, W. J.; Li, Z. S.; Liu, Y.; Withers, R. L. *Nature Mater.* **2010**,

9, 559.

(21) Inoue, T.; Fujishima, A.; Konishi, S.; Honda, K. *Nature* **1979**, *277*, 637.

(22) Tu, W. G.; Zhou, Y.; Liu, Q.; Tian, Z. P.; Gao, J.; Chen, X. Y.; Zhang, H. T.; Liu, J. G.; Zou, Z. G. *Adv. Funct. Mater.* **2012**, *22*, 1215.

(23) Zuttel, A.; Borgschulte, A.; Schlapbach, L. *Wiley-VCH:Weinheim, Germany* **2008**.

(24) Muradov, N. Z.; Veziroglu, T. N. *Int. J. Hydrogen Energy* **2008**, *33*, 6804.

(25) Badwal, S. P. S.; Giddey, S.; Munnings, C. *WIRES; Energy and Environment.* **2012**, *doi:10.1002/wene.50*.

(26) HFCIT Hydrogen Production: Natural Gas Reforming, U.S. Department of Energy. 2008-12-15.

(27) Damen, K.; van Troost, M.; Faaij, A.; Turkenburg, W. *Prog. Energy Combust. Sci.* **2006**, *32*, 215.

(28) Cormos, C. C.; Starr, F.; Tzimas, E.; Peteves, S. *Int. J. Hydrogen Energy* **2008**, *33*, 1286.

(29) Cobden, P. D.; van Beurden, P.; Reijers, H. T. J.; Elzinga, G. D.; Kluiters, S. C. A.; Dijkstra, J. W.; Jansen, D.; van den Brink, R. W. *Int. J. Greenhouse Gas Control* **2007**, *1*, 170.

(30) Bard, A. J. *J. Photochem.* **1979**, *10*, 59.

(31) Bard, A. J. *Science* **1980**, *207*, 139.

(32) Bard, A. J. *J. Phys. Chem.* **1982**, *86*, 172.

(33) Chen, X. B.; Shen, S. H.; Guo, L. J.; Mao, S. S. *Chem. Rev.* **2010**, *110*, 6503.

(34) Xu, Y.; Schoonen, M. A. A. *Am. Mineral.* **2000**, *85*, 543.

(35) Sato, S.; White, J. M. *Chem. Phys. Lett.* **1980**, *72*, 83.

(36) Domen, K.; Naito, S.; Soma, M.; Onishi, T.; Tamaru, K. *J. Chem. Soc. Chem. Commun.* **1980**, 543.

(37) Yamaguti, K.; Sato, S. *J. Chem. Soc. Farad Transaction I* **1985**, *81*, 1237.

(38) Domen, K.; Naito, S.; Onishi, T.; Tamaru, K. *Chem. Phys. Lett.* **1982**, *92*, 433.

(39) Kudo, A.; Sayama, K.; Tanaka, A.; Asakura, K.; Domen, K.; Maruya, K.; Onishi, T. *J. Catal.* **1989**, *120*, 337.

(40) Machida, M.; Yabunaka, J.; Kijima, T. *Chem. Mater.* **2000**, *12*, 812.

(41) Kato, H.; Asakura, K.; Kudo, A. *J. Am. Chem. Soc.* **2003**, *125*, 3082.

(42) Kim, H. G.; Hwang, D. W.; Bae, S. W.; Jung, J. H.; Lee, J. S. *Catal. Lett.* **2003**, *91*, 193.

(43) Maeda, K.; Saito, N.; Lu, D. L.; Inoue, Y.; Domen, K. *J. Phys.Chem. C* **2007**, *111*, 4749.

(44) Maeda, K.; Domen, K. *J. Phys. Chem. C* **2007**, *111*, 7851.

(45) Maeda, K.; Teramura, K.; Domen, K. *J. Catal.* **2008**, *254*, 198.

(46) Kudo, A. *MRS Bull.* **2011**, *36*, 32.

(47) Qu, Y.Q.; Duan, X.F. *Chem. Soc. Rev.* **2013**, *42*, 2568.

(48) Fujihara, B.; Ohno, T.; Matsumura, M. *J. Chem. Soc. Faraday Trans.* **1998**, *94*, 3705.

(49) Abe, R.; Sayama, K.; Domen, K.; Arakawa, H. *Chem. Phys. Lett.* **2001**, *344*, 339.

(50) Sasaki, Y.; Nemoto, H.; Saito, K.; Kudo, A. *J. Phys.Chem. C* **2009**, *113*, 17536.

(51) Maeda, K.; Higashi, M.; Lu, D. L.; Abe, R.; Domen, K. *J. Am. Chem. Soc.* **2010**, *132*, 5858.

(52) Yan, H. J.; Yang, J. H.; Ma, G. J.; Wu, G. P.; Zong, X.; Lei, Z. B.; Shi, J. Y.; Li,

C. *J. Catal.* **2009**, *266*, 165.

(53) Lee, S. G.; Lee, S.; Lee, H. I. *Appl. Catal. a-General* **2001**, *207*, 173.

(54) Yang, Y. H.; Chen, Q. Y.; Yin, Z. L.; Li, J. *Appl. Surf. Sci.* **2009**, *255*, 8419.

(55) Yi, H. B.; Peng, T. Y.; Ke, D. N.; Ke, D.; Zan, L.; Yan, C. H. *Inter. J. Hydrogen Energy* **2008**, *33*, 672.

(56) Liu, M. Y.; You, W. S.; Lei, Z. B.; Zhou, G. H.; Yang, J. J.; Wu, G. P.; Ma, G. J.; Luan, G. Y.; Takata, T.; Hara, M.; Domen, K.; Can, L. *Chem. Commun.* **2004**, 2192.

(57) Ryu, S. Y.; Choi, J.; Balcerski, W.; Lee, T. K.; Hoffmann, M. R. *Ind. Eng. Chem. Res.* **2007**, *46*, 7476.

(58) Kakuta, S.; Abe, T. *ACS Appl. Mater. Interfaces* **2009**, *1*, 2707.

(59) Zheng, X. J.; Wei, L. F.; Zhang, Z. H.; Jiang, Q. J.; Wei, Y. J.; Xie, B.; Wei, M. B. *Int. J. Hydrog. Energy* **2009**, *34*, 9033.

(60) Jia, L. S.; Li, J. J.; Fang, W. P. *J. Alloy. Compd.* **2010**, *489*, L13.

(61) Patsoura, A.; Kondarides, D. I.; Verykios, X. E. *Catal. Today.* **2007**, *124*, 94.

(62) Patsoura, A.; Kondarides, D. I.; Verykios, X. E. *Appl. Catal. B-Environ.* **2006**, *64*, 171.

(63) Zhang, X. H.; Liu, H.; Li, W. Z.; Cui, G. F.; Xu, H. Y.; Han, K.; Long, Q. P. *Catal. Lett.* **2008**, *125*, 371.

(64) Morris, A. J.; Meyer, G. J.; Fujita, E. *Account. Chem. Res.* **2009**, *42*, 1983.

(65) Schwarz, H. A.; Dodson, R. W. *J. Phys. Chem.* **1989**, *93*, 409.

(66) Fujita, E. *Coord. Chem. Rev.* **1999**, *185-6*, 373.

(67) Fujita, E.; Brunschwig, B. S. *In Electron Transfer in Chemistry; Balzani, V.,Ed.;Wiley-VCH:Weinheim, Germany* **2001**, *4*, 88.

(68) Whitten, D. G. *Acc. Chem. Res.* **1980**, *13*, 83.

(69) Tinnemans, A. H. A.; Koster, T. P. M.; Thewissen, D.; Mackor, A. *Recl. Trav. Chim. Pays-Bas-J. Roy. Neth. Chem. Soc.* **1984**, *103*, 288.

(70) Matsuoka, S.; Yamamoto, K.; Ogata, T.; Kusaba, M.; Nakashima, N.; Fujita, E.; Yanagida, S. *J. Am. Chem. Soc.* **1993**, *115*, 601.

(71) Ogata, T.; Yamamoto, Y.; Wada, Y.; Murakoshi, K.; Kusaba, M.; Nakashima, N.; Ishida, A.; Takamuku, S.; Yanagida, S. *J. Phys. Chem.* **1995**, *99*, 11916.

(72) Halmann, M. *Nature* **1978**, *275*, 115.

(73) Canfield, D.; Frese, K. W. *J. Electrochem. Soc.* **1983**, *130*, 1772.

(74) Eggins, B. R.; Irvine, J. T. S.; Murphy, E. P.; Grimshaw, J. *J. Chem. Soc. Chem. Commun.* **1988**, 1123.

(75) Fujiwara, H.; Hosokawa, H.; Murakoshi, K.; Wada, Y.; Yanagida, S. *Langmuir* **1998**, *14*, 5154.

(76) Zhang, N.; Ouyang, S. X.; Li, P.; Zhang, Y. J.; Xi, G. C.; Kako, T.; Ye, J. H. *Chem. Commun.* **2011**, *47*, 2041.

(77) Zhang, N.; Ouyang, S. X.; Kako, T.; Ye, J. H. *Chem. Commun.* **2012**, *48*, 1269.

(78) Fujishima, A.; Zhang, X. T.; Tryk, D. A. *Surf. Sci. Reports* **2008**, *63*, 515.

(79) Hashimoto, K.; Irie, H.; Fujishima, A. *Japan. J. Appl. Phys.* **2005**, *44*, 8269.

(80) Doodeve, C. F.; Kitchener, J. A. *Trans. Faraday Soc.* **1938**, *34*, 902.

(81) Kato, S.; Mashio, F. *Abtr. Book Annu. Meet. Chem. Soc. Japan* **1956**, 223.

(82) Fujishima, A.; Honda, K.; Kikuchi, S. *Kogyo Kagaku Zasshi* **1969**, *72*, 108.

(83) Linsebigler, A. L.; Lu, G. Q.; Yates, J. T. *Chem. Rev.* **1995**, *95*, 735.

(84) Thompson, T. L.; Yates, J. T. *Chem. Rev.* **2006**, *106*, 4428.

(85) Chen, X.; Mao, S. S. *Chem. Rev.* **2007**, *107*, 2891.

(86) Burdett, J. K.; Hughbanks, T.; Miller, G. J.; Richardson, J. W.; Smith, J. V. *J.*

Am. Chem. Soc. **1987**, *109*, 3639.

(87) Liu, G.; Yu, J. C.; Lu, G. Q.; Cheng, H. M. *Chem. Commun.* **2011**, *47*, 6763.

(88) Gratzel, M. *Nature* **2001**, *414*, 338.

(89) Xu, H.; Zheng, Z.; Zhang, L. Z.; Zhang, H. L.; Deng, F. *J. Solid State Chem.* **2008**, *181*, 2516.

(90) Xu, H.; Zhang, L. Z. *J. Phys. Chem. C* **2010**, *114*, 940.

(91) Xu, H.; Zhang, L. Z. *J. Phys. Chem. C* **2010**, *114*, 11534.

(92) Herrmann, J. M.; Disdier, J.; Pichat, P. *Chem. Phys. Lett.* **1984**, *108*, 618.

(93) Martin, S. T.; Morrison, C. L.; Hoffmann, M. R. *J. Phys. Chem.* **1994**, *98*, 13695.

(94) Ho, W. K.; Yu, J. C.; Lee, S. C. *J. Solid State Chem.* **2006**, *179*, 1171.

(95) Yu, J. C.; Yu, J. G.; Ho, W. K.; Jiang, Z. T.; Zhang, L. Z. *Chem. Mater.* **2002**, *14*, 3808.

(96) Ren, W. J.; Ai, Z. H.; Jia, F. L.; Zhang, L. Z.; Fan, X. X.; Zou, Z. G. *Appl. Catal. B-Environ.* **2007**, *69*, 138.

(97) Ozin, G. A.; Yang, S. M. *Adv. Funct. Mater.* **2001**, *11*, 95.

(98) Tetreault, N.; Miguez, H.; Ozin, G. A. *Adv. Mater.* **2004**, *16*, 1471.

(99) Arsenault, A.; Fleischhaker, F.; von Freymann, G.; Kitaev, V.; Miguez, H.; Mihi, A.; Tetreault, N.; Vekris, E.; Manners, I.; Aitchison, S.; Perovic, D.; Ozin, G. A. *Adv. Mater.* **2006**, *18*, 2779.

(100) Chen, J. I. L.; von Freymann, G.; Choi, S. Y.; Kitaev, V.; Ozin, G. A. *Adv. Mater.* **2006**, *18*, 1915.

(101) Xi, G. C.; Ye, J. H. *Chem. Eur. J.* **2010**, *16*, 8719.

(102) Yang, H. G.; Sun, C. H.; Qiao, S. Z.; Zou, J.; Liu, G.; Smith, S. C.; Cheng, H.

M.; Lu, G. Q. *Nature* **2008**, *453*, 638.

(103) Antonelli, D. M.; Ying, J. Y. *Angew. Chem. Int. Ed.* **1995**, *34*, 2014.

(104) Wilson, G. J.; Will, G. D.; Frost, R. L.; Montgomery, S. A. *J. Mater. Chem.* **2002**, *12*, 1787.

(105) Zhang, L. Z.; Yu, J. C. *Chem. Commun.* **2003**, 2078.

(106) Pan, J.; Liu, G.; Lu, G. M.; Cheng, H. M. *Angew. Chem. Int. Ed.* **2011**, *50*, 2133.

Chapter 2 Size-Dependent Mie's Scattering Effect on TiO_2 Spheres for the Superior Photoactivity of H_2 Evolution

2.1. Introduction

Photocatalysis is an environmentally-friendly and promising technology to convert solar energy into chemical energy.[1-5] In 1972, Fujishima and Honda reported that TiO_2 electrode could photocatalytic split water into H_2 and O_2 under some bias potential and UV light irradiation.[6] After that, much work has been carried out on TiO_2 to enhance the photocatalytic activity.[7-11] In general, the TiO_2 photocatalytic cycle comprises three steps: first, light excitation induces the transition of electrons from valance band to the conduction band, leaving an equal number of vacant sites (holes); second, the excited electrons and holes migrate to the surface of TiO_2; third, they react with the adsorbed electron donors and electron acceptors, respectively.[1] Since the first step for the photocatalysis is the light excitation process, a high-efficient utilization of the incident light is an effective method to enhance the photocatalytic performance.[12-16]

Light can be scattered and redirected in many directions. Particularly, when the size of the particles is comparable to the wavelength of the incident light, the Mie's scattering happens. In the atmosphere, the clouds appear white is attributed to the Mie's scattering effect which can scatter all wavelength of the visible light by the various sized dusts. If we introduce the Mie's scattering phenomenon into the TiO_2 spheres, when the light collides with the TiO_2 sphere with size comparable to its wavelength, the light scatters strongly along the forward direction. This scattering produces a pattern like an antenna lobe, with a sharper and more intense forward lobe (Figure 2.1 a).[17] Therefore, the path length of the incident light between the neighbored spheres will be

increased,[18] leading to a promoted light utilization efficiency over the TiO_2 spheres. The scattering phenomenon has been applied in the dye-sensitized solar cells (DSSC) before,[19,20] however, to the best of our knowledge, there is few study available on the light scattering effect over TiO_2 in the application of H_2 evolution. Previous work reported that the light scattering efficiency is largely dependent on the size of the scattering particle and the wavelength of the incident light.[21] Therefore, fabrication of TiO_2 spheres with suitable diameter is critical to induce the Mie's scattering effect happened in the light absorption region of TiO_2.

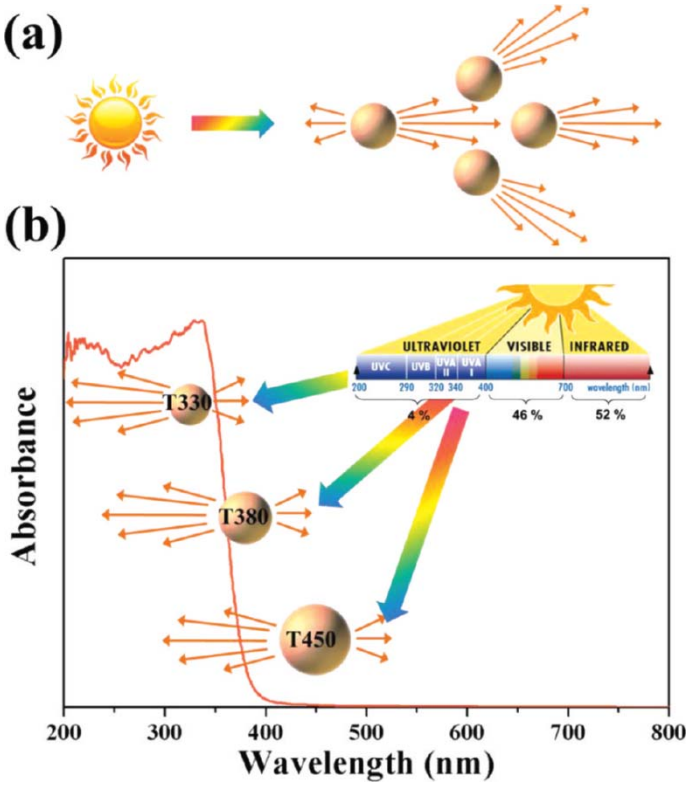

Figure 2.1 The schematic illustration of the Mie's scattering phenomenon among the TiO_2 spheres (a), and the simulated scattering region for the TiO_2 spheres with different diameters (b). (TiO_2 spheres with diameters of 330 nm, 380 nm, and 450 nm were denoted as T330, T380, and T450, respectively.)

In this chapter, we develop a strategy of coupling Mie's scattering into the light-absorption region of TiO_2 to enhance the light-utilization efficiency of the TiO_2 spheres. The band gap of TiO_2 is 3.2 eV, which can only be excited by the light with wavelength smaller than 387 nm. According to the Mie's scattering theory, the light will be strongly scattered on the surface of TiO_2 with an appropriate size comparable to its wavelength. When the scattering cross section exhibits a number of resonances for a given particle size of TiO_2 sphere, the scattering will be very efficient at these wavelengths. Therefore, the scattering efficiency in different wavelength region of the incident light spectrum is largely dependent on the diameter of TiO_2 spheres. Only when the scattering resonant peak, which indicates the strongly efficient scattering,[22] is coupled into the light-absorption region of TiO_2, the scattering and absorption for the TiO_2 is effective, followed with the highest light utilization efficiency. As shown in Figure 2.1 b, the scattering phenomenon occurred on the TiO_2 spheres with diameters of smaller (330 nm), comparable (380 nm), and larger (450 nm) than the light absorption edge of TiO_2 (about 387 nm) is depicted. We can assume that the scattering effect happened on the TiO_2 spheres will be various and related to the different diameters. Based on the above assumption, herein, the TiO_2 spheres with different sizes (330 nm, 380 nm, 450 nm, 600 nm, and 750 nm) have been selectively fabricated. The scattering resonant peaks over the TiO_2 spheres were checked to study the correlation between the particle size and the scattering efficiency. The further photocatalytic H_2 evolution and photoelectrochemical measurements over the TiO_2 spheres were investigated to test the validity of the coupling strategy of size-dependent Mie's scattering effect.

2.2 Experimental Methods

2.2.1 Synthesis of TiO_2 Spheres

The TiO_2 spheres were prepared via a facile sol-gel method[23] by the coagulation of titanium tetra-n-butyl (TBOT) with the polymer poly(methyl methacrylate) (PMMA) spheres as templates as shown in Figure 2.2. Typically, 0.05 g PMMA spheres and 0.6 mL ammonium were firstly added into a mixed solution of 75 mL ethanol and 25 mL acetonitrile. In this step, the PMMA spheres were negatively charged, while the ammonium was selected to electrostatically stabilize the PMMA template because of the positive charged NH_4^+. After stirred for 20 min, 3 mmol of TBOT was subsequently added and adsorbed on the surface of the NH_4^+/$PMMA^-$ spheres, followed with a series of hydrolysis process to form the amorphous TiO_2 via a magnetic stirring at room temperature for 24 h. Finally, the white precipitation was heated at 500 ^oC for 2 h with a temperature ramping rate of 1 ^oC /min, all the PMMA polymers were removed, leading to the formation of TiO_2 hollow spheres. By using different sized PMMA spheres as the template, TiO_2 spheres with different diameters were selectively prepared. The diameters of the TiO_2 spheres were controlled to be 330, 380, 450, 600, and 750 nm (denoted as T330, T380, T450, T600, and T750) by adopting 170, 260, 330, 450, and 670 nm sized PMMA spheres, respectively.

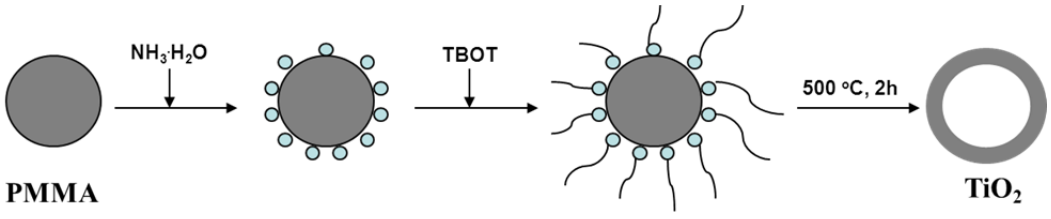

Figure 2.2 Schematic illustration of the reaction process of the TiO_2 spheres.

2.2.2 Preparation of TiO_2 Films

The TiO_2 films used for the photoelectrochemical test were prepared via a spin-coating method. The 20 mg of TiO_2 samples were firstly dispersed into 10 mL of ethanol solvent by ultrasonic treatment, then spin-coated on the ITO substrate layer by layer for 50 times. In the procedure of spin coating, every drop of the TiO_2 suspension was about 0.05 mL. In each cycle, 3 drops of suspension was dripped on the ITO substrate. The spin speed and time were 800 rpm for 5 s followed with 1000 rpm for 30 s. Finally, the coated films were heated to 500 ^oC at a rate of 1 ^oC/min and kept at this temperature for 2 h.

2.2.3 Characterization

The X-ray diffraction (XRD) patterns of the prepared samples were conducted on a Rigaku Multiflex diffractometer (RINT 2000; Rigaku Corp., Japan) with monochromatized Cu Ka radiation (λ=1.54178 Å). The size and morphology of the samples were observed by a scanning electron microscope (SEM, JSM-6701F, JEOL Co., Japan) and transmission electron microscope (TEM, JEM-200 CX, JEOL Co., Japan) operating at 200 kV. The Brunauer-Emmett-Teller (BET) surface areas were recorded by a surface area analyzer (Tristar 3000, Micromeritics Inc., USA) with nitrogen absorption at 77 K. The UV-visible diffuse reflectance spectra were measured on a UV-visible spectrophotometer (UV-2500PC, Shimadzu Co., Japan).

2.2.4 Photocatalytic H_2 Evolution Test

Photocatalytic reactions of H_2 evolution were carried out in a closed gas circulation system with an external-irradiation Pyrex-cell. The light source was a 300 W xenon lamp. The intensity of the light at 300-800 nm was measured to be 242.3 mW/cm^2 using a spectroradiometer (USR-40; Ushio Inc., Japan). The co-catalyst Pt was loaded by an

in situ photodeposition method. The 0.5 wt % Pt-loaded catalyst (0.09 g) was firstly ultrasonically dispersed into monodispersed spheres suspended in a methanol aqueous solution (50 mL of methanol and 220 mL of water). Then magnetic stirring was used to stabilize the suspension during the whole photocatalytic H_2 evolution process. The evolved gas including H_2 was analyzed by an online gas chromatograph (GC-8A; Shimadzu Corp., Japan) equipped with a thermal conductivity detector.

2.2.5 Photoelectrochemical Measurement

Photocurrent measurements were performed with an electrochemical station (ALS/CH model 650A, Japan) using a three-electrode mode with 0.1 M Na_2SO_4 solution as the electrolyte. The TiO_2 photoanodes were used as working electrodes; a Pt wire served as a counter electrode. The Ag/AgCl electrode was used as the reference electrodes. The illumination source was a 500 W Xe lamp (Optical ModuleX; Ushio Inc., Japan). The intensity of the light at 300-800 nm was measured to be 140.4 mW/cm^2 using a spectroradiometer (USR-40; Ushio Inc., Japan). In the photocurrent-time measurement, the TiO_2 photoelectrodes were illuminated at normal incidence of light trough a quartz window. The voltage-scan speed was 0.1 V/s, and light was chopped manually at regular intervals.

2.3 Results and Discussion

2.3.1 Crystal Structure and Morphology of the TiO_2 Spheres

The XRD patterns of the as-prepared TiO_2 samples are shown in Figure 2.3. The XRD profiles of all the samples can be coincidently indexed by the standard anatase TiO_2 pattern (JCPDS file No. 71-1167). The peaks at 25.25, 37.72, 48.03, 53.91, and 54.99 degree can be assigned to (101), (004), (200), (105), and (211) crystal planes of

anatase TiO_2, respectively. It is well-known that the crystallinity of the TiO_2 during the crystal growth process is largely dependent on the water content, the solution acidity, and the calcination temperature. Since the TiO_2 spheres were prepared in the same procedure and similar preparation environment (0.06 mL ammonium added and calcination at 500 ^oC for 2 h), thus leading to the similar crystallinity for all the TiO_2 samples.

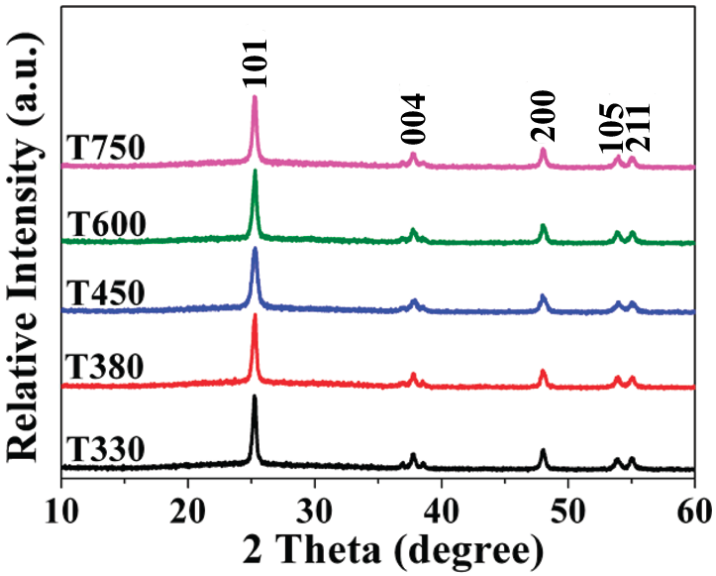

Figure 2.3 XRD patterns of the as-prepared TiO_2 spheres.

The size and morphology of the TiO_2 samples can be observed by the SEM images (Figure 2.4a-e). There is no obvious difference in the surface morphology except for the size among the TiO_2 spheres with different diameters around 330, 380, 450, 600, and 750 nm, respectively. Furthermore, the TEM image confirms the spherical structure with an average size of 380 nm for T380 (Figure 2.4f). Meanwhile, the contrast between the bold dark ring and the bright inner circle indicates that the sphere is hollow which is resulted from the removal of the PMMA template via calcination. The enlarged representative surface of the TiO_2 sphere (Figure 2.4g) reveals that the TiO_2 sphere

consists of a large amount of tiny nanoparticles (~ 3 nm). The spacing of the lattice fringes is 0.350 nm as shown in the HRTEM image (Figure 2.4h), which is associated with the (101) lattice plane of the anatase TiO_2.

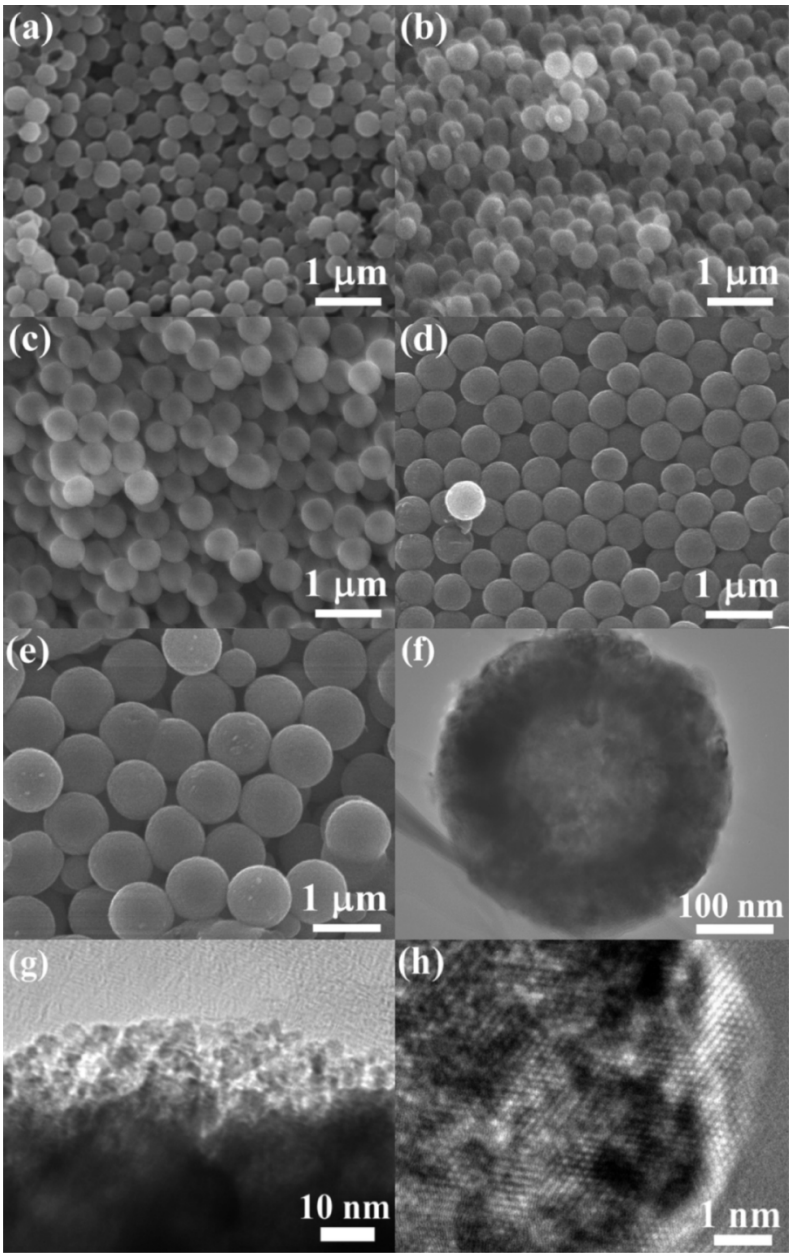

Figure 2.4 SEM images of the TiO_2 spheres, (a) T330, (b) T380, (c) T450, (d) T600, and (e) T750; the TEM image (f), the high-magnified TEM image (g), and HRTEM image (h) of T380.

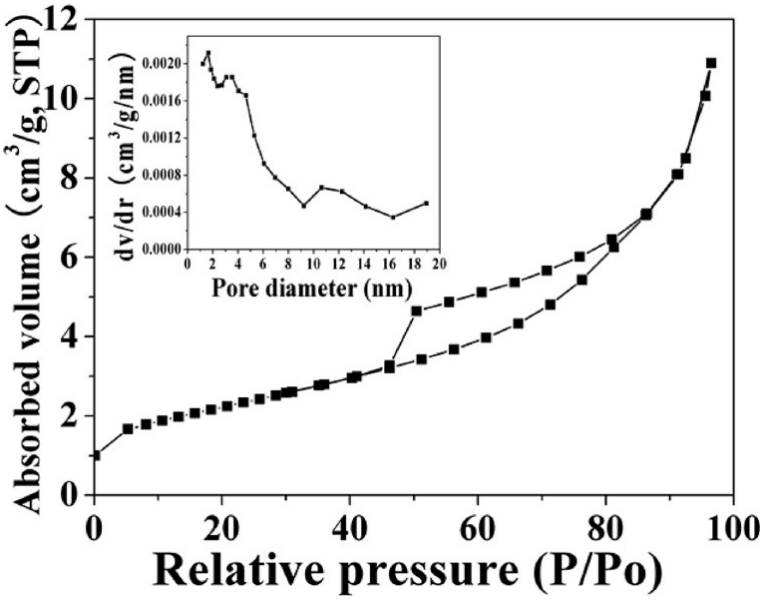

Figure 2.5 Nitrogen adsorption-desorption isotherms and pore-size distribution curve (inset) of the prepared TiO_2 sample (T380).

As shown in Figure 2.5, the N_2 adsorption-desorption isotherms of T380 exhibits a typical Type Ⅳ isotherm with hysteresis loop, which is associated with capillary condensation taking place in mesopores, and the limiting uptake over a range of high P/P_0.[24] Moreover, the pore-size distribution curve of T380 (inset of Figure 2.5) indicates that the TiO_2 samples contain mesopores with diameter smaller than 10 nm. This result is well consistent with the TEM image as shown in Figure 2.4g. The TiO_2 spheres are made of large amounts of small nanoparticles and the mesopores are resulted from the aggregates of the nanoparticles. Therefore, besides the contribution of the external and internal surface areas of the hollow sphere, the pores resulted from the aggregation of the small TiO_2 nanocrystalline consisted in the TiO_2 sphere also make an effort to the total surface area. Finally, the Brunauer-Emmett-Teller (BET) specific surface areas are recorded as 13.8, 9.4, 10.1, 10.2, and 8.8 m^2/g for T330, T380, T450, T600, and T750, respectively (as listed in Table 2.1).

2.3.2 Optical Properties of TiO_2 Spheres

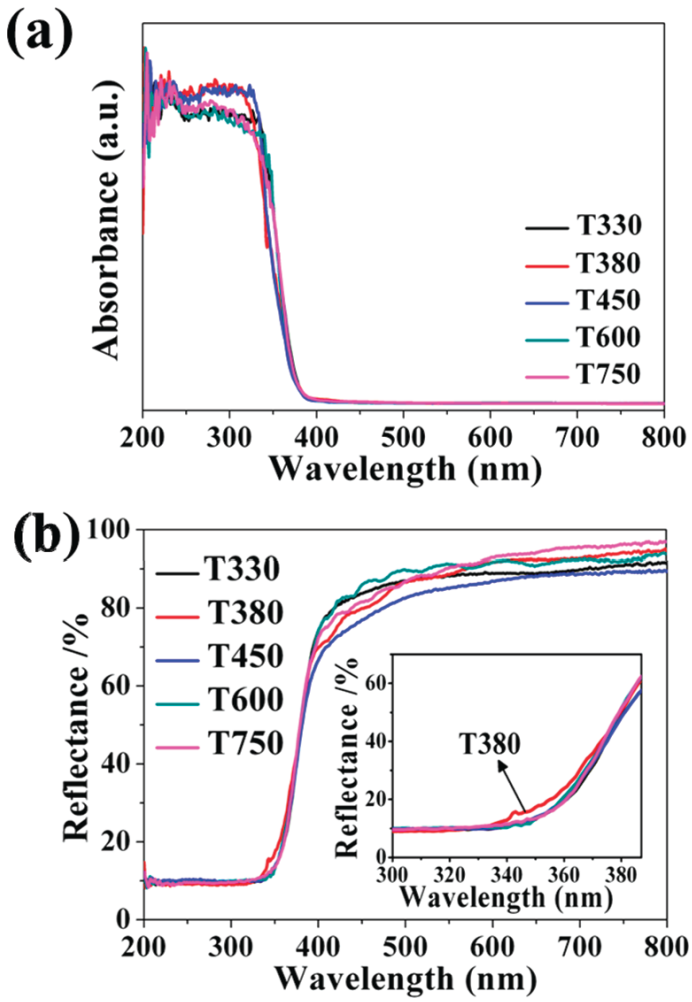

Figure 2.6 (a) The UV-visible absorption spectra of the TiO_2 powders; and (b) the UV-visible diffuse reflectance spectra of the TiO_2 powders and the enlarged part in the region of 300-387 nm (inset).

The optical properties of the TiO_2 sphere powders are shown in Figure 2.6. All the TiO_2 samples exhibit the similar light absorption edge around 380 nm (Figure 2.6a), while a little differences exist in the reflectance spectra, especially in the region of 335-370 nm (inset of Figure 2.6b), which reveals that T380 presents a relatively higher reflectance intensity compared with other TiO_2 samples. It is well-known that the

light-scattering performance of TiO_2 is strongly dependent on the particle size, and the size dependency of the scattering effect can be evaluated by the reflectance spectra to some extent.[25] Therefore, since T380 exhibits the strongest reflectance intensity in the region of 335-370 nm, it might have a strong scattering efficiency in this region.

2.3.3 Photocatalytic H_2 Evolution of the TiO_2 Spheres

The photocatalytic activities of the H_2 evolution were tested for all the TiO_2 sphere samples. The amounts of the evolved H_2 over the TiO_2 samples were 76, 265, 94, 136, and 131 μmol/h for T330, T380, T450, T600, and T750, respectively (as depicted in Table 2.1). Among which, T380 exhibited obviously higher photocatalytic activity compared with the other TiO_2 samples. Usually the photocatalytic performance of TiO_2 is affected by various factors such as the morphology, the phase composition, the crystallinity, the surface area, and so on. In this work, considering that the crystallinity is not appreciably different for these TiO_2 samples (Figure 2.3), so the effect of the crystallinity on the photocatalytic performance can be ignored. Moreover, taking the surface area into account, the photocatalytic activities of the TiO_2 samples are 61, 313, 103, 148, and 165 μmol/($h \cdot m^2$) for T330, T380, T450, T600, and T750, respectively (Figure 2.7), in which the photoactivity of T380 is also superior to that of other TiO_2 samples. Therefore, the highest photocatalytic activity of the H_2 evolution over T380 can be attributed that the unique diameter can result in a strongly efficient scattering effect in the light absorption region of TiO_2 and thus lead to the enhanced photocatalytic performance.

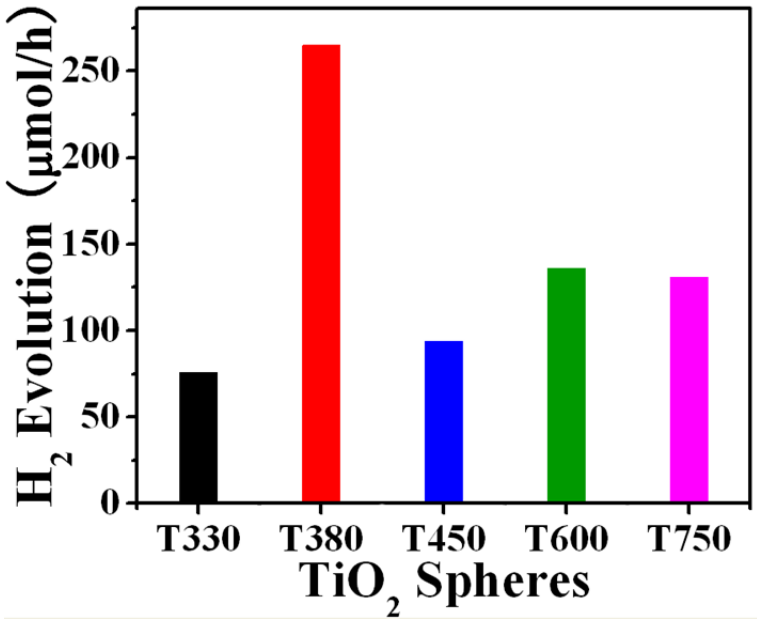

Figure 2.7 The photocatalytic activities of H_2 evolution over the different sized TiO_2 spheres (with 0.5 wt% Pt loaded) under UV-visible light irradiation (λ > 300 nm).

2.3.4 Mechanism of Mie's Scattering Effect on the TiO_2 Spheres

The strong scattering effect is largely dependent on the particle size, which can be theoretically explained as follows. When the size of sphere is comparable to the incident-light wavelength, the Mie's scattering occurs. Theoretically, the scattered wave is found to be necessary to obtain the right boundary conditions between incident wave and the field inside the sphere. For an incident light wavelength λ, the scattering behavior of a system which consists of dispersed spherical particles can be fully described by the radius of sphere r and the complex refractive index m. The complex Mie coefficients a_n and b_n can be deduced by the complex Bessel-Riccatti functions ψ and ζ

$$a_n = \frac{\psi'_n(mx)\psi_n(x) - m\psi_n(mx)\psi'_n(x)}{\psi'_n(mx)\zeta_n(x) - m\psi_n(mx)\zeta'_n(x)}$$

$$b_n = \frac{m\psi'_n(mx)\psi_n(x) - \psi_n(mx)\psi'_n(x)}{m\psi'_n(mx)\zeta_n(x) - \psi_n(mx)\zeta'_n(x)}$$

where the size parameter x is taken as: $x = 2\pi r/\lambda$.

The Mie coefficients a_n and b_n are functions with numerous poles in the complex plane. The scattering, absorption, and extinction efficiencies are given by

$$Q_{Sca} = \frac{2}{x^2}\sum_{n=1}^{\infty}(2n+1)\,(|a_n|^2 + |b_n|^2)$$

$$Q_{Abs} = Q_{Ext} - Q_{Sca}$$

$$Q_{Ext} = \frac{2}{x^2}\sum_{n=1}^{\infty}(2n+1)\,\mathrm{Re}(a_n + b_n)$$

Therefore, the scattering cross section exhibits a number of resonances for a given particle size; at these wavelengths, the scattering is very efficient.[29,30]

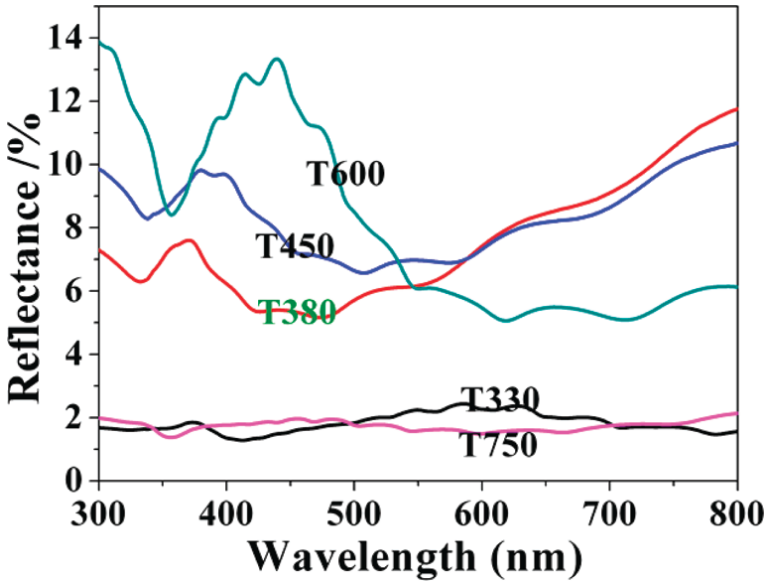

Figure 2.8 The UV-visible reflectance spectra of the TiO_2 suspensions obtained after the H_2 evolution test to detect the scattering resonant peaks of the TiO_2 spheres.

To verify the existence of the scattering effect in the H_2 evolution process, the TiO_2 suspensions obtained after the H_2 evolution test were used to check the scattering

resonant peaks by the UV-visible reflectance spectra from 300 to 800 nm.[25, 31] As shown in Figure 2.8, the experimental results reveal that the scattering effect for the various sized TiO_2 spheres in the incident light spectrum are obviously different. The TiO_2 sample with diameter of 380 nm exhibits the strong resonant peak around 366 nm, indicating that the incident light strongly scatters on the 380 nm sized TiO_2 sphere at wavelength around 366 nm. The scattered light then transfers to and is absorbed by the neighbored spheres, thus inducing more photoexcited electrons to reduce the H^+ ions into H_2 molecules. For TiO_2 spheres, only for the light with wavelengths shorter than the absorption edge (λ < 387 nm), scattering and absorption is effective. As to the TiO_2 spheres with diameters of 450 and 600 nm, the peaks of scattering resonances locate at 400 and 440 nm, thus the scattering effects are relatively limited to the enhancement of light absorption for TiO_2. For the 750 nm sized TiO_2 sample, a very weak and broad peak between 350 and 600 nm can be detected with careful observation. The weak scattering resonance peak might be attributed to the low scattering coefficient reported by Thiele and his coworkers.[32] In the photocatalytic H_2 evolution process, more light can be absorbed by the TiO_2 samples, more electrons will be excited and take part in the H^+ reduction reaction, thus lead to a higher H_2 output efficiency. Since TiO_2 sample with diameter of 380 nm exhibits the strongly effective scattering effect in the light-absorption region of TiO_2, more light will be scattered and absorbed by the TiO_2, thus the light utilization efficiency will be largely enhanced followed with the superior photocatalytic activity, which is well in accordance with our photocatalytic tests that T380 showed the higher photocatalytic activity of H_2 evolution compared with other TiO_2 samples (T330, T450, T600, and T750). In conclusion, only the scattering and absorption happened in the light absorption region of TiO_2 can make great contribution

to the effective light-utilization efficiency followed with the enhancement of photocatalytic performance.

2.3.5 Photoelectrochemical Properties of the TiO_2 Spheres

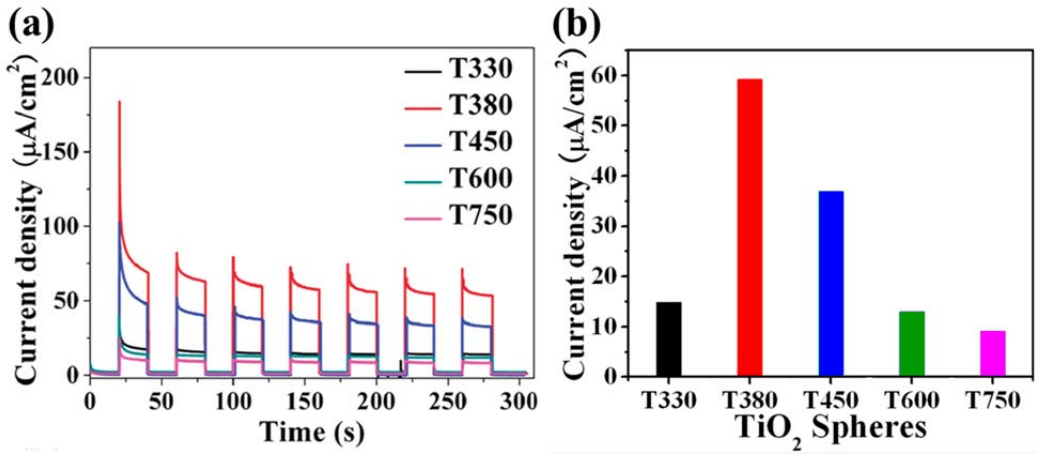

Figure 2.9 (a) The photocurrent curves (*I* - *t*) of the as-prepared TiO_2 photoanodes measured under UV-visible light irradiation (λ > 300 nm); (b) the comparison of the photoelectrochemical properties of the TiO_2 thin films samples.

In order to further confirm that the photon-to-electron conversion efficiency of the TiO_2 sphere is affected by the size-dependent Mie's scattering effect, the photoelectrochemical measurements of the TiO_2 photoanodes have been conducted. Figure 2.9a shows the photocurrent-time (*I* - *t*) curves measured with a three-electrode mode and 0.1 M Na_2SO_4 solution as the electrolyte. Under a bias potential of 0.6 V, the photocurrent densities of the TiO_2 spheres are 14.9, 59.2, 36.9, 13.0, and 9.2 $\mu A/cm^2$ for T330, T380, T450, T600, and T750, respectively, in which the photocurrent intensity of T380 is the highest (Figure 2.9b), indicating that T380 has the best photon-to-electron conversion efficiency. This result is consistent with the results from the photocatalytic H_2 evolution tests. In the photocatalytic H_2 evolution process, the photoexcited electrons

will reduce the protons (H^+) into H_2, thus an enhanced light-utilization efficiency followed with the better photon-to-electron conversion performance might result in a superior output efficiency of H_2.

Table 2.1 The BET surface areas, photocatalytic activities, and photoelectrochemical properties of the as-prepared TiO_2 spheres.

	T330	**T380**	**T450**	**T600**	**T750**
BET surface area (m^2/g)	13.8	9.4	10.1	10.2	8.8
Amounts of H_2 evolution (μmol/h)	76	265	94	136	131
Photocurrent density ($\mu A/cm^2$)	14.9	59.2	36.9	13.0	9.2

2.4 Conclusion

In summary, the Mie's scattering effect was introduced into the application of photocatalytic H_2 evolution over TiO_2 spheres. TiO_2 spheres with different diameters (330-750 nm) were fabricated to investigate the correlation between the particle size and the scattering effect. In contrast to the 450 and 600 nm sized TiO_2 spheres, the TiO_2 with a diameter of 380 nm exhibited the strongly efficient scattering effect in the light absorption region of TiO_2, thus leading to a higher light-utilization efficiency, followed with a considerable enhancement of the photocatalytic activity. This study proposes a novel strategy that coupling the effect of Mie's scattering into the light absorption region of TiO_2 via morphological modulation to improve the photocatalytic performance in the H_2 evolution. Moreover, it will provide a promising approach to effectively enhance the light utilization efficiency for other semiconductor

photocatalysts, especially for the visible-light-driven photocatalysts with the optimized diameter.

Reference:

(1) Tong, H.; Ouyang, S. X.; Bi, Y. P.; Umezawa, N.; Oshikiri, M.; Ye, J. H. *Adv. Mater.* **2012**, *24*, 229.

(2) Hoffmann, M. R.; Martin, S. T.; Choi, W. Y.; Bahnemann, D. W. *Chem. Rev.* **1995**, *95*, 69.

(3) Linsebigler, A. L.; Lu, G. Q.; Yates, J. T. *Chem. Rev.* **1995**, *95*, 735.

(4) Zou, Z. G.; Ye, J. H.; Sayama, K.; Arakawa, H. *Nature* **2001**, *414*, 625.

(5) Ouyang, S. X.; Ye, J. H. *J. Am. Chem. Soc.* **2011**, *133*, 7757.

(6) Fujishima, A.; Honda, K. *Nature* **1972**, *238*, 37.

(7) Yang, H. G.; Sun, C. H.; Qiao, S. Z.; Zou, J.; Liu, G.; Smith, S. C.; Cheng, H. M.; Lu, G. Q. *Nature* **2008**, *453*, 638.

(8) Asahi, R.; Morikawa, T.; Ohwaki, T.; Aoki, K.; Taga, Y. *Science* **2001**, *293*, 269.

(9) Ahmed, A. Y.; Kandiel, T. A.; Oekermann, T.; Bahnemann, D. *J. Phys. Chem. Lett.* **2011**, *2*, 2461.

(10) Hensel, J.; Wang, G. M.; Li, Y.; Zhang, J. Z. *Nano Lett.* **2010**, *10*, 478.

(11) Zhao, W.; Ma, W. H.; Chen, C. C.; Zhao, J. C.; Shuai, Z. G. *J. Am. Chem. Soc.* **2004**, *126*, 4782.

(12) Chen, X. Q.; Ye, J. H.; Ouyang, S. X.; Kako, T.; Li, Z. S.; Zou, Z. G. *ACS Nano* **2011**, *5*, 4310.

(13) Li, H. X.; Bian, Z. F.; Zhu, J.; Zhang, D. Q.; Li, G. S.; Huo, Y. N.; Li, H.; Lu, Y.

F. *J. Am. Chem. Soc.* **2007**, *129*, 8406.

(14) Yu, J. C.; Yu, J. G.; Ho, W. K.; Jiang, Z. T.; Zhang, L. Z. *Chem. Mater.* **2002**, *14*, 3808.

(15) Yu, J. C.; Ho, W. K.; Yu, J. G.; Yip, H.; Wong, P. K.; Zhao, J. C. *Environ. Sci. Technol.* **2005**, *39*, 1175.

(16) Ren, W. J.; Ai, Z. H.; Jia, F. L.; Zhang, L. Z.; Fan, X. X.; Zou, Z. G. *Appl. Catal. B Environ.* **2007**, *69*, 138.

(17) Mie, G. *Ann. Phys.* **1908**, *330*, 377.

(18) Koo, H. J.; Park, J.; Yoo, B.; Yoo, K.; Kim, K.; Park, N. G. *Inorg. Chim. Acta* **2008**, *361*, 677.

(19) Wu, X.; Lu, G. Q.; Wang, L. Z. *Energ. Environ. Sci.* **2011**, *4*, 3565.

(20) Yu, I. G.; Kim, Y. J.; Kim, H. J.; Lee, C.; Lee, W. I. *J. Mater. Chem.* **2011**, *21*, 532.

(21) Usami, A. *Chem. Phys. Lett.* **1997**, *277*, 105.

(22) Retsch, M.; Schmelzeisen, M.; Butt, H. J.; Thomas, E. L. *Nano Lett.* **2011**, *11*, 1389.

(23) Tang, F. Q.; Fudouzi, H.; Zhang, J. X.; Sakka, Y. *Scripta Mater.* **2003**, *49*, 735.

(24) Sing, K. S. W.; Everett, D. H.; Haul, R. A. W.; Moscou, L.; Pierotti, R. A.; Rouquerol, J.; Siemieniewska, T. *Pure Appl. Chem.* **1985**, *57*, 603.

(25) Bohren, C. F.; Huffman, D. R. *Wiley, New York* **1983**, 103.

Chapter 3 Porous-Structured Cu_2O/TiO_2 Nanojunction Material toward Efficient CO_2 Photoreduction

3.1 Introduction

The reduction of carbon dioxide (CO_2) into hydrocarbon fuels (e.g. CH_4) is a promising solution to both the global warming and energy shortage.[1-6] Generally, the gas-phase CO_2 photoreduction comprises two steps: CO_2 adsorption and CO_2-to-hydrocarbon conversion. Firstly, CO_2 molecular adsorb on the surface of photocatalyst; then, the photo-generated electrons migrate from bulk to the surface to reduce CO_2 into CH_4 or other hydrocarbons.[7-10] Nevertheless, in the second step, a large proportion of photogenerated electrons recombine with the holes in the bulk and can not migrate to the surface to take part in the photocatalytic reaction, leading to a poor photocatalytic activity.[11,12] Therefore, in order to achieve a higher CO_2 conversion efficiency, it requires the photocatalyst not only have strong ability to capture CO_2 on its surface but also can motivate more electrons migrate to the surface reactive sites to reduce CO_2.

To effectively suppress the photogenerated electron-hole recombination probability, one of the most effective methods is to fabricate photocatalysts with heterojunction structure which can facilitate charge rectification and induce faster carrier migration.[13-17] Herein, we will focus on the Cu_2O/TiO_2 p-n heterojunction, in which Cu_2O is a typical p-type semiconductor with band gap of 2.2 eV [18-20] and TiO_2 is a popular n-type semiconductor with band gap of 3.2 eV.[21,22] As shown in Figure 3.1, the band structures of the Cu_2O and TiO_2 matched well with each other, in which the conduction band of Cu_2O is higher than that of TiO_2, while the valence band of TiO_2 is

lower than that of Cu_2O.[1,23,24] Under UV-visible light irradiation, the electrons on the conduction band of Cu_2O will quickly move to the conduction band of TiO_2, whereas the holes on the valence band of TiO_2 will transfer to the valence band of Cu_2O, effectively realizing the charge separation process.[24] More interestingly, a p-n junction effect is supposed to exist in the interface region between the p-type Cu_2O and n-type TiO_2 in the Cu_2O/TiO_2 heterojunction, which can further facilitate the charge transfer between Cu_2O and TiO_2.[25,26] In parallel, if we make the particle size of the material smaller in several nanometers, the transfer distance of the electrons and holes from bulk to the surface reactive sites can largely be shorten.[27] Therefore, it is expected that the Cu_2O/TiO_2 nanojunction material will exhibit excellent charge separation properties.

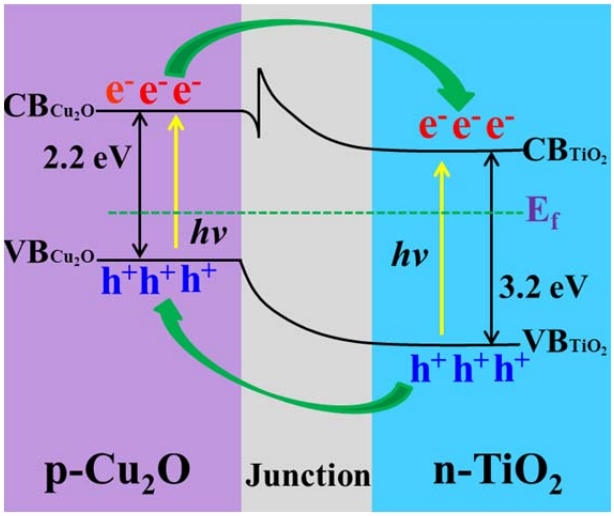

Figure 3.1 Schematic illustration of the charge transfer process happened in the Cu_2O/TiO_2 nanojunction under UV-visible light irradiation.

Moreover, due to their outstanding structural characteristics such as good adsorption ability and large surface area, which not only facilitate the reactant adsorption but also can offer more reaction sites in the photocatalytic reaction, porous-structured materials

have been largely adopted in the field of photocatalysis.[2,28] We recently demonstrated that mesoporous structure can promote CO_2 adsorption on the surface of photocatalyst, thus significantly enhance the photocatalytic activity.[29,30] Inspired by the above studies, considering both the effect of photogenerated carriers and gas adsorption properties, we suggest that porous-structured Cu_2O/TiO_2 nanojunction materials will be a good candidate for the CO_2 photoreduction.

There were some studies carried out on the Cu_2O/TiO_2 heterojunctions before, which have confirmed that the Cu_2O/TiO_2 heterojunction can enhance the charge separation efficiency and lead to a higher photocatalytic activity. For instance, Lalitha et al. reported that Cu_2O/TiO_2 nanocomposites with size about 20-40 nm exhibit higher activity than pure TiO_2 in the H_2 evolution;[31] Chu et al. designed a $Cu_2O@TiO_2$ core-shell structure, and this material shows an excellent photocatalytic activity in the 4-nitrophenol degradation;[24] Yang et al. deposited the Cu_2O nanowire on the TiO_2 nanotube and found that the Cu_2O/TiO_2 composites exhibit 2 times higher activity of the pure TiO_2 nanotube.[32] Nevertheless, to date, no study is focused on the porous-structured Cu_2O/TiO_2 material, especially in the CO_2 photoreduction. Herein, we demonstrate a facile method to synthesize porous-structured Cu_2O/TiO_2 nanojunction material in the size less than 10 nm via loading Cu_2O nanoparticles on the network of TiO_2 porous materials. As a promising material, the Cu_2O/TiO_2 nanojunction exhibits marked performance in the CO_2 photoreduction test. The simultaneously enhanced charge separation efficiency and CO_2 adsorption make the great contributions to the high photocatalytic activity. To the best of our knowledge, this is the first report about the porous-structured Cu_2O/TiO_2 nanojunction materials in the application of CO_2 photoreduction.

3.2 Experimental Section

3.2.1 Synthesis of Porous-Structured TiO_2

In a typical synthetic procedure, 0.5 mL of titanium tetrachloride ($TiCl_4$) was firstly dissolved into 30 mL of benzyl alcohol containing 2 mL of ethanol to obtain the yellowish solution as the Ti precursor. After that, the above solution was transferred to a Teflon vessel and heated at 200 ^oC for 40 min. After reaction, the resulting product was collected, thoroughly washed with ethanol and deionized water, and finally dried in the oven at 70 ^oC for 6 h.

3.2.2 Synthesis of Porous-Structured Cu_2O/TiO_2 Composite

The schematic illustration of the reaction process is shown in Figure 3.2. Typically, 2 mmol of the above-prepared porous TiO_2 powders were firstly dispersed into 2 mL of ethanol via ultrasonic treatment for 15 min. Then, the TiO_2 suspension was transferred into the Teflon vessel contained with 30 mL of benzyl alcohol. After that, 0.4 mmol of copper (II) acetylacetonate ($Cu(acac)_2$) was added into the vessel, and kept stirring for another 15 min. Finally, the reaction vessel was fixed into the microwave oven, after the microwave-solvothermal treatment at 200 ^oC for 40 min, the final Cu_2O/TiO_2 heterojuntions can be obtained.

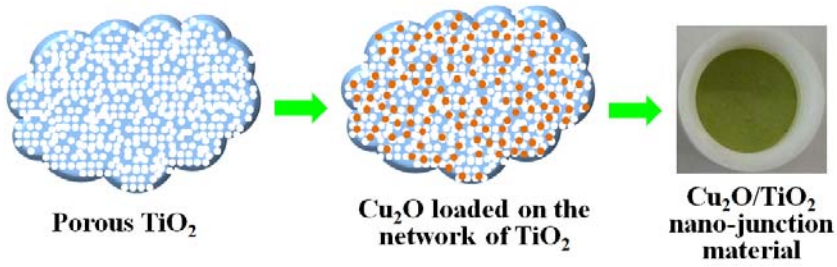

Figure 3.2 Schematic illustration of the formation process of the Cu_2O/TiO_2 heterojunctions.

In comparison, the Pt loaded TiO_2 was prepared via photodeposition of Pt (1 wt %) on the porous TiO_2 in the mixed solution (50 mL of methanol and 220 mL of water) under UV-visible light irradiation for 2 h. $HPtCl_4$ was used as the Pt precursor, and the light source is a 300 W Xenon arc lamp. To remove the surface adsorbed organics, the Pt loaded TiO_2 was finally calcined at 400 ^oC for 2 h. This sample is denoted as Pt-TiO_2.

3.2.3 Characterization

X-ray diffraction patterns were recorded on a Rigaku Multiflex diffractometer (RINT 2000; Rigaku Corp. Japan) with monochromatized Cu Ka radiation (λ=1.54178 Å). The size and morphology of the samples were observed with a transmission electron microscope (TEM, JEM-200 CX, JEOL) operating at 200 kV. The Brunauer-Emmett-Teller (BET) surface areas were deducted by a surface area analyser (Autosorb-1C, Quantachrome Co., USA) with nitrogen absorption at 77 K. UV-visible absorption spectra were measured on a UV-visible spectrophotometer (UV-2500 PC, Shimadzu Co., Japan). The CO_2 pulse chemisorption tests were carried out on Micromeritics Autochem Ⅱ Chemisorption Analyzer at 35 ^oC with a fixed volume loop of 0.05 mL.

3.2.4 CO_2 Photoreduction Test

In the photocatalytic reduction of CO_2, 40 mg of the sample without any cocatalyst was uniformly dispersed on a glass reactor with a base area of 8.1 cm^2. A 300 W Xenon arc lamp was used as the light source for the photocatalytic reaction. The volume of the reaction system was around 390 mL. The reaction setup was vacuum treated several times, and then high-purity CO_2 gas was introduced into the reaction system to achieve

a pressure of 80 kPa. Deionized water (3 mL) was injected into the reaction system. During the irradiation, about 0.5 mL of gas was taken from the reaction cell at given intervals for subsequent CH_4 concentration analysis using a gas chromatograph (GC-14B, Shimadzu) equipped with a flame ionized detector (FID) and methanizer.

3.3 Results and Discussions

3.3.1 Crystal Structure and Morphology

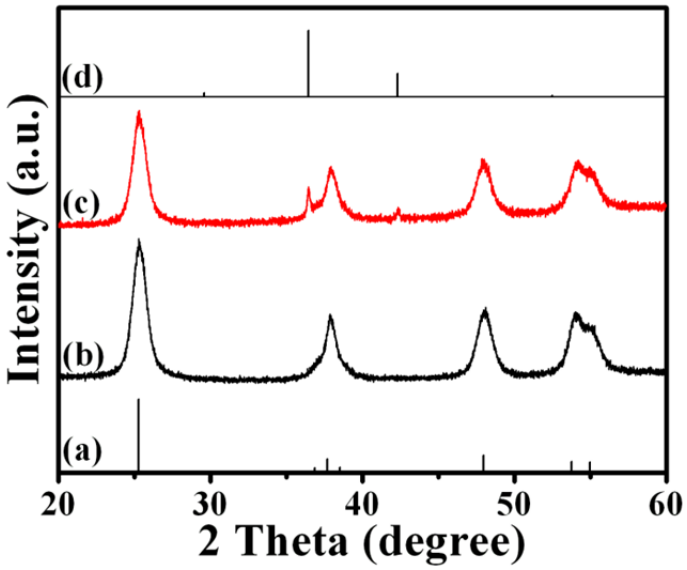

Figure 3.3 XRD patterns of the standard anatase TiO_2 (JCPDS no. 71-1167) (a), porous TiO_2 (b), porous Cu_2O/TiO_2 nanojunction material (c), and the standard cubic Cu_2O (JCPDS no. 78-2076) (d).

To characterize the crystal structure of the samples, XRD measurements were carried out on the as-prepared TiO_2 and Cu_2O/TiO_2 heterojunction as shown in Figure 3.3. The diffraction peaks at 25.26, 37.83, 47.90, 53.91, and 54.99° can be assigned to (101), (004), (200), (105), and (211) planes of anatase TiO_2 (JCPDS no. 71-1167) (Figure 3.3a), respectively. Thus, as shown in Figure 3.3b, our prepared TiO_2 is well-indexed to

the pure anatase TiO_2. For the Cu_2O/TiO_2 heterojunction (Figure 3.3c), besides the peaks matched well with the anatase TiO_2, the relative peak around at 36.22° is indexed to the diffraction of (111) plane of the cubic Cu_2O (JCPDS no. 78-2076) (Figure 3.3d), indicating that both TiO_2 and Cu_2O coexist in the Cu_2O/TiO_2 heterojunction.

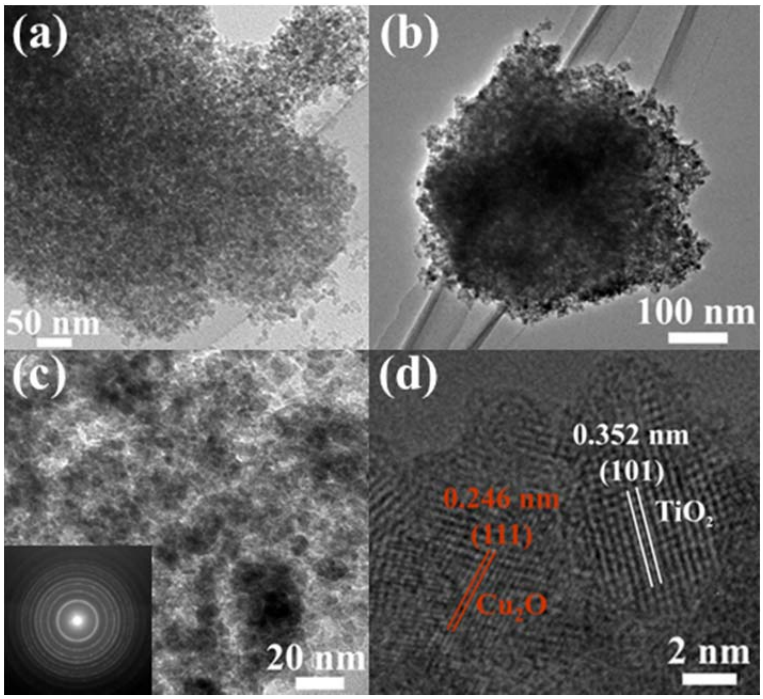

Figure 3.4 TEM image of pure TiO_2 (a), TEM (b, c), SAED pattern (inset of c), and HRTEM (d) images of the porous-structured Cu_2O/TiO_2 nanojunction material.

The size and morphology of the TiO_2 and Cu_2O/TiO_2 heterojunction were observed by TEM. As shown in Figure 3.4a, TiO_2 is composed of large amounts of ultrafine nanoparticles with size about several nanometers, and these particles aggregated together to from the porous structure. The Cu_2O/TiO_2 heterojunction material exhibits the similar morphology to that of TiO_2 (Figure 3.4b), which also consists of ultrafine nanoparticles and those nanoparticles agglomerated together to form the porous structure (Figure 3.4c). The corresponding selected area electron diffraction (SAED)

pattern of the agglomerated nanoparticles is shown in the inset of Figure 3.4c, in which the clear diffraction rings indicate that the Cu_2O/TiO_2 nanojunction material is well crystallized. The well-designed interface between Cu_2O and TiO_2 nanoparticles can be observed by the HRTEM image as shown in Figure 3.4d. The lattice spacing of the two nanoparticles are measured to be 0.246 and 0.352 nm, which are corresponding to the (111) crystal plane of cubic Cu_2O and (101) crystal plane of anatase TiO_2, respectively. It is clear that the Cu_2O nanoparticle (~ 5 nm) and TiO_2 nanoparticle (~ 6 nm) are closely connected with each other, indicating that our prepared heterojunction material exhibits a good nanojunction interface.

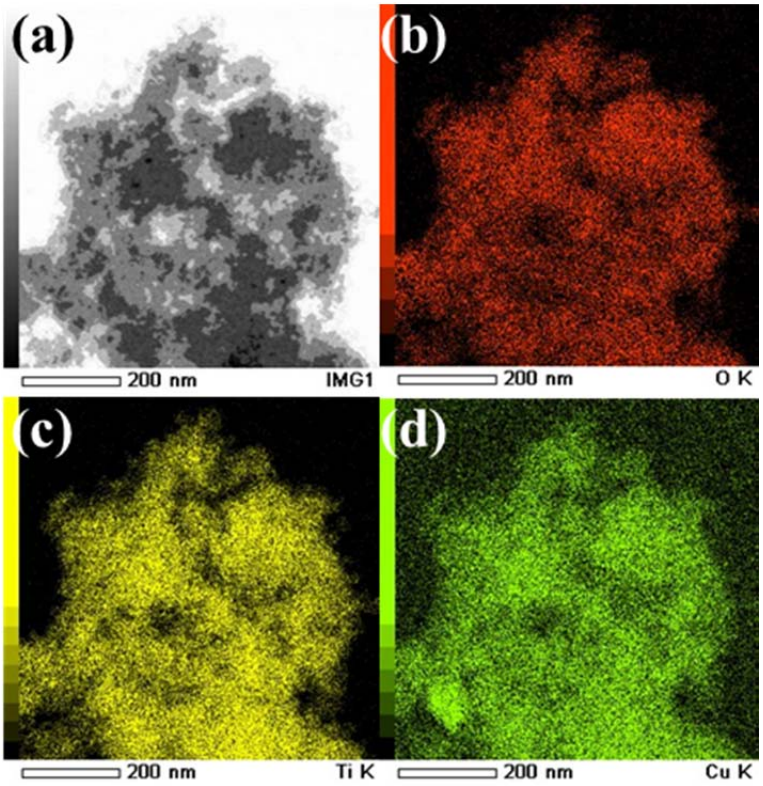

Figure 3.5 EDS elemental mapping analysis of the Cu_2O/TiO_2 nanojunction material. (a) survey, (b) O element, (c) Ti element, and (d) Cu element.

Furthermore, the energy-dispersive X-ray spectroscopy (EDS) elemental mapping

analyses (Figure 3.5) reveal that the distribution of both Ti and Cu is homogeneous. Therefore, we can conclude that the as-prepared Cu_2O/TiO_2 nanojunction has a good nanojunction structure, in which TiO_2 nanoparticles and Cu_2O nanoparticles are closely contacted with each other. Such a well-designed interface is beneficial for the charge separation between Cu_2O and TiO_2.

3.3.2 Porous Structure

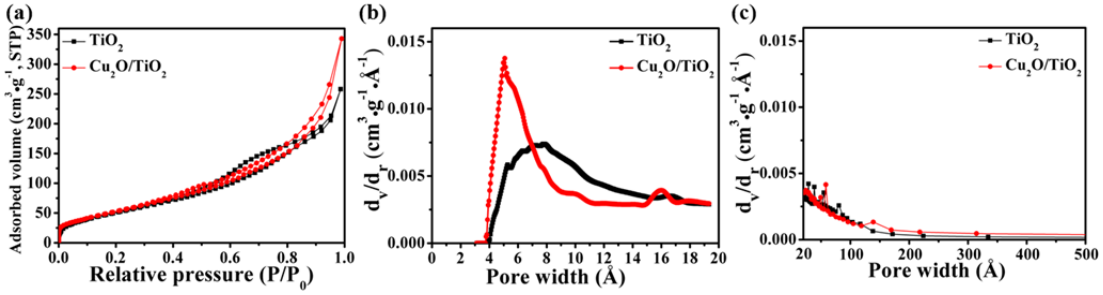

Figure 3.6 N_2 adsorption-desorption isotherms (a), pore size distributions analysed by the HK method (b) and BJH method (c) of the prepared TiO_2 and Cu_2O/TiO_2 nanojunction material.

Figure 3.6a shows the nitrogen adsorption-desorption isotherms of the prepared TiO_2 and Cu_2O/TiO_2 nanojunction. The adsorption isotherms of both TiO_2 and Cu_2O/TiO_2 nanojunction can be classified as type IV with a hysteresis loop of type H1, which is associated with porous materials.[33] The pores are resulted from the agglomeration of nanoparticles, which is well in accordance with the TEM images shown in Figure 3.4. In parallel, the pore size distributions of TiO_2 and Cu_2O/TiO_2 nanojunction are also listed, in which the micropores below 2 nm were analysed by the Horvath-Kawazoe (HK) method (Figure 3.6b), and the mesopores above 2 nm were studied by the Barrett-Joyner-Halenda (BJH) method (Figure 3.6c). It is obvious that our developed

Cu_2O/TiO_2 nanojunction material exhibits a sharp pore size distribution around 4~8 Å (Figure 3.6b), indicating that the Cu_2O/TiO_2 nanojunction material is mainly in micro-pores. And the size distribution of Cu_2O/TiO_2 nanojunction is sharper than the pure TiO_2 below 2 nm (Figure 3.6b) and similar to TiO_2 in the range larger than 2 nm (Figure 3.6c). As shown in Figure 3.2, the Cu_2O/TiO_2 nanojunction is fabricated via loading Cu_2O nanoparticles on the network of porous TiO_2; after loading some ultrafine Cu_2O nanoparticles on the TiO_2, parts of the pores in TiO_2 might be partially filled, leading to a smaller pore size.

Table 3.1 Total pore volumes, BET surface areas, as well as the amounts of adsorbed CO_2 of the prepared TiO_2, Cu_2O/TiO_2 nanojunction, and the commercial P25 TiO_2.

	pore volume (cm^3/g)	**surface area (m^2/g)**	**CO_2 adsorption (mL/g)**
TiO_2	0.21	198	0.12
Cu_2O/TiO_2	0.29	206	0.27
P25	0.10	51	0.05

Meanwhile, as shown in Table 3.1, the total pore volumes and Brunauer-Emmett-Teller (BET) surface areas are recorded to be (0.21 $cm^3 \bullet g^{-1}$, 198 $m^2 \bullet g^{-1}$) and (0.29 $cm^3 \bullet g^{-1}$, 206 $m^2 \bullet g^{-1}$) for TiO_2 and Cu_2O/TiO_2 nanojunction, respectively. Both the large total pore volume and surface area strongly support the fact that our developed Cu_2O/TiO_2 nanojunction has the porous structure, which is beneficial for the CO_2 adsorption in the photocatalytic reaction. In addition, to investigate the CO_2 adsorption ability on the porous TiO_2 and Cu_2O/TiO_2 nanojunction, the CO_2 pulse chemisorption tests were carried out. As shown in Figure 3.7 and Table 3.2, the

amounts of adsorbed CO_2 molecular are calculated to be 0.12 and 0.27 mL/g for our developed porous TiO_2 and Cu_2O/TiO_2 nanojunction, respectively. In comparison, the commercial P25 TiO_2 powder in the size of 25 nm and with lower surface area (51 m^2/g) as well as smaller total pore volume (0.10 cm^3/g) is also tested; P25 exhibits a relatively limited CO_2 adsorption, about 0.05 mL/g. Those above results further experimentally confirmed that the porous structure with a larger total pore volume is beneficial for the CO_2 adsorption, especially in the case of smaller pore size.

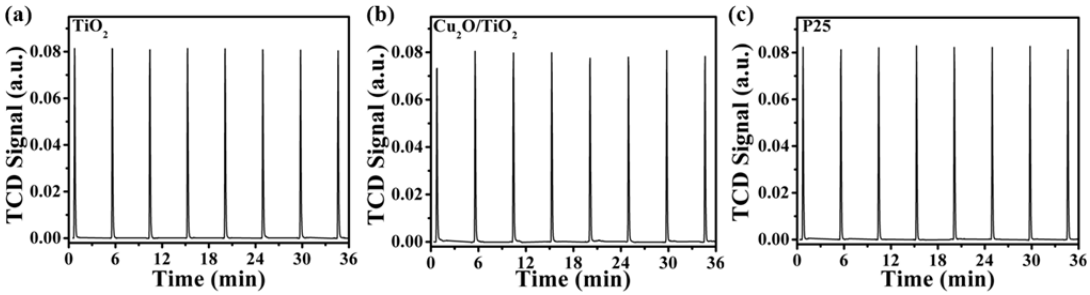

Figure 3.7 CO_2 pulse chemisorption tests over TiO_2 (a), Cu_2O/TiO_2 nanojunction (b), as well as the commercial P25 TiO_2 powder (c). (TCD: thermal conductivity detector)

Table 3.2 Peak areas and calculated adsorption amounts of CO_2 in CO_2 pulse chemisorption measurements.

	peak areas (a.u.)								CO_2 adsorption (ml/g)
	1	2	3	4	5	6	7	8	
TiO_2	0.0105	0.0109	0.0109	0.0109	0.0108	0.0109	0.0109	0.0108	**0.12**
Cu_2O/TiO_2	0.0102	0.0108	0.0109	0.0108	0.0109	0.0109	0.0109	0.0109	**0.27**
P25	0.0107	0.0108	0.0108	0.0109	0.0108	0.0108	0.0108	0.0108	**0.05**

3.3.3 Optical Properties of Cu_2O/TiO_2 Heterojunction

The UV-visible absorption spectra of the prepared TiO_2 and Cu_2O/TiO_2 heterojunction are shown in Figure 3.8. It can be clearly seen that the absorption edge of TiO_2 is around 380 nm; as for Cu_2O/TiO_2 heterojunction, except for the absorption edge (nearly 388 nm) of pure TiO_2, another absorption band edge around 510 nm can also be detected, which is resulted from the existence of Cu_2O in the hybrid Cu_2O/TiO_2 material.

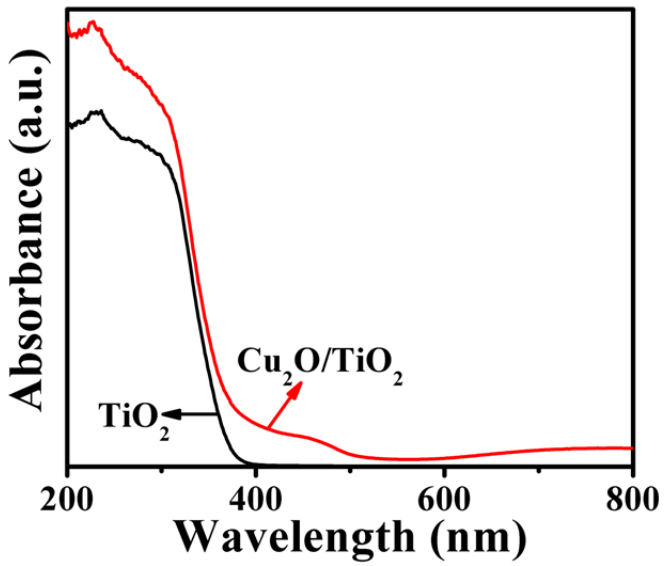

Figure 3.8 UV-visible absorption spectra of the prepared TiO_2 and Cu_2O/TiO_2 nanojunction.

3.3.4 CO_2 Photoreduction

The CO_2 photoreduction tests of the as-prepared TiO_2 and Cu_2O/TiO_2 nanojunction material were evaluated under UV-visible light irradiation (Figure 3.9a). For purpose of comparison, the Pt-loaded porous TiO_2 (Pt-TiO_2) and commercial P25 were also tested under the same experimental conditions. As shown in Figure 3.9b, the CH_4 evolution rates are calculated to be 2.4, 28.4, 3.2, and 3.7 $ppm \cdot g^{-1} \cdot h^{-1}$ for TiO_2, Cu_2O/TiO_2 nanojunction, Pt-TiO_2 and P25, respectively. Among those samples, the Cu_2O/TiO_2

nanojunction exhibits the highest photocatalytic activity, about 12, 9, and 7.5 times higher of TiO_2, Pt-TiO_2 and P25, respectively. Besides CH_4, trace amounts of CO can also be detected. In addition, controlled experiments show that no CH_4 was evolved when the photocatalytic reaction was carried out in the dark or irradiated in the absence of photocatalyst, revealing that the reduction of CO_2 is driven by light irradiation over the photocatalyst.

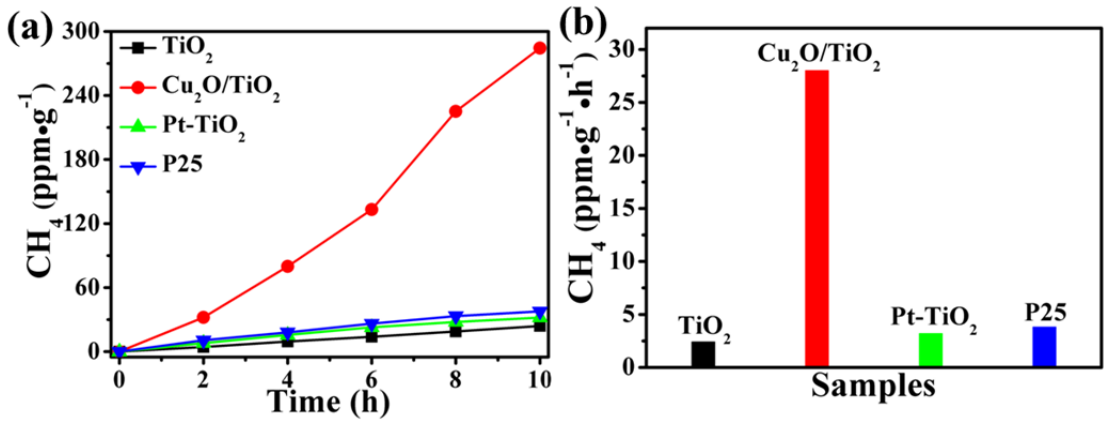

Figure 3.9 (a) CH_4 evolution over the prepared TiO_2, Cu_2O/TiO_2 nanojunction, Pt-TiO_2, and P25 under UV-visible light irradiation (λ > 300 nm) in 10 hours. (b) Average CH_4 evolution rates of the prepared TiO_2, Cu_2O/TiO_2 nanojunction, Pt-TiO_2, and P25.

3.3.5 Discussion about the Enhancement of Photocatalytic Activity

The well-designed porous-structure combined with the closely contacted interface of the Cu_2O/TiO_2 nanojunction plays important roles in enhancing the photocatalytic activity. Firstly, in contrast to the pure TiO_2, the superior activity of Cu_2O/TiO_2 material can be attributed to its well-designed nanojunction structure. As shown in Figure 3.10a, once excited, the electrons will transfer from Cu_2O to and accumulate on the TiO_2, while the holes will move from TiO_2 to Cu_2O, to realize the charge separation. While

for pure TiO_2 (Figure 3.10b), the electrons and holes is easy to recombine together on the surface, leading to a poor charge separation efficiency and lower photocatalytic activity.

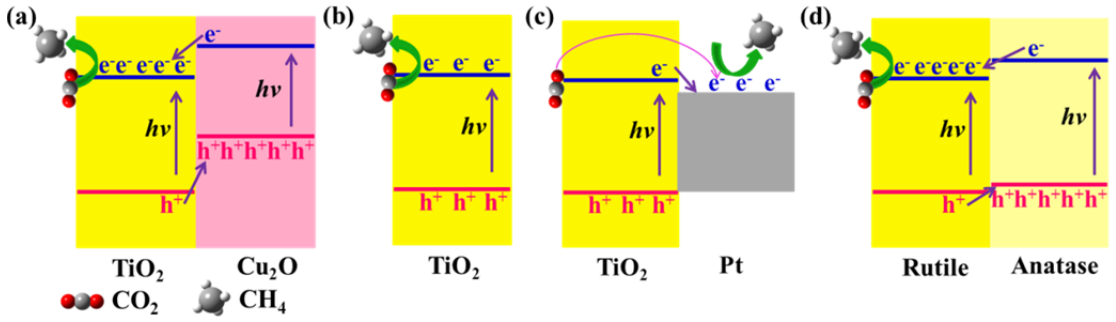

Figure 3.10 Schematic illustration of the charge transfer and CO_2 reduction processes happened on the Cu_2O/TiO_2 nanojunction (a), porous TiO_2 (b), Pt loaded porous TiO_2 (c), as well as the commercial P25 powder (d) under UV-visible light irradiation.

Then, after Pt loading, the photocatalytic activity of Pt-TiO_2 is slightly enhanced than pure TiO_2, but still lower than that of Cu_2O/TiO_2 nanojunction. As shown in Figure 3.10c, Pt has a lower Fermi energy than TiO_2, so Pt-TiO_2 can enhance the charge separation efficiency via pushing the photogenerated electrons transfer from the conduction band of TiO_2 to the surface Pt sites; then, the accumulated electrons on the Pt sites reduce CO_2 into CH_4. However, most of the CO_2 molecular is adsorbed on the porous TiO_2, and to finish the whole CO_2 photoreduction process, either the CO_2 molecular on the TiO_2 surface or the accumulated electrons on the Pt sites need to migrate for dozens of nanometers; during this migration, the charges (electrons and holes) are easily recombined. In the case of our-developed Cu_2O/TiO_2 nanojunction, as shown in Figure 3.10a, both the CO_2 adsorption and electrons' accumulation simultaneously happened on the TiO_2 surface, thus the distance for electron migration

become shorter and ratio for recombination on the surface becomes lower, leading to higher activity.

Furthermore, compared with commercial P25 TiO_2 powder which is composed of 80% of anatase and 20% of rutile (Figure 3.10d), our developed Cu_2O/TiO_2 nanojunction exhibits 7.5 times higher activity in the CH_4 evolution (Figure 3.9). The higher activity of the Cu_2O/TiO_2 nanojunction in contrast to P25 might be ascribed to the porous structure and larger surface area as shown in Table 3.1, which facilitate the CO_2 adsorption (0.27 mL/g for Cu_2O/TiO_2 nanojunction *vs*. 0.05 mL/g for P25) and can offer more reaction active sites. On the other hand, our-designed Cu_2O/TiO_2 nanojunction owns a smaller particle size (about 5~8 nanometer) than that of P25 TiO_2 (around 25 nm). With a smaller particle size, the migration distance for the electrons and holes from bulk to surface can largely be shorten, which can somehow inhibit the charge recombination in the bulk.

3.4 Conclusion

We have successfully prepared the porous-structured Cu_2O/TiO_2 nanojunction material in the size of several nanometers. The well-designed nanojunction structure facilitates the charge separation between Cu_2O and TiO_2; while the porous structure is beneficial for the CO_2 adsorption. Those combined properties endow the Cu_2O/TiO_2 nanojunction exhibits marked photocatalytic performance in the CO_2 photoreduction, about 12, 9, and 7.5 times higher of the TiO_2, Pt-TiO_2, and the commercial P25 TiO_2, respectively. This study demonstrates that constructing of porous-structure coupled with nanojunction is an interesting strategy to enhance the photocatalytic activity of CO_2 photoreduction. We anticipate that this concept can provide a versatile route to fabricate

other porous-structured heterojunction materials for higher solar-to-energy conversion efficiency.

Reference:

(1) Roy, S. C.; Varghese, O. K.; Paulose, M.; Grimes, C. A. *ACS Nano* **2010**, *4*, 1259.

(2) Yan, S. C.; Ouyang, S. X.; Gao, J.; Yang, M.; Feng, J. Y.; Fan, X. X.; Wan, L. J.; Li, Z. S.; Ye, J. H.; Zhou, Y.; Zou, Z. G. *Angew. Chem. Int. Ed.* **2010**, *49*, 6400.

(3) Tu, W. G.; Zhou, Y.; Liu, Q.; Tian, Z. P.; Gao, J.; Chen, X. Y.; Zhang, H. T.; Liu, J. G.; Zou, Z. G. *Adv. Funct. Mater.* **2012**, *22*, 1215.

(4) Xu, H.; Ouyang, S. X.; Li, P.; Kako, T.; Ye, J. H. *ACS Appl. Mater. Interfaces* **2013**, *5*, 1348.

(5) Chen, X. Y.; Zhou, Y.; Liu, Q.; Li, Z. D.; Liu, J. G.; Zou, Z. G. *ACS Appl. Mater. Interfaces* **2012**, *4*, 3372.

(6) Zhou, Y.; Tian, Z. P.; Zhao, Z. Y.; Liu, Q.; Kou, J. H.; Chen, X. Y.; Gao, J.; Yan, S. C.; Zou, Z. G. *ACS Appl. Mater. Interfaces* **2011**, *3*, 3594.

(7) Li, P.; Ouyang, S. X.; Kako, T.; Ye, J. H. *J. Mater. Chem. A* **2013**, *1*, 1185.

(8) Li, P.; Ouyang, S. X.; Xi, G. C.; Kako, T.; Ye, J. H. *J. Phys. Chem. C* **2012**, *116*, 7621.

(9) Liu, Q.; Zhou, Y.; Kou, J. H.; Chen, X. Y.; Tian, Z. P.; Gao, J.; Yan, S. C.; Zou, Z. G. *J. Am. Chem. Soc.* **2010**, *132*, 14385.

(10) Liu, Q.; Zhou, Y.; Tian, Z. P.; Chen, X. Y.; Gao, J.; Zou, Z. G. *J. Mater. Chem.* **2012**, *22*, 2033.

(11) Tong, H.; Ouyang, S. X.; Bi, Y. P.; Umezawa, N.; Oshikiri, M.; Ye, J. H. *Adv.*

Mater. **2012**, *24*, 229.

(12) Ouyang, S. X.; Ye, J. H. *J. Am. Chem. Soc.* **2011**, *133*, 7757.

(13) Bi, Y. P.; Ye, J. H. *Chem. Commun.* **2009**, 6551.

(14) Bi, Y. P.; Hu, H. Y.; Ouyang, S. X.; Jiao, Z. B.; Lu, G. X.; Ye, J. H. *J. Mater. Chem.* **2012**, *22*, 14847.

(15) Li, Q. Y.; Kako, T.; Ye, J. H. *Chem. Commun.* **2010**, *46*, 5352.

(16) Yao, W. F.; Zhang, B.; Huang, C. P.; Ma, C.; Song, X. L.; Xu, Q. J. *J. Mater. Chem.* **2012**, *22*, 4050.

(17) Xi, G. C.; Ouyang, S. X.; Ye, J. H. *Chem. Eur. J.* **2011**, *17*, 9057.

(18) de Jongh, P. E.; Vanmaekelbergh, D.; Kelly, J. J. *Chem. Mater.* **1999**, *11*, 3512.

(19) Ai, Z. H.; Xiao, H. Y.; Mei, T.; Liu, J.; Zhang, L. Z.; Deng, K. J.; Qiu, J. R. *J. Phys. Chem. C* **2008**, *112*, 11929.

(20) Zheng, Z. K.; Huang, B. B.; Wang, Z. Y.; Guo, M.; Qin, X. Y.; Zhang, X. Y.; Wang, P.; Dai, Y. *J. Phys. Chem. C* **2009**, *113*, 14448.

(21) Fujishima, A.; Honda, K. *Nature* **1972**, *238*, 37.

(22) Chen, X. B.; Liu, L.; Yu, P. Y.; Mao, S. S. *Science* **2011**, *331*, 746.

(23) Zhang, J. Y.; Zhu, H. L.; Zheng, S. K.; Pan, F.; Wang, T. M. *ACS Appl. Mater. Interfaces* **2009**, *1*, 2111.

(24) Chu, S.; Zheng, X. M.; Kong, F.; Wu, G. H.; Luo, L. L.; Guo, Y.; Liu, H. L.; Wang, Y.; Yu, H. X.; Zou, Z. G. *Mater. Chem. Phys.* **2011**, *129*, 1184.

(25) Lin, J. J.; Shen, J. X.; Wang, R. J.; Cui, J. J.; Zhou, W. J.; Hu, P. G.; Liu, D. O.; Liu, H.; Wang, J. Y.; Boughton, R. I.; Yue, Y. Z. *J. Mater. Chem.* **2011**, *21*, 5106.

(26) Deo, M.; Shinde, D.; Yengantiwar, A.; Jog, J.; Hannoyer, B.; Sauvage, X.; More, M.; Ogale, S. *J. Mater. Chem.* **2012**, *22*, 17055.

(27) Xu, H.; Zhang, L. Z. *J. Phys. Chem. C* **2009**, *114*, 940.

(28) Yan, S. C.; Yu, H.; Wang, N. Y.; Li, Z. S.; Zou, Z. G. *Chem. Commun.* **2012**, *48*, 1048.

(29) Zhang, N.; Ouyang, S. X.; Li, P.; Zhang, Y. J.; Xi, G. C.; Kako, T.; Ye, J. H. *Chem. Commun.* **2011**, *47*, 2041.

(30) Zhang, N.; Ouyang, S. X.; Kako, T.; Ye, J. H. *Chem. Commun.* **2012**, *48*, 1269.

(31) Lalitha, K.; Sadanandam, G.; Kumari, V. D.; Subrahmanyam, M.; Sreedhar, B.; Hebalkar, N. Y. *J. Phys. Chem. C* **2010**, *114*, 22181.

(32) Yang, L. X.; Luo, S. L.; Li, Y.; Xiao, Y.; Kang, Q.; Cai, Q. Y. *Environ. Sci. Technol.* **2010**, *44*, 7641.

(33) Sing, K. S. W.; Everett, D. H.; Haul, R. A. W.; Moscou, L.; Pierotti, R. A.; Rouquerol, J.; Siemieniewska, T. *Pure Appl. Chem.* **1985**, *57*, 603.

Chapter 4 High-Active Anatase TiO_2 Nanosheets Exposed with 95% {100} Facets toward Efficient H_2 Evolution and CO_2 Photoreduction

4.1 Introduction

Photocataysis is well-considered to be a potential solution to the worldwide energy shortage and environmental pollution, such as CO_2 photoreduction into solar fuels, photocatalytic water splitting into H_2, and photodegradation of organic pollutants.[1-4] For a photocatalyst, the photocatalytic performance is largely dependent on the surface structure because many physical and chemical processes (e.g. adsorption of reactant molecules, surface transfer of photoexcited electrons to reactant molecules, and desorption of product molecules) take place on the surface.[3-5] Peculiarly, for a crystalline TiO_2, the surface geometric (atomic arrangement and coordination) and electronic structures vary with crystal facets in different orientations, leading to various physical and chemical properties.[6] Therefore, tailored synthesis of TiO_2 single crystals with optimized reactive facets is highly desirable for promoting the photocatalytic activity.

In the case of anatase TiO_2, the shape of this material under equilibrium conditions is a slightly truncated tetragonal bipyramid enclosed with 94% of {101} surfaces (the most thermodynamically stable) and minor {001} surfaces based on the Wulff construction and theoretically calculated surface energy ({101} (0.44 J/m^2) < {100} (0.53 J/m^2) < {001} (0.90 J/m^2)).[6] Nevertheless, in the real experimental process, the facet control of anatase TiO_2 can be effectively achieved.[7] A significant breakthrough

was carried out by Yang and his co-workers, who experimentally obtained the anatase TiO_2 single crystals with majority of {001} facets.[8] Moreover, in spite of that no {100} facet can be observed in the Wulff construction model, the latest investigations have confirmed the existence of {100} facet existed as the 'belt' at the center of TiO_2 particle as shown in Figure 4.1.[9,10]

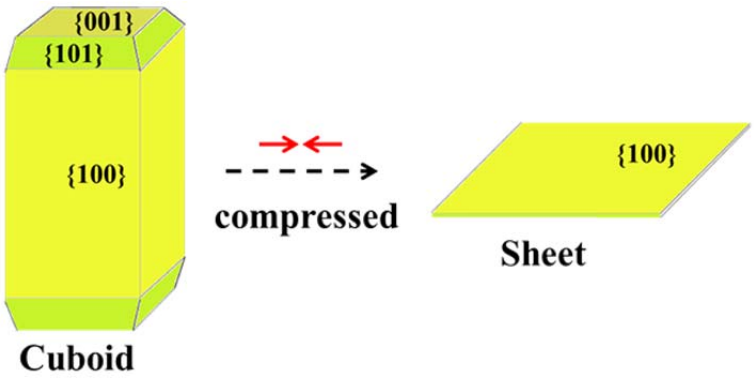

Figure 4.1 Schematic illustration of anatase TiO_2 single crystals exposed with different crystal facets.

Among the most investigated {101}, {001}, and {100} facets, {100} facet is considered to be the most active facet in the photocatalysis because of its superior surface atomic structure and electronic structure.[7,11] On the {100} surface, 100% Ti atoms are 5-coordinated Ti (Ti_{5c}), these under-coordinated Ti atoms (Ti_{5c}) can act as active sites in the photocatalytic reaction, which is beneficial for the higher photocatalytic activity.[6] In parallel, it is reported that TiO_2 sample with more {100} facet exposed owns a superior electronic band structure, in which more strongly reductive electrons can be generated on the conduction band and then transferred to the TiO_2 surface to reduce H^+ into H_2, resulting in a higher photocatalytic activity in the H_2 evolution.[7,12] Thereby, fabrication of TiO_2 single crystals exposed with more active

{100} facet will be an effective way to optimize the photocatalytic properties of anatase TiO_2, then find its promising application in the renewable energy, such as H_2 evolution and photoreduction of CO_2 into hydrocarbon fuels (e.g. CH_4).

To date, several studies have confirmed that anatase TiO_2 single crystals with dominant {100} facets were experimentally prepared in the morphology of rods or cuboids.[7,12,15] Nevertheless, there are still some problems for those reported TiO_2 cuboids, which limited their practical application. For those TiO_2 particles, besides {100} facet, other facet (such as {001} and {101} facets) on the upper and bottom of the cuboids will be also exposed (Figure 4.1). Up to now, the highest percentage of the {100} facet exposed on TiO_2 cuboids is reported to be 85.7%, and the TiO_2 cuboids exhibited a relatively small surface area of 5.8 m^2/g.[15] As we all know, surface area plays an important role in the photocatalytic reaction, which is not only beneficial for the adsorption of the reactant, but also can offer more active sites for the photoreaction.[16,17] Therefore, in order to largely enhance the photocatalytic activity, both the percentage of the exposed {100} facets and surface area should be increased for the anatase TiO_2.

As shown in Figure 4.1, we hypothesize that if we reduce the thickness of the TiO_2 cuboids in the [100] direction to some extent, ultrathin TiO_2 nanosheets will be obtained. In this case, the percentages of the {101} and {001} facets will be significantly decreased, resulting into a larger percentage of {100} facets exposed. Accordingly, in this chapter, we adopt a facile and effective method to fabricate the ultrathin anatase TiO_2 nanosheets with both high percentage of {100} facet exposed (up to 95%) and large surface area (57.1 m^2/g).

To the best of our knowledge, both the percentage of the {100} facet exposed and the surface area of our prepared TiO_2 nanosheets reported in this work is the highest so far. Due to the high ratio of {100} facet exposed as well as the larger surface area, which can offer more active sites in the phtocatalytic reaction, our developed TiO_2 nanosheets showed marked photocatalytic activity, about 5 times higher activity in both of H_2 evolution and CO_2 photoreduction than the reference sample, TiO_2 cuboids with 53% of exposed {100} facet. Moreover, the superior electronic band structure that is resulted from the higher percentage of exposed {100} facet on the TiO_2 nanosheets also makes a great contribution to the higher photocatalytic activity.

4.2 Experimental Section

4.2.1 Synthesis of TiO_2 Nanosheets

All chemicals were of analytical grade and used as received without further purification. In a typical synthesis of the TiO_2 nanosheets, 1 mmol of TiF_4 was firstly dissolved into 2 ml of ethanol. Then, 30 mL of benzyl alcohol containing 3 mmol of oleic acid was added in the above solution. After treated at 200 ^oC for 40 min, the final TiO_2 powders can be obtained. In order to remove the surface absorbed organics and fluorine, the TiO_2 powders were calcined at 600 ^oC for 2 h. The final obtained TiO_2 nanosheets with clean surface are denoted as T_{Sheets}.

4.2.2 Synthesis of TiO_2 Cuboids

TiO_2 cuboids with less {100} facet exposed were also prepared in comparison to the 95% of {100} facets exposed TiO_2 nanosheets. The TiO_2 cuboids were synthesized following the method reported by Pan et al. via reacting 32 mg of $TiOSO_4$ into 40 mL

of HF solution (40 mM) at 180 ^{o}C for 2 h, then calcined at 600 ^{o}C for 2 h to remove the surface fluorine.[7] The obtained TiO_2 cuboids with clean surface are denoted as $T_{Cuboids}$.

4.2.3 Characterization

X-ray diffraction patterns were recorded on a Rigaku Multiflex diffractometer (RINT 2000; Rigaku Corp. Japan) with monochromatized Cu Ka radiation (λ=1.54178 Å). The size and morphology of the samples were observed by a scanning electron microscope (SEM, JSM-6701F, JEOL Co., Japan) and transmission electron microscope (TEM, JEM-200 CX, JEOL) operating at 200 kV. The Brunauer-Emmett-Teller (BET) surface areas were deducted by a surface area analyser (BEL Sorp- II mini, BEL Japan Co., Japan) with nitrogen absorption at 77 K. Raman measurement was carried out using a Raman spectroscopy (NRS-1000; Jasco Corp. Japan). UV-visible absorption spectra were measured on a UV-visible spectrophotometer (UV-2500 PC, Shimadzu Co., Japan). X-ray Photoelectron Spectroscopy (XPS) were conducted on Thermo ESCALAB250 using monochromatized Al Ka at hυ = 1486.6 eV. The binding energies were calibrated to the C1s peak by 284.6 eV. The Electron Paramagnetic Resonance (EPR) spectra were measured to confirm the presence of oxygen vacancy on JEOL JES-FA200 Electron Spin Resonance Spectrometer at ambient temperature. The CO_2 pulse chemisorption tests were carried out on Micromeritics Autochem Ⅱ Chemisorption Analyzer at 35 ^{o}C with a fixed volume loop of 0.05 mL.

4.2.4 Photocatalytic H_2 Evolution Test

The photocatalytic reactions of H_2 evolution were carried out in a closed gas circulation system with an external-irradiation type of a glass reactor. The light source was a 300 W xenon lamp. The intensity of the light at 300-800 nm was measured to be

240 mW/cm^2 by using a spectroradiometer (USR-40; Ushio Inc., Japan). The co-catalyst Pt was loaded by an in-situ photodeposition method. The 1 wt% of Pt-loaded catalyst (60 mg) was dispersed with a magnetic stirrer in a methanol aqueous solution (50 mL of CH_3OH and 220 mL of H_2O). The evolved gas including H_2 was analyzed using an online gas chromatograph (GC-8A; Shimadzu) equipped with a thermal conductivity detector (TCD).

4.2.5 CO_2 Photoreduction

In the photocatalytic reduction of CO_2, 40 mg of the sample without any cocatalyst was uniformly dispersed on a glass reactor with a base area of 8.1 cm^2. A 300 W Xenon arc lamp was used the light source for the photocatalytic reaction. The volume of the reaction system was around 390 mL. The reaction setup was vacuum treated several times, and then high-purity CO_2 gas was introduced into the reaction system to achieve a pressure of 80 kPa. Deionized water (3 mL) was injected into the reaction system. During the irradiation, about 0.5 mL of gas was taken from the reaction cell at given intervals for subsequent CH_4 concentration analysis using a gas chromatograph (GC-14B, Shimadzu) equipped with a flame ionized detector (FID) and methanizer.

4.3 Results and Discussions

4.3.1 Crystal Structure and Morphology

The powder XRD patterns of the prepared TiO_2 nanosheets and cuboids are shown in Figure 4.2. The XRD profiles of the two TiO_2 samples can coincidently be indexed to the pure anatase TiO_2 with tetragonal structure (space group $I4_1/amd$, $a = b = 3.782$ Å, $c = 9.502$ Å, JCPDS Card 73-1764). The peaks at 25.25, 37.72, 48.03, 53.91, and 54.99° can be assigned to (101), (004), (200), (105), and (211) crystal planes of anatase TiO_2,

respectively. The values of the full width at half maximum (FWHM) at 25.25, 37.72, and 48.03° (indexed to be (101), (004), and (200) crystal planes, respectively) are measured to be (0.11, 0.26, and 0.09) for $T_{Cuboids}$ and (0.32, 0.68, and 0.23) for T_{Sheets}, respectively. It is obvious that $T_{Cuboids}$ exhibit better crystallinity than that of T_{Sheets}. Moreover, according to the JCPDS standard card, the peak intensity of $I_{(101)}$:$I_{(004)}$:$I_{(200)}$ equals to 100:18:23; it is noteworthy that the relative peak intensities of the (101), (004), and (200) planes are calculated to be 100:23:48 and 100:20:53 for $T_{Cuboids}$ and T_{Sheets}, respectively, indicating that both $T_{Cuboids}$ and T_{Sheets} have the preferential crystallographic orientation along the [100] direction.

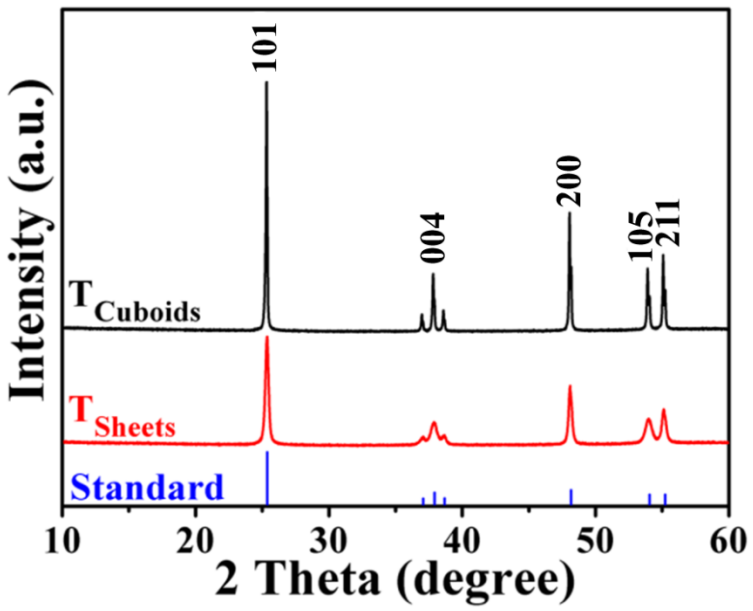

Figure 4.2 XRD patterns of TiO_2 nanosheets and cuboids.

The morphology of the TiO_2 nanosheets was observed by SEM. As shown in Figure 4.3a, the TiO_2 sample consists of large amounts of paper-like nanosheets. These nanosheets assemble together to form the hierarchical architectures. In order to observe the nanosheets clearly, the TEM image is shown in Figure 4.3b. Those sheets are in the

size around 70 nm × 70 nm with the thickness around 2 nm. The high-resolution TEM (HRTEM) image (Figure 2c) shows that the distance of the visible lattice fringes were measured to be 0.35 and 0.48 nm, which is corresponding to the lattice spacing of the (011) and (002) atomic plane of anatase TiO_2, respectively.[18] Furthermore, the selected-area electron diffraction (SAED) pattern (inset of Figure 4.3c) can be indexed to the diffraction spots of the [100] zone for the TiO_2 single crystalline, indicating that our prepared T_{Sheets} are exposed with {100} facet. This result is well-coincident with the analysis of the XRD pattern, which implies that the T_{Sheets} preferential crystallographic grow along the [100] direction. Anatase TiO_2 is in the tetragonal structure and belonging to the space group of $I4_1/amd$, in which $a = b = 3.782$ Å, $c = 9.502$ Å, thus {100} facet is equal to {010} facet in anatase TiO_2. (In some literatures, it is reported to be {010} facet.) In addition, the low-magnification SEM image (Figure 4.4) proved that our prepared TiO_2 sample is composed of almost all the nanosheets. Hence, based on the above information, we can calculate that the percentage of the exposed {100} facet in T_{Sheets} is about 95%. The morphology of the TiO_2 cuboids can be observed as shown in Figure 4.3d. The cuboids are in the size of 0.6 μm ×1.5 μm with a thickness about 300 nm. The percentage of the exposed {100} facet in $T_{Cuboids}$ was reported to be 53%.[7] In addition, with the decrease of the thickness from 300 nm (cuboids) to 2 nm (nanosheets), the surface areas are largely increased from 3.9 m^2/g for $T_{Cuboids}$ to 57.1 m^2/g for T_{Sheets} (Figure 4.5). Both the higher percentage of {100} facet and larger surface area of our developed T_{Sheets} can offer more active sites in the photocatalytic reaction, which are beneficial for the photocatalytic performance.

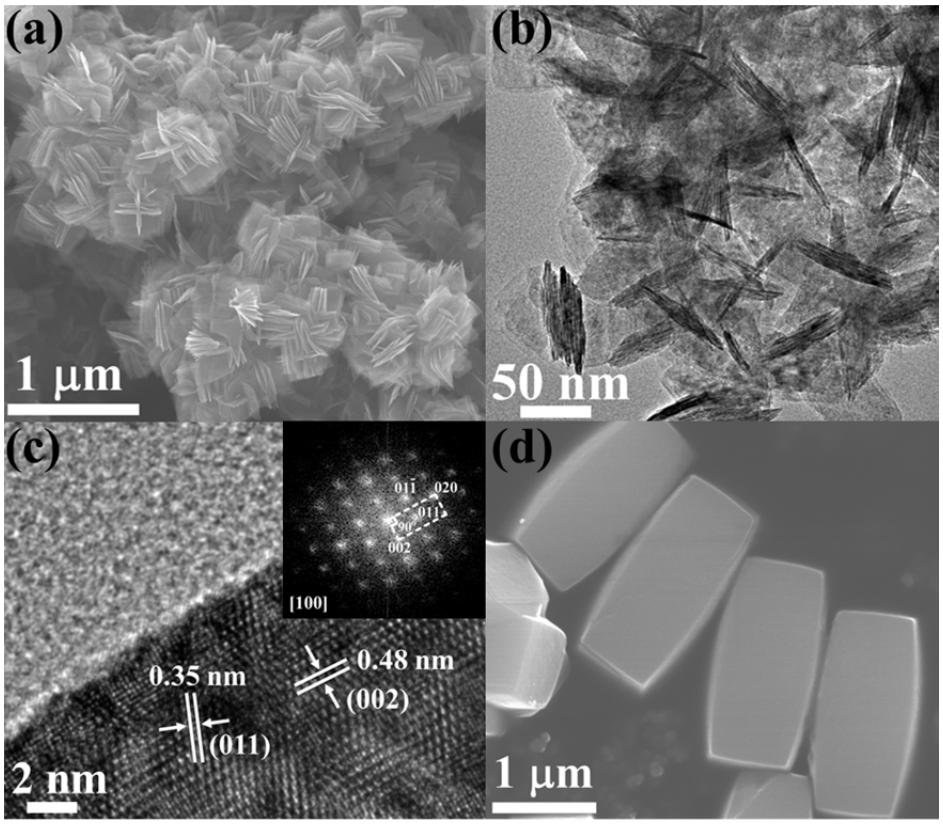

Figure 4.3 SEM image (a), TEM image (b), HRTEM image (c), and SAED pattern (inset of c) of the TiO_2 nanosheets, as well as the SEM image of the TiO_2 cuboids (d).

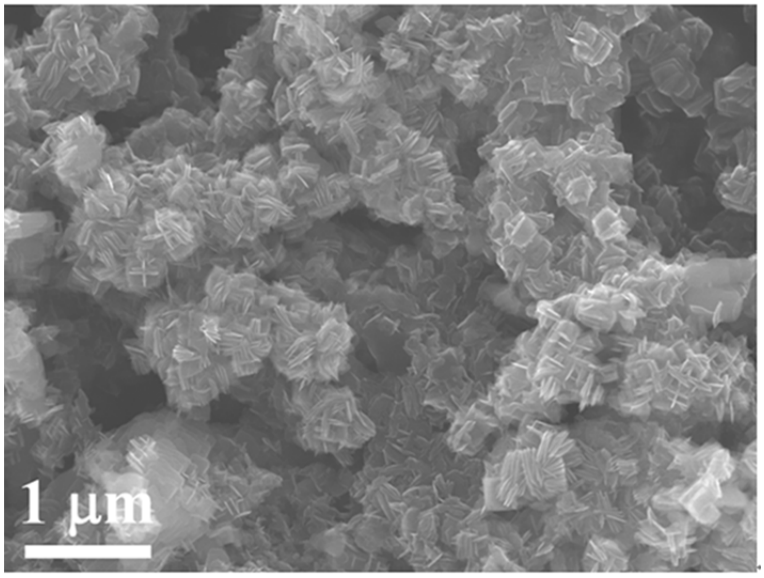

Figure 4.4 Low-magnification SEM image of the prepared TiO_2 nanosheets.

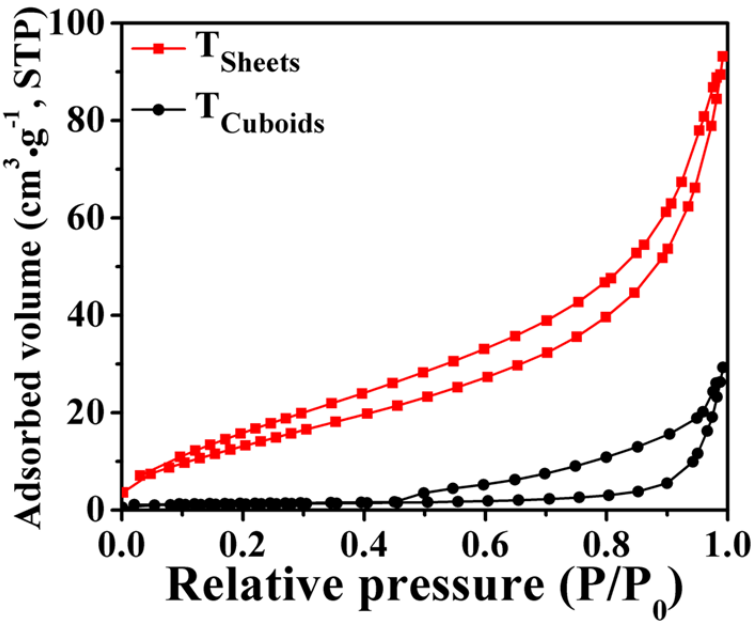

Figure 4.5 Nitrogen adsorption-desorption isotherms of the TiO_2 nanosheets and cuboids.

Meanwhile, the crystal structures of the two TiO_2 samples were also investigated by Raman spectroscopy. As shown in Figure 4.6, the peaks appeared at 396, 515, and 638 cm^{-1} of the two TiO_2 samples are corresponding to the B_{1g}, A_{1g}, and E_g peaks of anatase TiO_2, respectively.[19] However, the relative intensities of the three peaks in the two TiO_2 samples are obviously different, in which the intensities of the A_{1g} and B_{1g} peaks of T_{Sheets} are obviously much higher than that of $T_{Cuboids}$. For anatase TiO_2, the E_g, B_{1g}, and A_{1g} peaks are mainly related to the symmetric stretching vibration, symmetric bending vibration, and antisymmetric bending vibration of the O-Ti-O, respectively.[19] The slab models of the {100} and {101} surfaces are shown in Figure 4.7. It can be observed that the {101} surface is flatter than {100} surface and 100% Ti atoms on the top layer of the {100} surface are 5-coordinated, thus it can be deduced that more O-Ti-O bonding on the {100} surface are bending vibration because of its unique atomic arrangement.[19]

For $T_{Cuboids}$, it was composed of 53% {100}, 33% {101}, and 14% {001} facets.[7] In comparison to T_{Sheets} with up to 95% {100} facet, the bending vibration of the O-Ti-O will be much stronger on the T_{Sheets}. Therefore, the relative peaks in 396 and 515 cm^{-1} for T_{Sheets} are much higher than that of $T_{Cuboids}$.

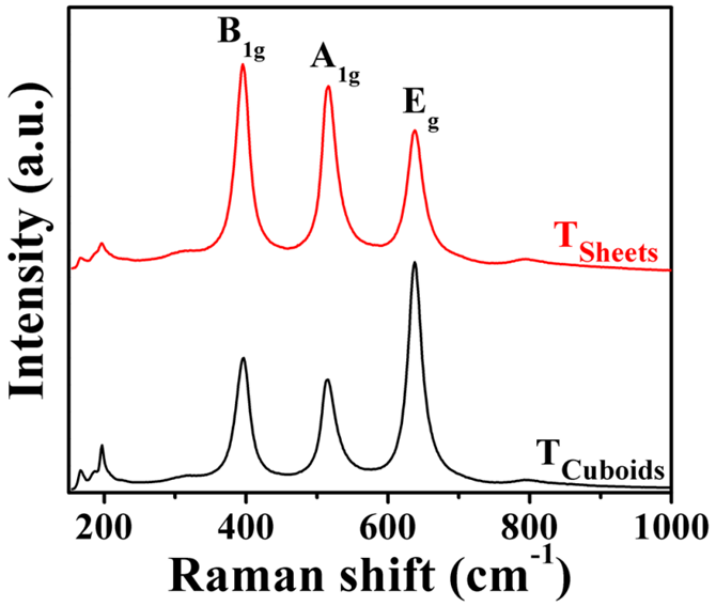

Figure 4.6 Raman spectra of the TiO_2 nanosheets and cuboids exposed with different percentage of {100} facets.

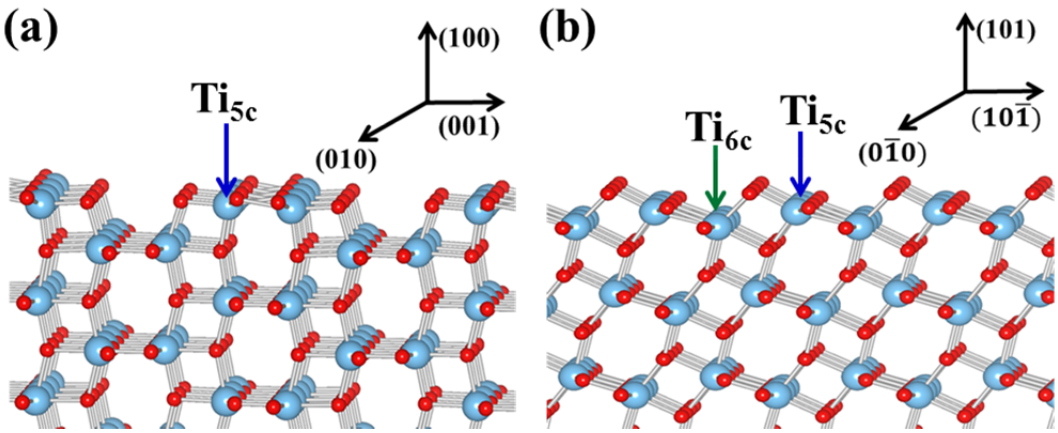

Figure 4.7 Slab models of {100} surface (a) and {101} surface (b) of anatase TiO_2. (Ti_{5c}: 5-coordinated Ti atoms; Ti_{6c}: fully- or 6-coordinated Ti atoms)

4.3.2 Electronic Structure

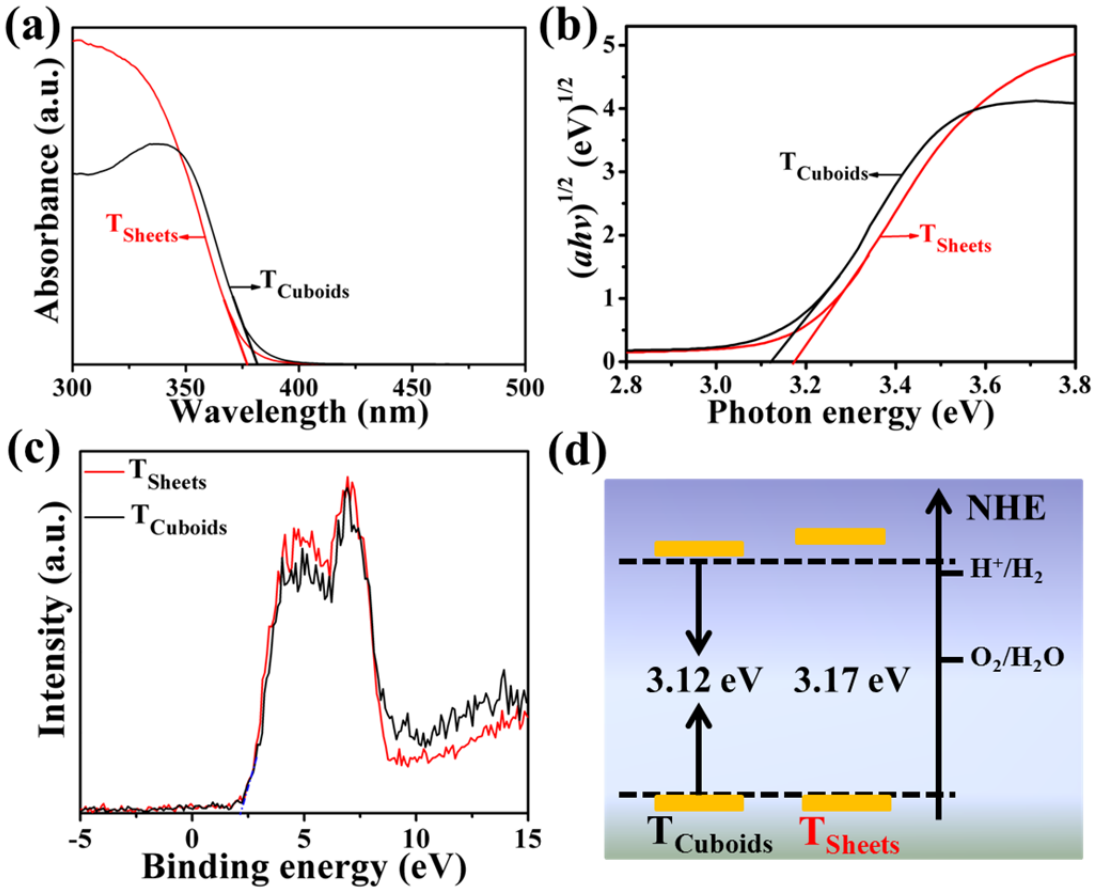

Figure 4.8 UV-visible absorption spectra (a), the corresponding plots of transformed Kubelka-Munk function versus the energy of photon (b), Valence band XPS spectra (c) of the TiO_2 nanosheets and cuboids exposed with different percentage of {100} facets, and schematic illustration of the band structures of the two TiO_2 samples (d).

The UV visible absorption spectra of the TiO_2 nanosheets and cuboids are shown in Figure 4.8a. Compared with the $T_{Cuboids}$ exposed with 53% {100} facet, the intrinsic absorption edge of our prepared T_{Sheets} with 95% {100} facets has an obvious blue-shift by 5 nm. Based on the formula $a=B_i(hv-E_g)^2/hv$ (a is the absorption coefficient, hv is the incident photon energy, and B_i is the absorption constant for indirect transitions),[20] the

band gaps are deduced to be 3.12 and 3.17 eV for the $T_{Cuboids}$ and T_{Sheets}, respectively (Figure 4.8b). The valence band maximum of the two TiO_2 samples are measured to be similar (Figure 4.8c), thus the larger band gap of the T_{Sheets} is indicated to a higher conduction band minimum of the T_{Sheets} in contrast to the $T_{Cuboids}$ (Figure 4.8d).

Our experimental phenomenon is in well-accordance with the previous report. It is well accepted that {100} facet owns superior electronic structure in comparison with other facets (e.g. {001} facet and {101} facet), and TiO_2 single crystals exposed with more {100} facets will exhibit higher conduction band minimum.[6,7,12,21] In this work, when the percentage of the {100} facet is increased from 53% to 95%, the conduction band minimum of the T_{Sheets} obviously increases. The higher conduction band minimum, on which more reductive electrons can be generated and then transferred to the TiO_2 surface to take part in the photocatalytic reaction, is beneficial for the photocatalytic reaction.[6,22]

4.3.3 Photocatalytic H_2 Evolution

As a photocatalyst, anatase TiO_2 has a conduction band edge that is more negative [vs. normal hydrogen electrode (NHE)] than the H^+/H_2 reduction potential; thus, the TiO_2 can efficiently split water into hydrogen, which is a promising candidate as a future energy carrier.[23] So, herein, the H_2 evolution tests in the presence of methanol as hole scavenger were carried out to evaluate the photocatalytic activity of the prepared T_{Sheets} and $T_{Cuboids}$. As shown in Figure 4.9a, when the TiO_2 is excited by the light, the photo-generated electrons will move to the conduction band, left a positive hole in the valence band. In the H_2 evolution, the electrons will then transfer to the TiO_2 surface on the Pt sites to reduce H^+ into H_2; the holes will be exhausted via oxidizing the sacrifice

reagent (methanol) to prevent the hole-electron recombination.[1] As shown in Figure 4.10, the H_2 evolution rates over 6 hours are measured to be 362 μmol•h^{-1} and 79 μmol•h^{-1} for the T_{Sheets} and $T_{Cuboids}$, respectively; the photocatalytic activity of T_{Sheets} is 4.6 times higher of $T_{Cuboids}$.

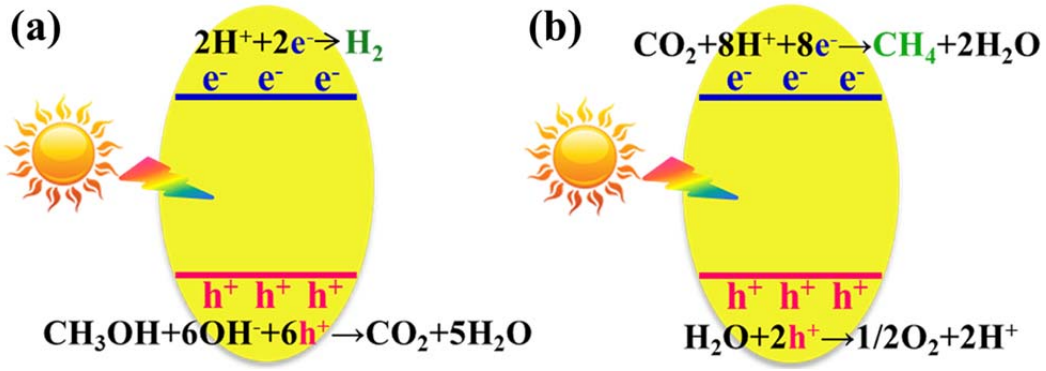

Figure 4.9 Schematic illustration of H_2 evolution (a) and CO_2 photoreduction (b) processes.

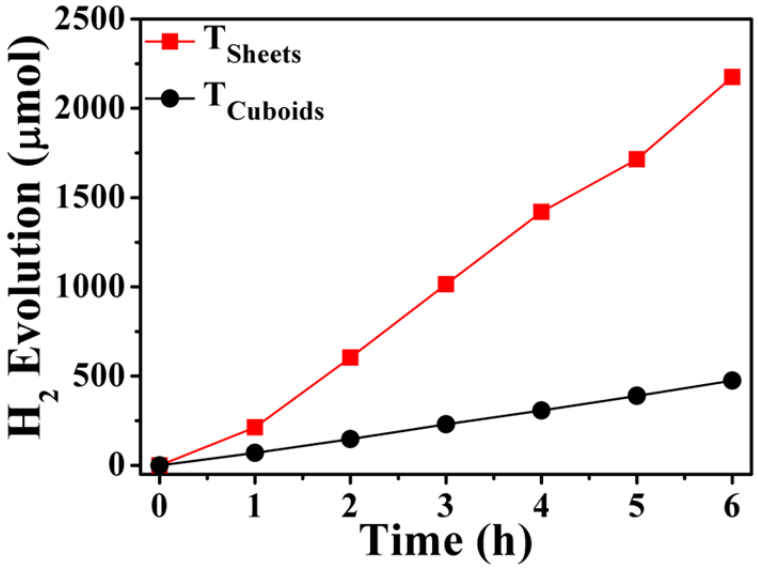

Figure 4.10 Photocatalytic H_2 evolution tests of the 1 wt% Pt-loaded TiO_2 samples with the same mass of 60 mg under UV-visible light irradiation (λ > 300 nm).

4.3.4 Investigation of the Enhanced Photocatalytic Activity

In general, the photocatalytic activity is affected by various factors, such as optical absorption properties, crystallinity, surface area, facet reactivity, and defect contents, and so on.[1,24,25] Herein, the effect of several factors on the photocatalytic activity are discussed as below.

First, considering about the optical absorption properties; more photons absorbed by the TiO_2 photocatalyst, more photoexcited charge carriers can be produced to take part in the photocatalytic reaction.[26] As shown in Figure 4.8a, $T_{Cuboids}$ exhibit red-shifted optical absorption edge in comparison to T_{Sheets}, while the intensity of the absorption of T_{Sheets} is higher than $T_{Cuboids}$ in the region of 300-350 nm. Hence, their photocatalytic performance under monochromatic light centered at a wavelength of 361 nm was studied. In this case, $T_{Cuboids}$ obviously absorb more light than T_{Sheets} (Figure 4.11a); however, the activity of T_{Sheets} is 3.3 times higher of $T_{Cuboids}$ as shown in Figure 4.11b. Next, discuss the effect of crystallinity; obviously, $T_{Cuboids}$ have a better crystallinity than T_{Sheets} (Figure 4.2), which is beneficial for the inhabitation of charge recombination in the photocatalytic reaction,[27] but T_{Sheets} still exhibit significantly higher photocatalytic activity than $T_{Cuboids}$. Thus, the effect of both optical absorption properties and crystallinity will not be the reason for the higher activity of T_{Sheets}.

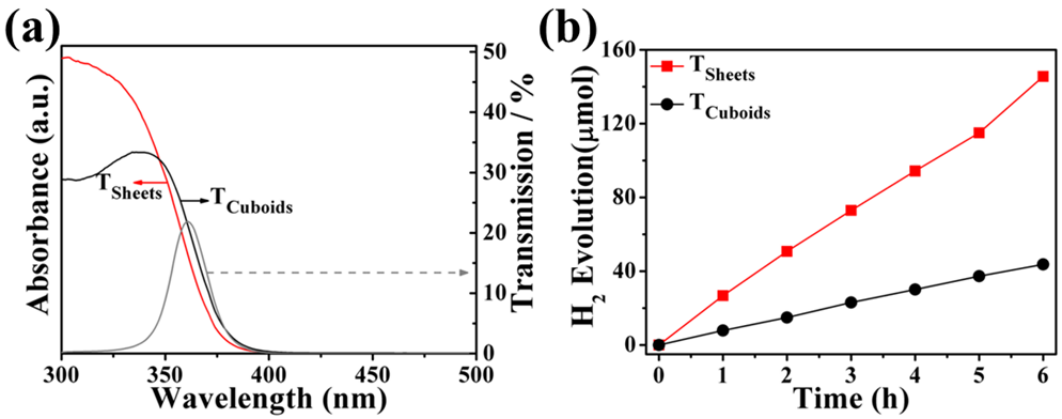

Figure 4.11 (a) UV-visible absorption spectra of the TiO_2 samples, and the power spectrum of the monochromatic filter centered at a wavelength of 361 nm ($\Delta\lambda = \pm$ 19.4 nm) (gray curve). (b) Comparison of photocatalytic activities between T_{Sheets} and $T_{Cuboids}$ under the monochromatic light irradiation (λ = 361 nm, $\Delta\lambda = \pm$19.4 nm).

Then, taking the surface area into account; TiO_2 with a larger surface area can not only offer more active reactions sites on the surface but also is beneficial for the reactant adsorption.[28,29] In comparison to $T_{Cuboids}$ (3.9 m^2/g), T_{Sheets} exhibit a relatively large surface area of 57.1 m^2/g. With a larger surface area of the T_{Sheets}, the surface area of the exposed {100} facet will be also increased, thus more 5-coordinated Ti atoms (Ti_{5c}) will be existed on the surface. Experimentally, we compared the photocatalytic activity of the two TiO_2 samples in the same total surface area as shown in Figure 4.12. In this case, the activity of T_{Sheets} is about 3.5 times of $T_{Cuboids}$; in contrast to the 4.6 times higher activity of T_{Sheets} than $T_{Cuboids}$ with the same mass but different surface area, the above control experiments indicate that the surface area indeed makes contributions to the enhancement of photocatalytic activity, however, some other factors (including facet reactivity, surface defects, and electronic band structures) might be also contributed to the higher photocatalytic activity.

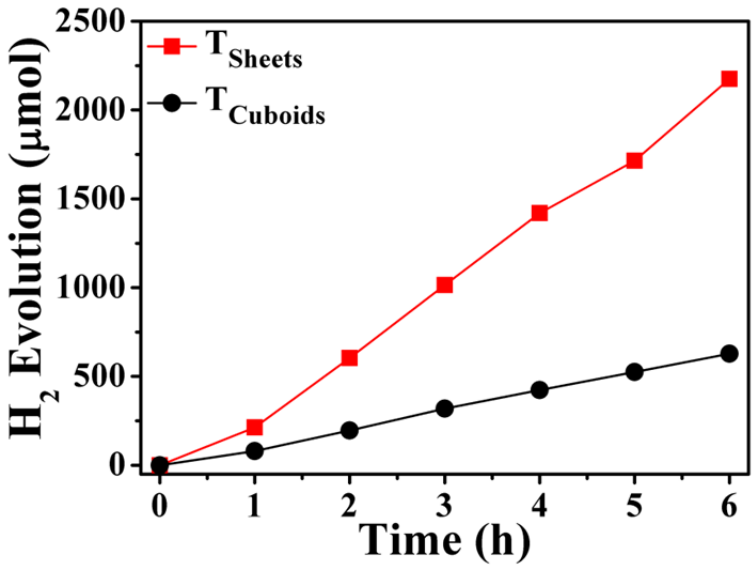

Figure 4.12 Comparison of photocatalytic activities between T_{Sheets} (60 mg × 57.1 m^2/g = 3.43 m^2) and $T_{Cuboids}$ (879 mg × 3.9 m^2/g = 3.43 m^2) with same total surface area (ca. 3.43 m^2) under UV-visible light irradiation (λ > 300 nm).

Surface chemistry (such as facet reactivity and surface defects) always plays important roles in the photocatalysis.[8,25] {100} facet is reported to be the active facet in H_2 evolution because of its superior surface properties.[7] With more {100} facets exposed on T_{Sheets}, more 5-coordinated Ti atoms can be offered on the surface to act as active sites for the photocatalytic reaction. Meanwhile, because of the largely under-coordinated Ti and O atoms existed on the {100} surface (Figure 4.7), our previous theoretical calculation results revealed that the oxygen vacancy is more easily produced on the {100} surface than that of the {101} surface.[30] Herein, more {100} facet is exposed on T_{Sheets} than that of $T_{Cuboids}$ based on the analysis of Raman spectra, thus more oxygen vacancy might be formed on the surface of T_{Sheets}. To check the existence of the oxygen vacancies on the TiO_2 surface, the electron paramagnetic resonance (EPR) spectra were adopted as shown in Figure 4.13. The signal observed at

g = 2.002 for T_{Sheets} is the characteristics of oxygen vacancy existed on the surface of TiO_2.[31] T_{Sheets} shows an EPR signal at g = 2.002 but $T_{Cuboids}$ does not, indicating that some oxygen vacancy is existed on the T_{Sheets} surface. Those oxygen vacancies are known to act as active reaction sites in the photocatalytic reaction.[3,30]

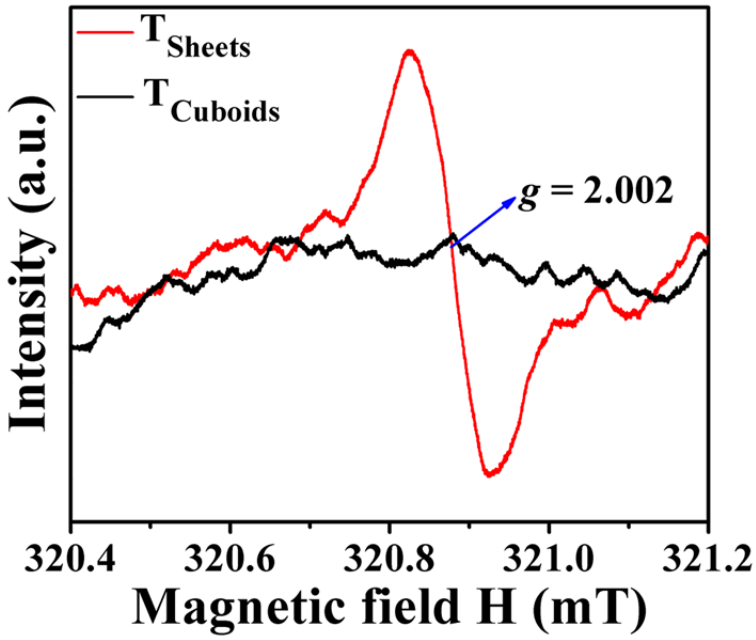

Figure 4.13 Electron Paramagnetic Resonance (EPR) spectra (measured at ambient temperature) of the TiO_2 samples. (According to the formula $g = h\nu/\beta H$, where g is the g value, h is Planck's constant, ν is the microwave frequency, β is the Bohr magneton, and H is the magnetic field at resonance. Herein, when H is equal to 320.877 mT, the g value is obtained as 2.00267.)

In addition, the CO_2 pulse chemisorption results showed that T_{Sheets} can adsorb 0.15 mL/g CO_2 but the CO_2 adsorption property of $T_{Cuboids}$ is very weak (Figure 4.14 and Table 4.1). The CO_2 chemisorption over T_{Sheets} is resulted from its surface oxygen vacancy,[32,33] which is further confirmed that oxygen vacancies are produced on the surface of T_{Sheets}. Finally, besides its superior surface atomic structure, {100} facet also

exhibits excellent surface electronic structure. Herein, with more {100} facet exposed in our developed T_{Sheets}, the electronic band gap of T_{Sheets} is increased. As shown in Figure 4.8d, the conduction band minimum of T_{Sheets} is much higher than that of $T_{Cuboids}$, the superior electronic band structure of the T_{Sheets} will make a great contribution to the enhanced photocatalytic activity, in which more strongly reductive electrons can be produced then transferred to the surface to reduce H^+ into H_2.[6,7,21]

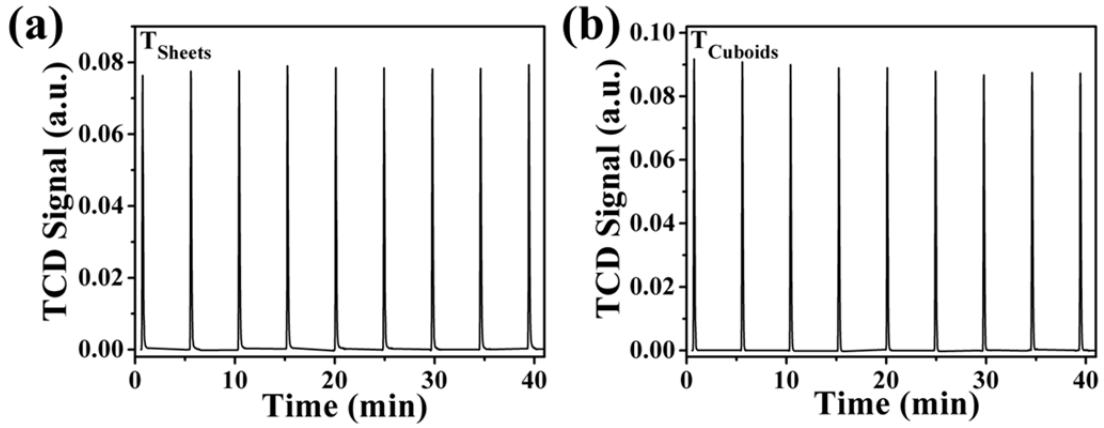

Figure 4.14 CO_2 pulse chemisorption tests over TiO_2 nanosheets (a) and cuboids (b). (TCD: thermal conductivity detector.)

Table 4.1 Peak areas and calculated adsorption amounts of CO_2 in CO_2 pulse chemisorption measurements.

	peak areas (a.u.)									CO_2 adsorption (ml/g)
	1	2	3	4	5	6	7	8	9	
T_{Sheets}	0.0097	0.0103	0.0102	0.0101	0.0102	0.0101	0.0101	0.0102	0.0102	**0.15**
$T_{Cuboids}$	0.0115	0.0113	0.0112	0.0111	0.0111	0.0110	0.0110	0.0111	0.0111	**< 0.001**

On the basis of the above analysis, we can conclude that the higher percentage of the exposed {100} facet (up to 95%) and the larger surface area (57.1 m^2/g) make more

{100} facet exposed on the T_{Sheets} surface; accordingly, oxygen vacancies together with more Ti_{5c} atoms are existed on the surface to act as active reaction sites, and the superior electronic band structure is also beneficial for the photocatalytic reaction, followed with a higher photocatalytic activity of T_{Sheets}.

4.3.5 Investigation about the Surface Reconstruction

In the synthesis process of the TiO_2 nanosheets, fluorine species is used to stabilize the {100} facets by forming the Ti-F bonds; however, the surface Ti-F bonds will lead to the surface reconstruction in two aspects: changing 5-coordinated Ti atoms (Ti_{5c}) into fully- or 6-coordinated Ti atoms (Ti_{6c}) and modification of the force constants of the surface Ti-O-Ti network. Those changes can be indicated by the Raman spectra. As shown in Figure 4.15, in comparison to the TiO_2 nanosheets with clean surface (b), the peak related to the E_g mode of TiO_2 with Ti-F bond on its surface before calcination (a) shifted towards lower frequency. The surface reconstruction caused by the Ti-F bonding will largely destroy the surface activity of the {100} facet.

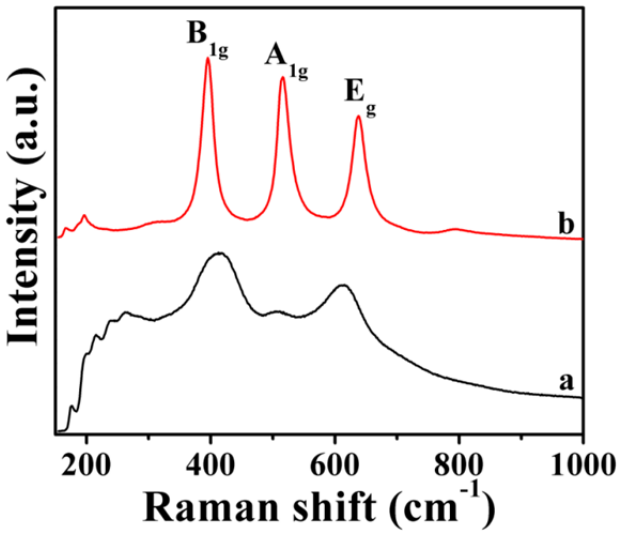

Figure 4.15 Raman spectra of TiO_2 nanosheets before (a) and after calcination (b).

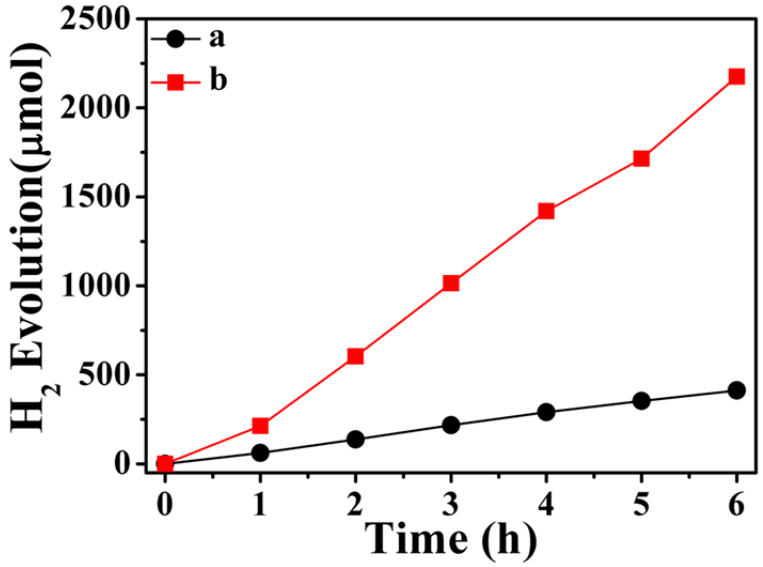

Figure 4.16 Photocatalytic activity of TiO_2 nanosheets before (a) and after calcination (b) under UV-visible light irradiation ($\lambda > 300$ nm).

As shown in Figure 4.16, the photocatalytic activity of the TiO_2 nanosheets before and after calcination at 600 ^oC are obviously different; the TiO_2 with clean surface (b) exhibits 5.3 times higher activity of the TiO_2 contained with Ti-F bonds (a). Therefore, our prepared TiO_2 nanosheets should be calcined at 600 ^oC for 2 h to remove the surface fluorine and recover the surface structure of {100} facet before the photocatalytic tests.

Moreover, the possible influence of the surface reconstruction during the photocatalytic reaction process is also investigated. Herein, we carried out a study related to the photocatalytic stability of our developed T_{Sheets} with clean surface. As shown in Figure 4.17, T_{Sheets} exhibits excellent photocatalytic stability in the time course tests, indicating that the effect of surface reconstruction on the clean {100} surface during the photocatalytic reaction can be ignored in our study.

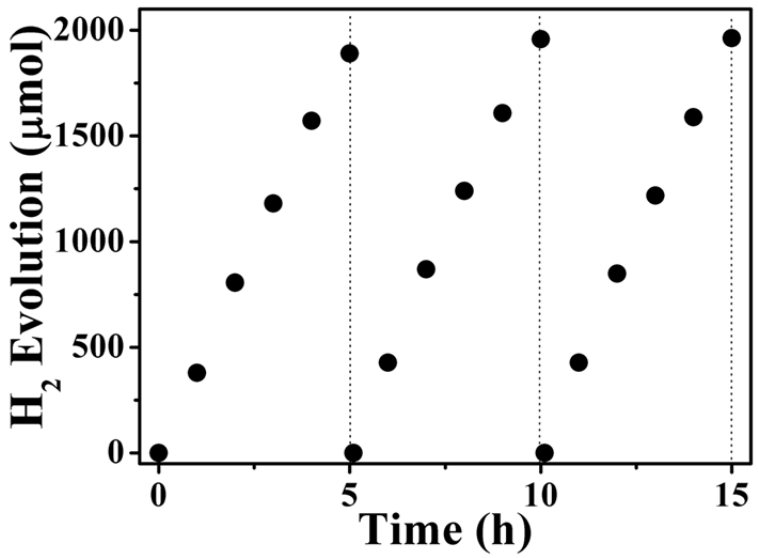

Figure 4.17 Time course of evolved H_2 over T_{Sheets} with clean surface under UV-visible light irradiation ($\lambda > 300$ nm).

4.3.6 CO_2 Photoreduction

Furthermore, the photocatalytic CO_2 reduction into hydrocarbon fuels is another promising application for TiO_2 photocatalyst.[22] The direct reduction of CO_2 into hydrocarbon fuels (e.g. CH_4) using solar energy is one of the best strategies to manage both the global warming and the energy shortage.[34-37] In the CO_2 photoreduction process, as shown in Figure 4.9b, the photo-generated holes in the valence band oxidize water into hydrogen ions (H^+) via the half-reaction $H_2O + 2h^+ \rightarrow 1/2O_2 + 2H^+$, and the photo-generated electrons in the conduction band reduce CO_2 to CH_4 via the reaction of $CO_2 + 8H^+ + 8e^- \rightarrow CH_4 + 2H_2O$.[38] Here, the photocatalytic activity of the TiO_2 nanosheets and cuboids in CO_2 photoreduction were evaluated over 40 mg of photocatalyst without any cocatalyst in a gas-solid system as shown in Figure 4.18a. Besides CH_4 as the main product, trace amounts of CO can also be detected. The CH_4 evolution rates over T_{Sheets} and $T_{Cuboids}$ are determined to be 5.8 and 1.2 $ppm \bullet g^{-1} \bullet h^{-1}$,

respectively; in which T_{Sheets} is 4.8 times higher of $T_{Cuboids}$. The photoreactivity order is the same as that of the H_2 evolution test, $T_{Sheets} > T_{Cuboids}$. When compare the photocatalytic activity of the two TiO_2 samples in the same total surface area, as shown in Figure 4.18b, T_{Sheets} still exhibits higher photocatalytic activity, about 2.8 times of $T_{Cuboids}$. Herein, the reason of the higher activity of T_{Sheets} in CO_2 photoreduction is similar to that in H_2 evolution.

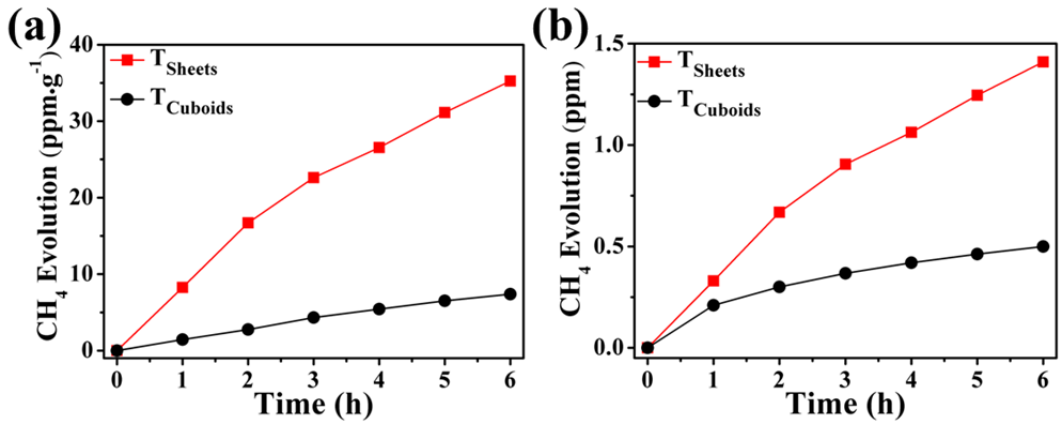

Figure 4.18 (a) Photocatalytic CO_2 photoreduction tests of the TiO_2 samples without any cocatalyst under UV-visible light irradiation (λ > 300 nm). (b) Comparison of photocatalytic activities between T_{Sheets} (40 mg × 57.1 m^2/g = 2.28 m^2) and $T_{Cuboids}$ (585 mg × 3.9 m^2/g = 2.28 m^2) with same total surface area (ca. 3.43 m^2) under UV-visible light irradiation (λ > 300 nm).

Firstly, both the oxygen vacancy existed on the TiO_2 surface and the larger surface area of TiO_2 nanosheets is beneficial for the CO_2 adsorption. Then, the photoexcited electrons on the conduction band of TiO_2 transfer to the TiO_2 surface to reduce CO_2 into CH_4. During this reaction process, since more {100} facet is exposed on the surface of T_{Sheets}, more surface active sites (such as Ti_{5c} atoms) will be offered. On the other hand, T_{Sheets} exhibits a higher conduction band minimum (Figure 4.8d), on which more

reductive electrons can be generated; more reductive potential of the electrons, the higher CH_4 output efficiency. Thus, the higher photocatalytic activity of T_{Sheets} is ascribed to its larger surface area, more active sites (e.g. oxygen vacancy and Ti_{5c} atoms) existed on the surface, and the superior electronic band structure. Moreover, controlled experiments show that no CH_4 was evolved when the photocatalytic reaction was carried out in the dark or irradiated in the absence of photocatalyst, revealing that the reduction of CO_2 is driven by light irradiation over the photocatalyst.

4.4 Conclusion

Ultrathin anatase TiO_2 nanosheets exposed with 95% of {100} facets are prepared. In contrast to the reference sample, TiO_2 cuboids exposed with 53% of {100} facets, our developed TiO_2 nanosheets own a relatively higher percentage of exposed {100} facet, larger surface area, and superior electronic band structure, which make the TiO_2 nanosheets exhibit significantly higher photocatalytic activity in both of H_2 evolution and CO_2 photoreduction processes. This study is related to the fine-tuning of the TiO_2 photocatalyst exposed with high percentage of active facets for excellent photocatalytic performance in the potential application of renewable energy. Furthermore, the present work also motivates us to process the facet engineering of other functional materials to achieve advanced and excellent properties over photocatalysts.

Reference:

(1) Tong, H.; Ouyang, S. X.; Bi, Y. P.; Umezawa, N.; Oshikiri, M.; Ye, J. H. *Adv. Mater.* **2012**, *24*, 229.

(2) Tang, J. W.; Zou, Z. G.; Ye, J. H. *Angew. Chem. Int. Ed.* **2004**, *43*, 4463.

(3) Bi, Y. P.; S.X., O.; Umezawa, N.; Cao, J. Y.; Ye, J. H. *J. Am. Chem. Soc.* **2011**,

133, 6490.

(4) Jiang, J.; Zhao, K.; Xiao, X. Y.; Zhang, L. Z. *J. Am. Chem. Soc.* **2012**, *134*, 4473.

(5) Wang, X. N.; Huang, B. B.; Wang, Z. Y.; Qin, X. Y.; Zhang, X. Y.; Dai, Y.; Whangbo, M. H. *Chem. Eur. J.* **2010**, *16*, 7106.

(6) Liu, G.; Yu, J. C.; Lu, G. Q.; Cheng, H. M. *Chem. Commun.* **2011**, *47*, 6763.

(7) Pan, J.; Liu, G.; Lu, G. M.; Cheng, H. M. *Angew. Chem. Int. Ed.* **2011**, *50*, 2133.

(8) Yang, H. G.; Sun, C. H.; Qiao, S. Z.; Zou, J.; Liu, G.; Smith, S. C.; Cheng, H. M.; Lu, G. Q. *Nature* **2008**, *453*, 638.

(9) Barnard, A. S.; Curtiss, L. A. *Nano Lett.* **2005**, *5*, 1261.

(10) Barnard, A. S.; Zapol, P.; Curtiss, L. A. *J. Chem. Theory Comput.* **2005**, *1*, 107.

(11) Anatase TiO_2 is in the tetragonal structure and belonging to the space group of $I4_1/amd$, in which $a = b = 3.782$ Å, $c = 9.502$ Å, thus {100} facet is equal to {010} facet in anatase TiO_2.

(12) Pan, J.; Wu, X.; Wang, L. Z.; Liu, G.; Lub, G. Q.; Cheng, H. M. *Chem. Commun.* **2011**, *47*, 8361.

(13) Lazzeri, M.; Vittadini, A.; Selloni, A. *Phys. Rev. B: Condens. Matter* **2001**, *63*, 155409.

(14) Lazzeri, M.; Vittadini, A.; Selloni, A. *Phys. Rev. B: Condens. Matter* **2002**, *65*, 119901.

(15) Zhao, X. W.; Jin, W. Z.; Cai, J. G.; Ye, J. F.; Li, Z. H.; Ma, Y. R.; Xie, J. L.; Qi, L. M. *Adv. Funct. Mater.* **2011**, *21*, 3554.

(16) Chen, X. Q.; Li, Z. S.; Ye, J. H.; Zou, Z. G. *Chem. Mater.* **2010**, *22*, 3583.

(17) Xu, H.; Zhang, L. Z. *J. Phys. Chem. C* **2010**, *114*, 940.

(18) Li, J.; Xu, D. *Chem. Commun.* **2010**, 46, 2301.

(19) Tian, F.; Zhang, Y. P.; Zhang, J.; Pan, C. X. *J. Phys. Chem. C* **2012**, *116*, 7515.

(20) Butler, M. A. *J. Appl. Phys.* **1977**, *48*, 1914.

(21) Liu, G.; Sun, C. H.; Yang, H. G.; Smith, S. C.; Wang, L. Z.; Lu, G. Q.; Cheng, H. M. *Chem. Commun.* **2010**, *46*, 755.

(22) Inoue, T.; Fujishima, A.; Konishi, S.; Honda, K. *Nature* **1979**, *277*, 637.

(23) Fujishima, A.; Honda, K. *Nature* **1972**, *238*, 37.

(24) Hoffmann, M. R.; Martin, S. T.; Choi, W. Y.; Bahnemann, D. W. *Chem. Rev.* **1995**, *95*, 69.

(25) Linsebigler, A. L.; Lu, G. Q.; Yates, J. T. *Chem. Rev.* **1995**, *95*, 735.

(26) Xu, H.; Chen, X. Q.; Ouyang, S. X.; Kako, T.; Ye, J. H. *J. Phys. Chem. C* **2012**, *116*, 3833.

(27) Ouyang, S. X.; Ye, J. H. *J. Am. Chem. Soc* **2011**, *133*, 7757.

(28) Li, Y. Z.; Sun, Q.; Kong, M.; Shi, W. Q.; Huang, J. C.; Tang, J. W.; Zhao, X. J. *J. Phys. Chem. C* **2011**, *115*, 14050.

(29) Fan, X. X.; Wang, Y.; Chen, X. Y.; Gao, L.; Luo, W. J.; Yuan, Y. P.; Li, Z. S.; Yu, T.; Zhu, J. H.; Zou, Z. G. *Chem. Mater.* **2010**, *22*, 1276.

(30) Xu, H.; Reunchan, P.; Ouyang, S. X.; Tong, H.; Umezawa, N.; Kako, T.; Ye, J. H. *Chem. Mater.* **2013**, *25,* 405.

(31) Anpo, M.; Che, M.; Fubini, B.; Garrone, E.; Giamello, E.; Paganini, M. C. *Top. Catal.* **1999**, *8*, 189.

(32) Thompson, T. L.; Diwald, O.; Yates, J. T. *J. Phys. Chem. B* **2003**, *107*, 11700.

(33) Thompson, T. L.; Yates, J. T. *Top. Catal.* **2005**, *35*, 197.

(34) Cheng, H. F.; Huang, B. B.; Liu, Y. Y.; Wang, Z. Y.; Qin, X. Y.; Zhang, X. Y.; Dai, Y. *Chem. Commun.* **2012**, *48*, 9729.

(35) Li, P.; Ouyang, S. X.; Xi, G. C.; Kako, T.; Ye, J. H. *J. Phys. Chem. C* **2012**, *116*, 7621.

(36) Zhou, Y.; Tian, Z. P.; Zhao, Z. Y.; Liu, Q.; Kou, J. H.; Chen, X. Y.; Gao, J.; Yan, S. C.; Zou, Z. G. *ACS Appl. Mater. Interfaces* **2011**, *3*, 3594.

(37) Chen, X. Y.; Zhou, Y.; Liu, Q.; Li, Z. D.; Liu, J. G.; Zou, Z. G. *ACS Appl. Mater. Interfaces* **2012**, *4*, 3372.

(38) Xi, G. C.; Ouyang, S. X.; Ye, J. H. *Chem. Eur. J.* **2011**, *17*, 9057.

Chapter 5 Anatase TiO_2 Single Crystals Exposed with High-Reactive {111} Facets toward Efficient H_2 Evolution

5.1 Introduction

Photocatalysis is an environmental-friendly and promising technology to convert solar energy into chemical energy.[1-5] Recently, special attention has been paid on the surface chemistry of TiO_2, since many physical and chemical processes happened on the surface during the photocatalytic reaction.[6-8] Peculiarly, for a crystalline TiO_2, the surface geometric (atomic arrangement and coordination) and electronic structures vary with crystal facets in different orientations, leading to various physical and chemical properties.[9]

Among the most investigated crystal facets ({100}, {101}, and {001} facets) for anatase TiO_2, {001} facet was ever been considered to be the active facets in the photocatalysis because of its highest surface energy (0.90 J/m^2) and superior surface atomic structure (100% five-coordinated Ti atoms (Ti_{5c}) on its surface). However, in 2011, Pan et al. reported that {100} facet owns the superior electronic structure than that of {001} and {101} facets, and TiO_2 single crystals exposed with more {100} facets exhibited superior electronic band structure than that of TiO_2 exposed with more {001} facets, thus resulted into a much higher photocatalytic activity in the H_2 evolution.[9] Those above findings indicated that both the surface atomic structure and electronic structure play important roles in the photocatalytic reaction, thus inspire us to make TiO_2 expose new active crystal facet with superior properties in both atomic structure and electronic configuration. We expect that those unique properties can endow TiO_2

with high photocatalytic activity, hence promoting their potential applications in the clean-energy and environmental remediation.

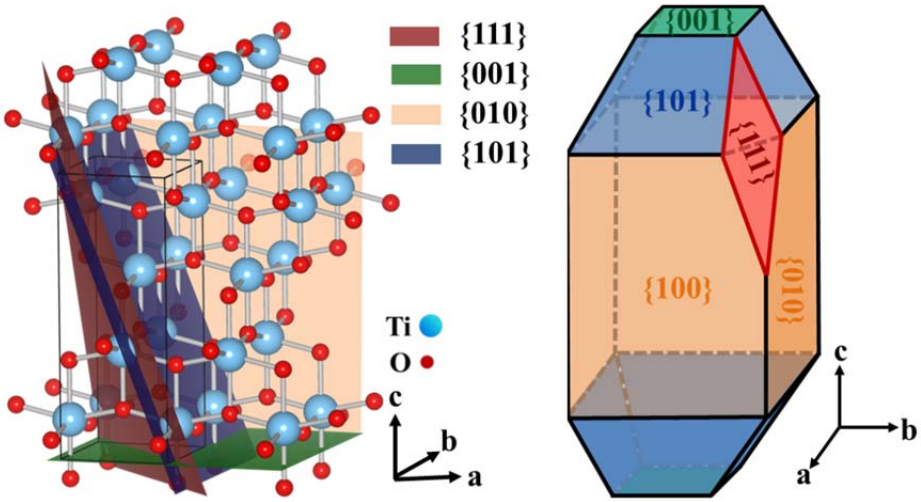

Figure 5.1 Schematic illustration of {101}, {100}, {001}, and {111} facets of anatase TiO_2, (a) molecular simulation model; (b) crystal model. (Notes: Anatase TiO_2 is in the tetragonal structure and belonging to the space group of $I4_1/amd$, in which $a = b = 3.782$ Å, $c = 9.502$ Å, thus {100} facet is equal to {010} facet in anatase TiO_2.)

To date, compared with the previously investigated {001}, {101}, and {100} facets for anatase TiO_2, few study has been concerned on the {111} facet, as illustrated in Figure 5.1. In this chapter, we report a facile process to prepare well-defined anatase TiO_2 single crystals exposed with {111} facets (T_{111}) which have never been realized experimentally before. The DFT theoretical calculations predict that the surface energy of {111} facet is up to 1.61 J/m^2 and large percentages of undercoordinated Ti atoms and O atoms existed on the surface. Experimentally, it is discovered that the conduction band minimum of this material is much higher than those of TiO_2 samples exposed with dominant {100}, {101}, and {001} facets (denoted as T_{100}, T_{101}, and T_{001}), indicating

that more reductive electrons can be produced on T_{111} then take part in the photoreaction to reduce H^+ into H_2. Furthermore, the photocatalytic properties of T_{111} are evaluated, it is revealed that T_{111} is an excellent photocatalyst with much higher photocatalytic activity, about 5 times, 9 times, and 13 times of T_{100}, T_{101}, and T_{001}, respectively. Both the superior surface atomic structure and electronic band structure significantly contribute to the enhanced photocatalytic performance.

The previous research reported that {100} facet was the most active facet for anatase TiO_2, which owns 100% Ti_{5c} atoms on its surface and superior electronic structure compared to that of {101} and {001} facets.[9] However, in this study, {111} facet is proved to be the more active crystal facet than {100} facet, which exhibits excellent properties in both the surface atomic structure and electronic structure.

5.2 Experimental Section

5.2.1 Synthesis of TiO_2 Exposed with Dominant {111} Facet

In a typical synthesis procedure of TiO_2 single crystals exposed with {111} facet, firstly, 3 mmol of TiF_4 (Aldrich) was added into the 100 mL of mixed solution of ethanol (Wako) and acetonitrile (Wako); then 0.6 mL of ammonia (Wako) was added slowly into the above solution. After stirred at room temperature for 48 h, the white suspension was centrifugated and the followed precipitation was dried at 60 ^oC for 3 h to get the gel-like precursor (denoted as TFN). In order to get the final single crystalline TiO_2, the Ti precursor (TFN) was heated at 500 ^oC for 2 h with a temperature ramping rate of 1 ^oC/min in the air atmosphere. After the combustion process, loosely TiO_2 powder was obtained. Furthermore, the obtained samples need to be calcined in the air

atmosphere at 600 ^{o}C for 2 h to clean the surface for the photocatalytic test. This as-prepared TiO_2 sample was denoted as T_{111}.

In order to verify the effects of the stabilizers of both F^- and ammonia, two control experiments in the absence of F^- or ammonia were conducted. The synthetic procedure was similar to that of T_{111}, but with different starting reagents. In the first control experiment, we used $TiCl_4$ to instead the TiF_4; while in the second one, pure water was used as the hydrolysis reagents without ammonia. The final TiO_2 powders prepared in the two control experiments were denoted as TCN and TF, respectively.

5.2.2 Synthesis of TiO_2 Exposed with Major {001}, {010}, and {101} Facets

In comparison with T_{111}, TiO_2 samples with exposed {001}, {100}, and {101} facets were prepared via solvothermal method reported in the literature as below[9]: 64, 32, 32 mg of titanium oxysulfate ($TiOSO_4 \bullet xH_2O$) (Aldrich) was dissolved in the HF solution (Aldrich) with concentrations of 120, 40, and 80 mM to prepare the precursors of TiO_2 with {001}, {100}, and {101} facet exposed, respectively. Then 40 mL of the $TiOSO_4$ solution were transferred to the Teflon-lined autoclave and heated at 180 ^{o}C for 12, 2, and 12 h for the {001}, {100}, and {101} facet exposed TiO_2, respectively. After reaction, the products were collected by centrifugation and washed with deionized water then dried at 80 ^{o}C in air for 12 h. In order to remove the surface fluorine, all the products were calcined in the air atmosphere at 600 ^{o}C for 2h. The samples with {001}, {100}, and {101} facets exposed were denoted as T_{001}, T_{100}, and T_{101}, respectively, and the related morphologies were observed by the SEM images as shown in Figure 5.2.

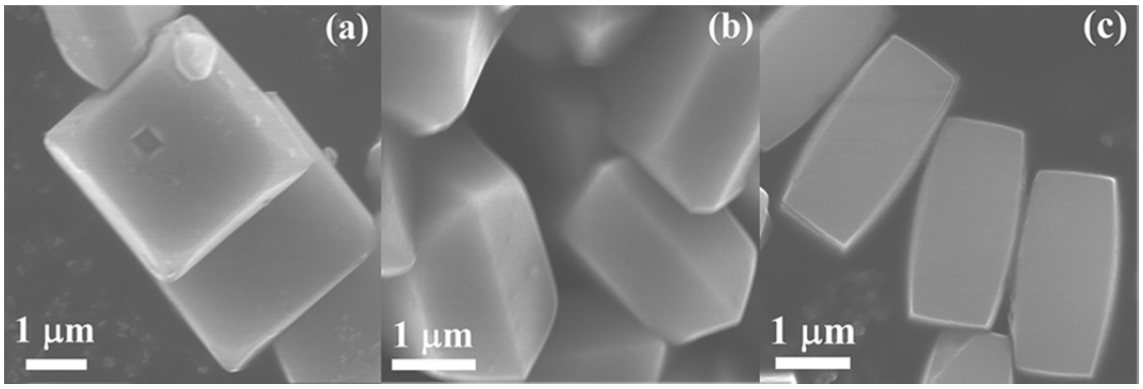

Figure 5.2 The SEM images of the TiO_2 samples. (a) T_{001}, (b) T_{101}, and (c) T_{100}. The average percentages of {001}, {101}, and {100} facets were calculated to be (40% {001}, 60% {101}, 0% {100}), (24% {001}, 76% {101}, 0% {100}), and (14% {001}, 33% {101}, 53% {100}) for T001, T101, and T100, respectively.

5.2.3 Characterization

The X-ray diffraction (XRD) patterns of the prepared samples were conducted on a Rigaku Multiflex diffractometer (RINT 2000; Rigaku Corp., Japan) with monochromatized Cu K_a radiation (λ=1.54178 Å). Raman measurement was carried out using a Raman spectroscopy (NRS-1000; Jasco Corp. Japan). The size and morphology of the samples were observed with a scanning electron microscope (SEM, JSM-6701F, JEOL Co., Japan) and transmission electron microscope (TEM, JEM-200 CX, JEOL) operating at 200 kV. The low temperature Electron Paramagnetic Resonance (EPR) spectra of the TiO_2 samples were recorded at 4 K to confirm the presence of oxygen vacancy on JEOL JES-FA200 Electron Spin Resonance Spectrometer. UV-visible absorption spectra were measured on a UV-visible spectrophotometer (UV-2500PC, Shimadzu Co., Japan). X-ray Photoelectron Spectroscopy (XPS) were performed on Thermo ESCALAB250 using monochromatized Al K_a at $h\upsilon$ = 1486.6 eV. The binding energies were calibrated to the C_{1s} peak by 284.6 eV. The Brunauer-Emmett-Teller

(BET) surface areas were recorded by a surface area analyzer (BEL Sorp-Ⅱ mini, BEL Japan Co., Japan) with nitrogen absorption at 77 K.

5.2.4 Theoretical Calculations

The calculations of the surface structure were based on the density-functional theory (DFT), as implemented in the VASP code.[10] The exchange-correlation energy was represented by the generalized-gradient approximation (GGA) of Perdew, Burke, and Ernzerhof (PBE).[11] The Ti $3s^2 3p^6 3d^2 4s^2$ and O $2s^2 2p^4$ were treated as valence electrons. The energy cutoff for the plane-wave basis set was 400 eV. The calculated crystal parameters for bulk anatase TiO_2 were a = 3.786 Å and c/a = 2.556, which were in good agreement with the experimental values.[12] A 6×6×6 Monk-horst k-point mesh was used for the Brillouin-zone integrations of the unit cell. For each surface, the supercells which were constructed from the relaxed unit cell of TiO_2 were periodically repeated along the surface normal and separated by vacuum layers. The constructed slabs with a vacuum thickness of ~10 Å can sufficiently suppress the interaction between adjacent slabs. The surface models were consisted of 144 atoms (24 unit cells of bulk TiO_2) for {111} and {001} planes, and 96 atoms (16 unit cells) for {100} and {101} planes, respectively. All atoms in the slabs were relaxed until the residual force was less than 0.02 eV/Å.

To further investigate the possibility of the oxygen vacancy existed on each surface, the surface energies of the reduced surfaces were also calculated. In the model structure, one oxygen atom was removed from each side of the {101}, {100}, {001}, and {111} slabs mentioned above. The geometries of the reduced surfaces were fully relaxed. The surface energy γ' of the reduced surface was given by

$$\gamma' = \frac{E_{\text{slab}}^{\text{reduced}} - nE_{\text{bulk}}}{2A} + \frac{\mu_{\text{O}}}{A}$$

, where $E_{\text{slab}}^{\text{reduced}}$ is the total energy of the reduced slab, and μ_0 is the chemical potential of oxygen, which is directly related to the O_2 partial pressure in ambient.

5.2.5 Photocatalytic H_2 Evolution Test

Photocatalytic reactions of H_2 evolution were carried out in a closed gas circulation system with an external-irradiation type of a glass reactor. The light source was a 300 W xenon lamp. The intensity of the light at 300–800 nm was measured to be 240 mW/cm^2 by using a spectroradiometer (USR-40; Ushio Inc., Japan). The co-catalyst Pt was loaded by an in-situ photodeposition method. The 0.5 wt% of Pt-loaded catalyst (60 mg) was dispersed with a magnetic stirrer in an aqueous methanol solution (50 mL of CH_3OH and 220 mL of H_2O). The evolved gas including H_2 was analyzed by an online gas chromatograph (GC-8A; Shimadzu) equipped with a thermal conductivity detector.

5.3 Results and Discussions

5.3.1 Crystal Structure and Morphology of the TiO_2 Single Crystals

As shown in Figure 5.3, the XRD patterns of the as-prepared TiO_2 samples (T_{001}, T_{101}, T_{100}, and T_{111}) can be indexed to the anatase TiO_2 (JCPDS No. 84-1286). The diffraction peaks at 25.32, 37.93, 48.02, 53.98, and 55.04^o are corresponding to the (101), (004), (200), (105) and (211) planes of anatase TiO_2, respectively. The differences in the peak intensity at 25.32^o (indexed to 101 crystal plane) and 37.93^o (indexed to 004 crystal plane) for the four TiO_2 samples are mainly related to the preferential crystallographic orientation of the crystal facets exposed. However, no corresponding characteristic peak for {111} facet can be observed in the XRD patterns. Structurally, anatase TiO_2

crystallizes in a tetragonal lattice, belonging to the space group of $I4_1/amd$. Only in the case of $h + k + l = 2n$ (n=1, 2, 3…), the diffraction peak will occur in the XRD pattern, thus the absence of (111) crystal plane is resulted from the extinction rules in the X-ray diffraction measurements.[12]

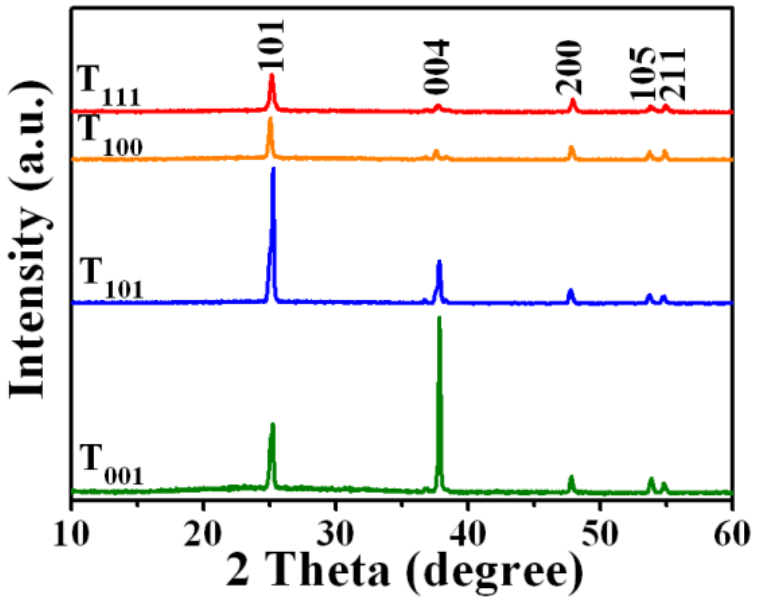

Figure 5.3 XRD patterns of the TiO_2 samples (T_{001}, T_{101}, T_{100}, and T_{111}).

In order to further confirm the TiO_2 samples were pure anatase, the Raman spectra were measured to identify the crystal structure of all the four prepared TiO_2 samples. As shown in Figure 5.4, the peaks appeared at 396, 515, and 638 cm^{-1} are corresponding to the B_{1g}, A_{1g}, and E_g peaks of anatase TiO_2, respectively.[13] Obviously, the peak positions of all the four prepared TiO_2 samples (T_{111}, T_{100}, T_{101}, and T_{001}) are similar, no other additional peaks indexed to rutile can be found. Therefore, we can prove that all the four prepared TiO_2 samples (T_{111}, T_{100}, T_{101}, and T_{001}) are pure anatase.

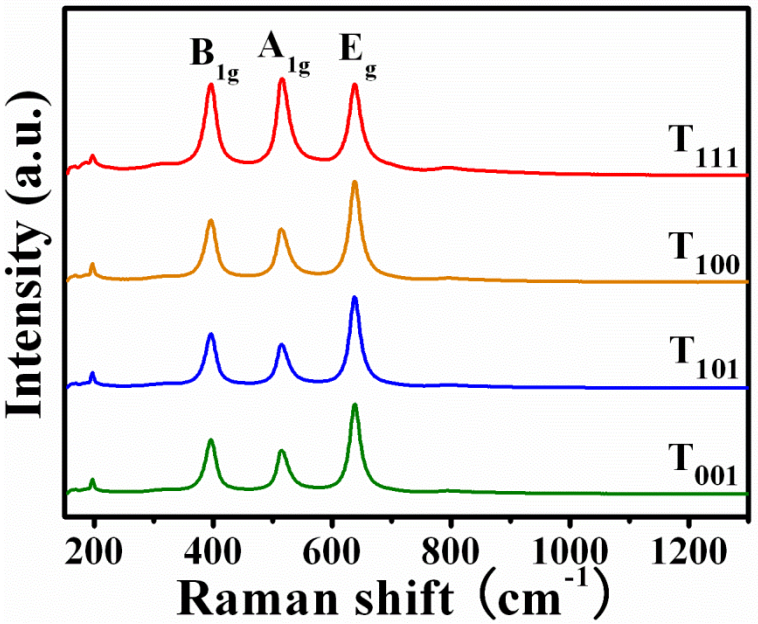

Figure 5.4 Raman spectra of the prepared TiO_2 samples (T_{111}, T_{001}, T_{100}, and T_{101}).

The morphology of the TiO_2 sample (T_{111}) was observed by the SEM image (Figure 5.5a), which was consisted of some square-like plates. As shown in Figure 5.5b, a square-shaped plate (400 × 400 nm^2) with a thickness of 50 nm in high-magnification was observed. Furthermore, a detailed study was carried out to verify the crystal facet of the square-shaped nanoplates via TEM (Figure 5.5c). The corresponding electron diffraction (SAED) pattern (inset in Figure 5.5c) confirms that the square-shaped crystalline is single crystal, and the zone axis is indexed to be [111]. Additionally, based on the analysis of the high-resolution TEM (HRTEM) image (Figure 5.5d), the interfacial angle between the (101) and (011) atomic planes (the same lattice spacing of 0.35 nm) of anatase TiO_2 is 82°, we can confirm that the exposed crystal plane is {111} facet. To the best of our knowledge, this is the first report about the single crystalline TiO_2 with {111} facet exposed. Based on the SEM and TEM images, the percentage of the {111} facets on T_{111} is calculated to be about 72% in average.

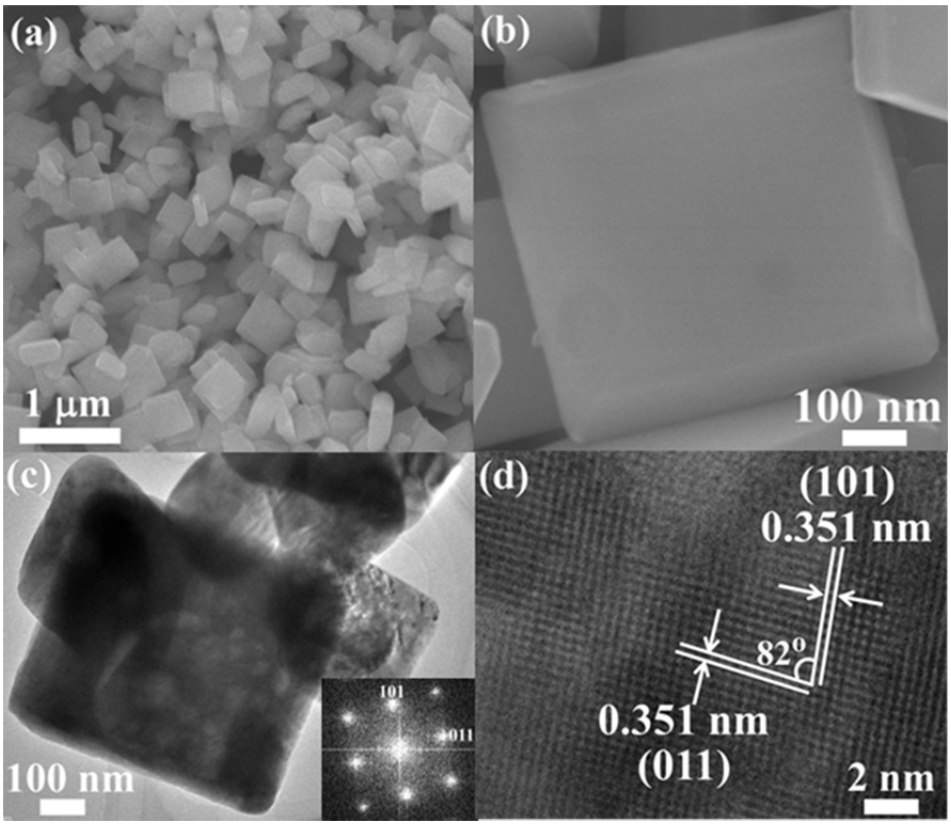

Figure 5.5 SEM (a, b), TEM (c), and HRTEM (d) images of the single crystalline TiO_2 exposed with {111} crystal facets.

5.3.2 Theoretical Calculations

Based on the above experimental findings, the surface structure of the {111} crystal facet was further theoretically studied via the density functional theory (DFT) calculation in comparison with the reported {001}, {100}, and {101} facets. The representative relaxed atomic geometries of each slab are shown in Figure 5.6. Accounting from the slab models, the surface atomic structures of each facets are described as below. On the {111} surface, all the Ti and O atoms on the top layer are undercoordinated: Ti atoms are fivefold- and threefold-coordinated (Ti_{5c} and Ti_{3c}) with the ratio of Ti_{3c} to Ti_{5c} is 1:3, and O atoms are twofold coordinated (O_{2c}). On the {001} surface, only Ti_{5c} atoms are present as well as O_{2c} and O_{3c} atoms. On the {100} surface,

we note that besides the outmost Ti_{5c} atoms on the top layer, the fully (sixfold)-coordinated Ti (Ti_{6c}) atoms are also exposed on the second layer. In addition, both O_{2c} and O_{3c} atoms are existed on the surface of {100}. On the {101} surface, both Ti_{6c} and Ti_{5c} atoms are present as well as O_{2c} and O_{3c} atoms. Apparently, {111} surface has favorable atomic structure, on which the large percentage of undercoordinated Ti atoms (Ti_{5c} and Ti_{3c}) can act as the active reaction sites in the photocatalytic reaction.[14,15]

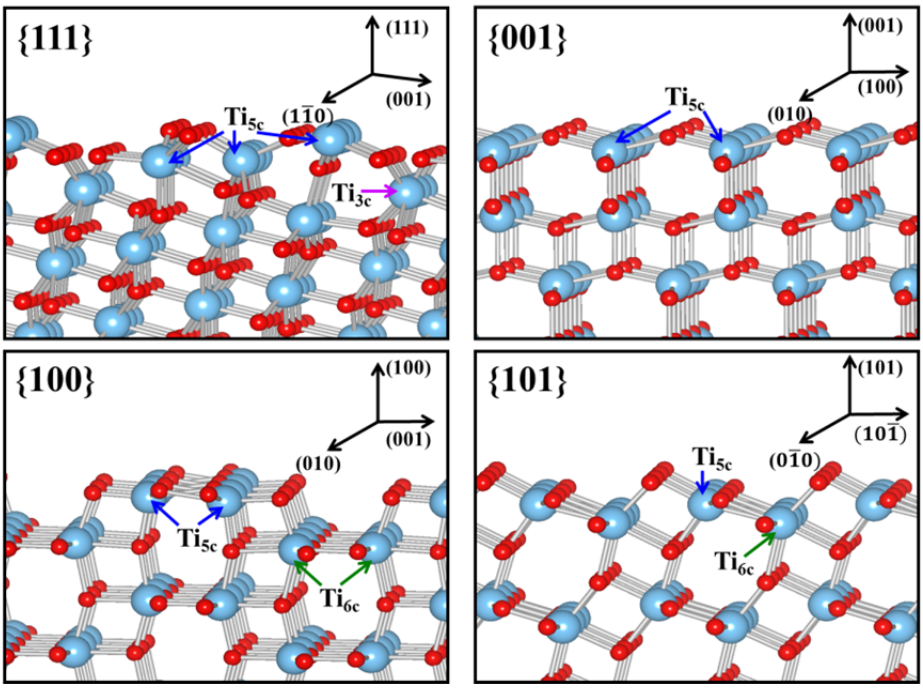

Figure 5.6 Surface structures of the relaxed stoichiometric {111}, {001}, {100}, and {101} facets on anatase TiO_2.

Meanwhile, the surface energy (γ) of each facet was calculated by the formula:

$$\gamma = \frac{E_{\text{slab}} - nE_{\text{bulk}}}{2A}$$

, where E_{slab} is the total energy of the slab, E_{bulk} is the total energy of the bulk per unit cell, n is the number of bulk unit cells contained in the slab, and A is the surface area of

each side of the slab. The calculated surface energies are 1.61, 0.95, 0.57, and 0.43 J/m^2 for {111}, {001}, {100}, and {101} facets, respectively; the latter three surface energies are in well accordance with the values reported in the literature (as listed in Table 5.1).[16] However, to the best of our knowledge, the surface energy of {111} facet has never been reported. Compared with {001}, {100}, and {101} facets, the surface energy of {111} facet is much higher. The higher surface energy of {111} facet is partially attributed to the large percentage of undercoordinated Ti and O atoms, of which the ground state energy is higher in contrast with the fully coordinated atoms.

Table 5.1 Surface energies of each crystal facet for anatase TiO_2.

crystal facet	surface energy (J/m^2) this work	surface energy (J/m^2) GGA-PBE[16]
{101}	**0.43**	**0.44**
{100}	**0.57**	**0.53**
{001}	**0.95**	**0.90**
{111}	**1.61**	**-**

Generally, the facet with high surface energy will vanish rapidly during the crystal growth process to minimize the total crystal energy. In order to stabilize the reactive surface during the crystal growth process, the TiO_2 samples with exposed high-energy {001} and {100} facets were prepared by using HF,[9,17-27] NH_4F,[28-30] or any other capping reagents (such as 1-butyl-3-methylimidazolium tetrafluoroborate,[25,31] disodium ethylenediaminetetraacetate,[32] and diethylenetriamine[33]) as stabilizers to lower the surface energy for certain crystallographic crystal facets in the previous report.[34] Herein, anatase TiO_2 single crystals with high-surface-energy {111} facet exposed is obtained, which could be ascribed to the synergetic effect of the F^- and ammonia as the capping

reagents. The crystal growth mechanism was also investigated in detail as described in the supporting information (Figure 5.7-8).

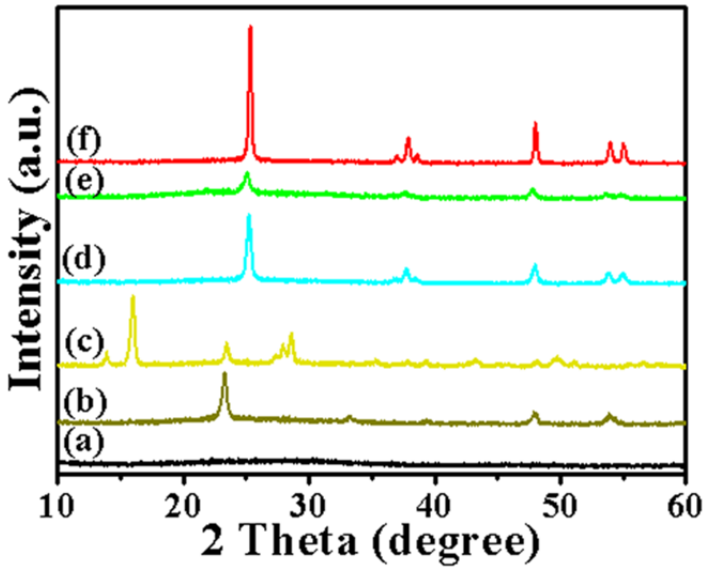

Figure 5.7 The XRD patterns of the TiO_2 precursors (a) TCN, (b) TF, (c) T_{111}, and the related samples after calcination (d) TCN, (e) TF, (f) T_{111}, respectively.

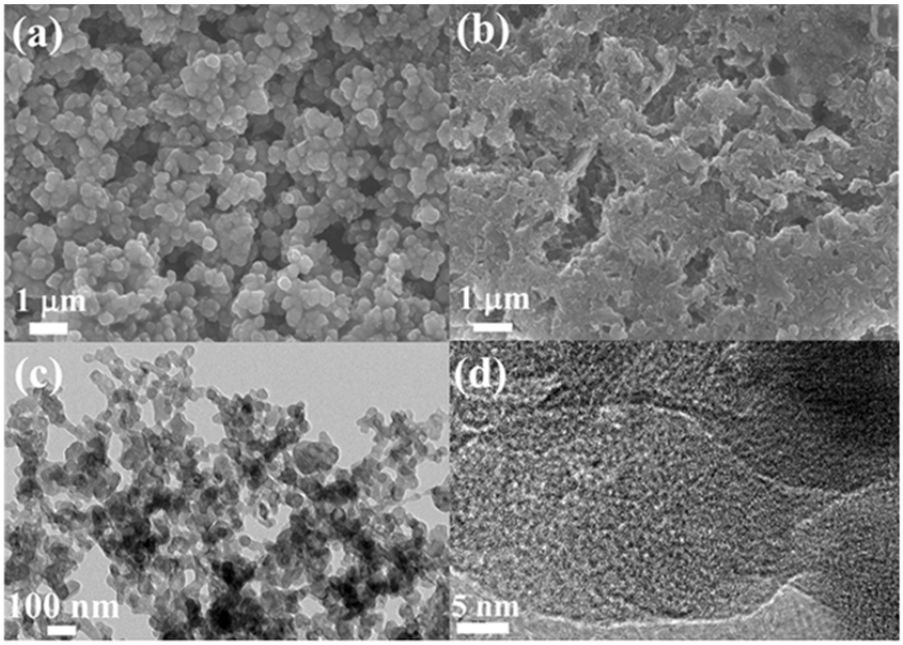

Figure 5.8 The SEM images of TCN (a) and TF (b), as well as the TEM images of the precursor of T_{111} (c, d).

As shown in Figure 5.7, the XRD patterns are indexed to be weak-crystalline rutile TiO_2 and $TiOF_2$ (JCPDS No. 77-132) for the TiO_2 precursors synthesized without F^- or ammonia, respectively (Figure 5.7). After the heating treatment at 500 ^oC for 2 h, the XRD patterns of the two samples (TCN and TF) are all indexed to anatase TiO_2 (JCPDS No. 71-1167) but different in crystallinity. The morphology of the two TiO_2 samples is observed by the SEM images (Figure 5.8). For the Cl-instead-F TiO_2 (TCN), there are some sphere-like aggregates consisted of small nanoparticles (Figure 5.8a), while only some irregular aggregates of nanoparticles can be observed for the TiO_2 prepared without ammonia (TF) as shown in Figure 5.8b. No square-plates can be detected in the two TiO_2 samples (TCN and TF). Moreover, to elucidate the formation process of the {111} facet exposed TiO_2, the precursor of the {111} exposed TiO_2 is collected. The precursor (TFN) existed in the form of $(NH_4)_2(TiF_4O)$ (JCPDS No. 82-1330) (Figure 5.7) with the morphology of irregular nanoparticles connected with each other (Figure 5.8c), and the connection interface can be further observed clearly by the high magnified TEM image (Figure 5.8d). Although we could not understand the exact growth mechanism, we would like to propose that both F anions and ammonia together played the important role to adsorb on the crystal facet of TiO_2 during the first crystallization process to form Ammonium Titanium Oxide Fluoride $(NH_4)_2(TiF_4O)$, then after a calcination process, left the TiO_2 plates with exposed {111} facets.

In addition, the numerous undercoordinated O atoms (100% O_{2c}) existed on the {111} surface can facilitate the formation of oxygen vacancy, which will affect the photocatalytic performance via acting as active sites in the photoreaction.[35] In order to verify the possibility of the existence of oxygen vacancy existed on the TiO_2 surface, the surface energy of the reduced {111} surface was theoretically calculated in comparison

with other crystal facets such as {001}, {100}, and {101}. As shown in Figure 5.9, the intersection of the ideal and reduced surface curves gives the transition value of ~ -1.61 eV for the {111} facet, which is much higher than that of the {001} (~ -3.76 eV), {100} (~ -4.25 eV), and {101} (~ -4.52 eV) facets. These results indicates that the oxygen vacancies can be more easily created on the {111} surface than that on the {001}, {100}, and {101} surfaces, and oxygen vacancies start to form on the {111} surface even under a relatively high O_2 pressure.[7]

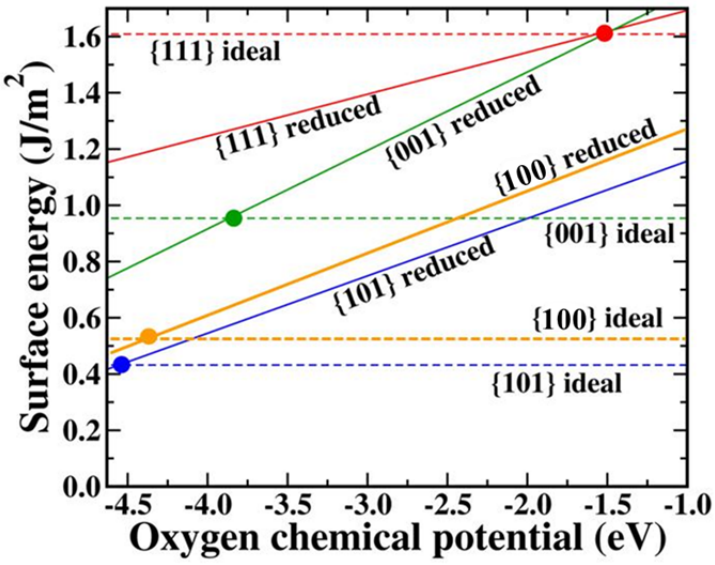

Figure 5.9 Surface energies of reduced and ideal surfaces of {111}, {001}, {100}, and {101} facets.

Later, to get a more convincing experimental evidence, we also adopted the low temperature electron paramagnetic resonance (EPR) spectra to check the existence of the oxygen vacancies on the TiO_2 surface. As shown in Figure 5.10, the signal observed at g = 2.002 is the characteristics of oxygen vacancy existed on the surface of TiO_2.[36] The intensity of the signal appeared in T_{111} is much stronger than that of T_{100}, T_{101}, and T_{001}, indicating that more oxygen vacancies are existed on the surface of T_{111}. These

oxygen vacancies can act as active sites in the photocatalytic reaction, which are beneficial for the enhancement of the photocatalytic efficiency.

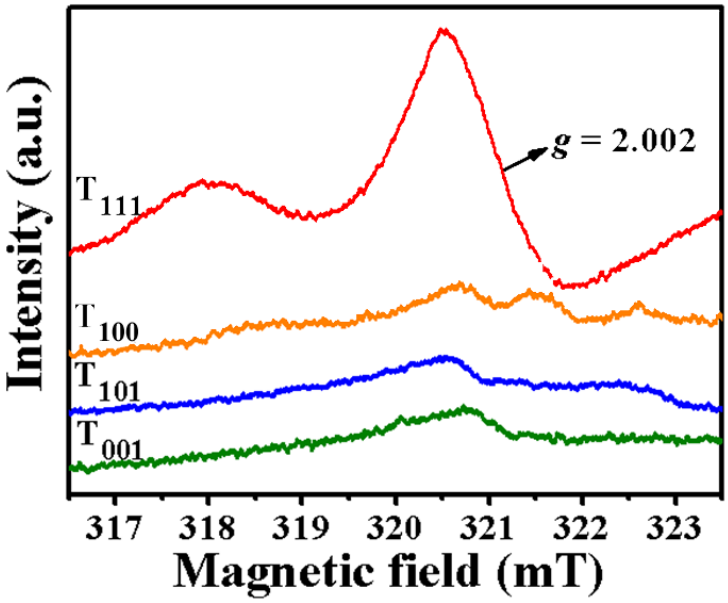

Figure 5.10 EPR spectra of the TiO_2 samples (T_{111}, T_{001}, T_{100}, and T_{101}).

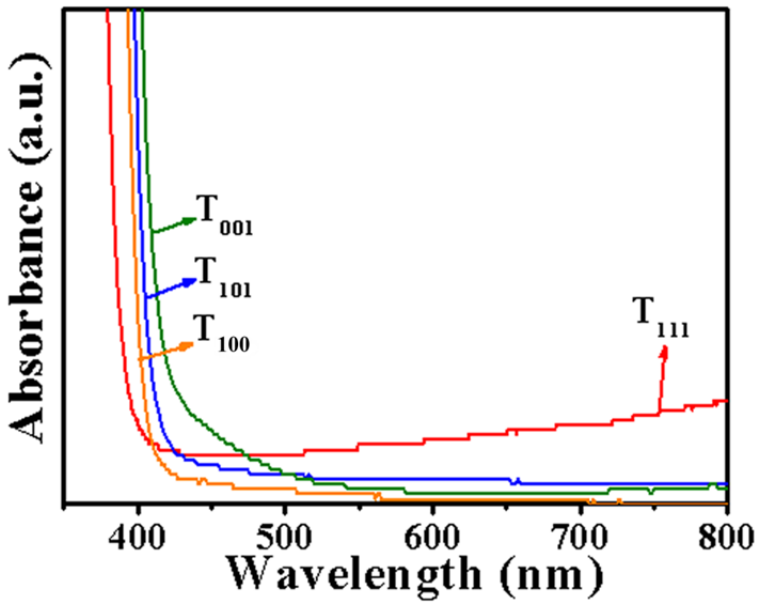

Figure 5.11 UV-visible absorption spectra of the TiO_2 samples (T_{111}, T_{001}, T_{100}, and T_{101}) in the enlarge range of 350-800 nm.

As shown in Figure 5.11, the UV-visible absorption spectra were enlarged in order to observe the differences among the four TiO_2 samples in the range of 500-800 nm more clearly. Compared with the other three TiO_2 samples (T_{100}, T_{101}, and T_{001}), T_{111} exhibits stronger absorption beyond 500 nm up to the infrared range, which is resulted from the existence of oxygen vacancy. Because the concentration of oxygen vacancy is low, we can only observe a slight slope.

5.3.3 Electronic Structure of the TiO_2 Single Crystals

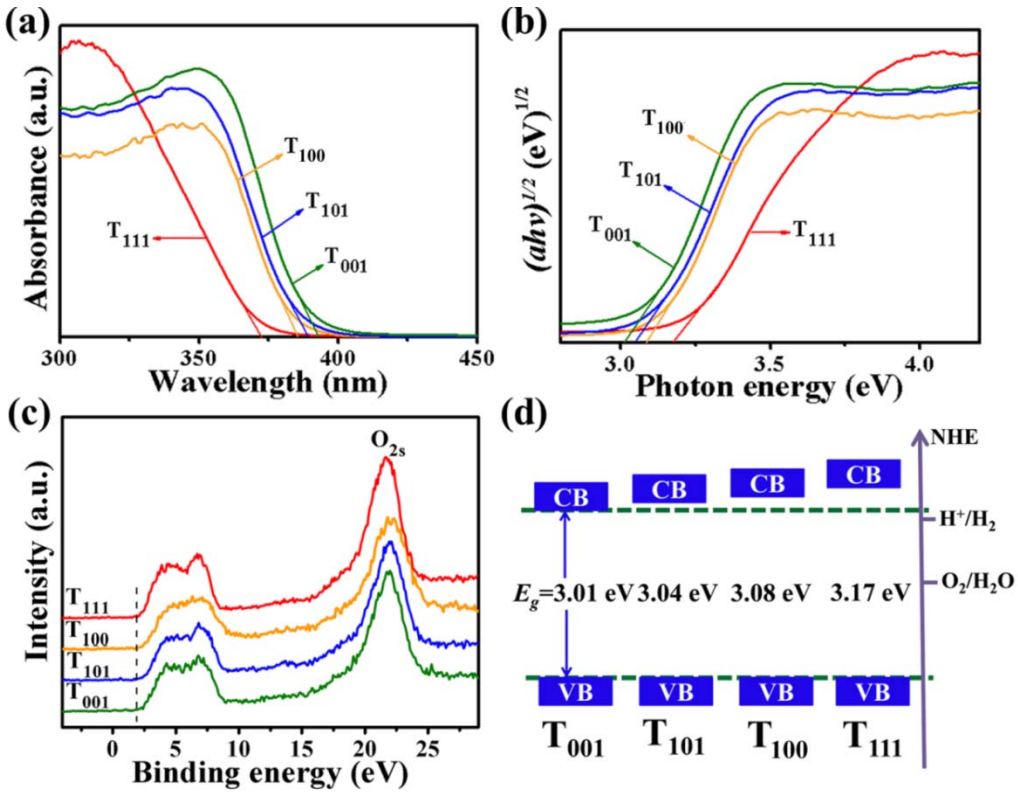

Figure 5.12 (a) UV-visible absorption spectra of the TiO_2 samples. (b) Their corresponding plots of transformed Kubelka-Munk function versus the energy of photon. (c) Valence-band XPS spectra of the four TiO_2 samples. (d) Schematic illustration of the determined valence-band (VB) and conduction-band (CB) edges of T_{001}, T_{101}, T_{100}, and T_{111}.

In parallel, the electronic band structures of the four TiO_2 samples, which will also affect their photocatalytic efficiencies, were deduced from the UV-visible absorption spectra and valence band XPS spectra. As shown in Figure 5.12a, the UV-visible absorption spectra demonstrate that, the absorption edges of T_{111}, T_{100}, T_{101}, and T_{001} are nearly 371, 385, 388, and 392 nm, respectively. TiO_2 is known as an indirect semiconductor, for which the relation between the absorption coefficient (a) and incident photon energy (hv) can be written as $a = B_i(hv\text{-}E_g)^2/hv$, where B_i is the absorption constant for indirect transitions.[37] The band gaps of the TiO_2 samples are calculated to be 3.01, 3.04, 3.08, and 3.17 eV for T_{001}, T_{101}, T_{100}, and T_{111}, respectively (Figure 5.12b). Since each facet owns its own unique surface atomic arrangement, which will result in different electronic configuration from other facet, thus TiO_2 single crystals exposed with various crystal facets will exhibit different electronic band structures.[9,38] As shown in Figure 5.12c, the valence band XPS spectra reveal that the VB maxima of all the four TiO_2 samples are similar. Consequently, the order of the potential of the conduction band minimum are $T_{111} > T_{100} > T_{101} > T_{001}$ (Figure 5.12d).

In the photocatalytic reaction, considering the effect of the electronic band structure, the TiO_2 sample with a higher conduction band minimum which can generate more reductive electrons to take part in the photocatalytic reaction will show superior photocatalytic activity.[39] Hence, among these four TiO_2 samples, T_{111} possesses a superior electronic band structure, in which more strongly reductive electrons can be generated, then transferred to the TiO_2 surface to take part in the photocatalytic reaction.

5.3.4 Photocatalytic H_2 Evolution of the TiO_2 Single Crystals

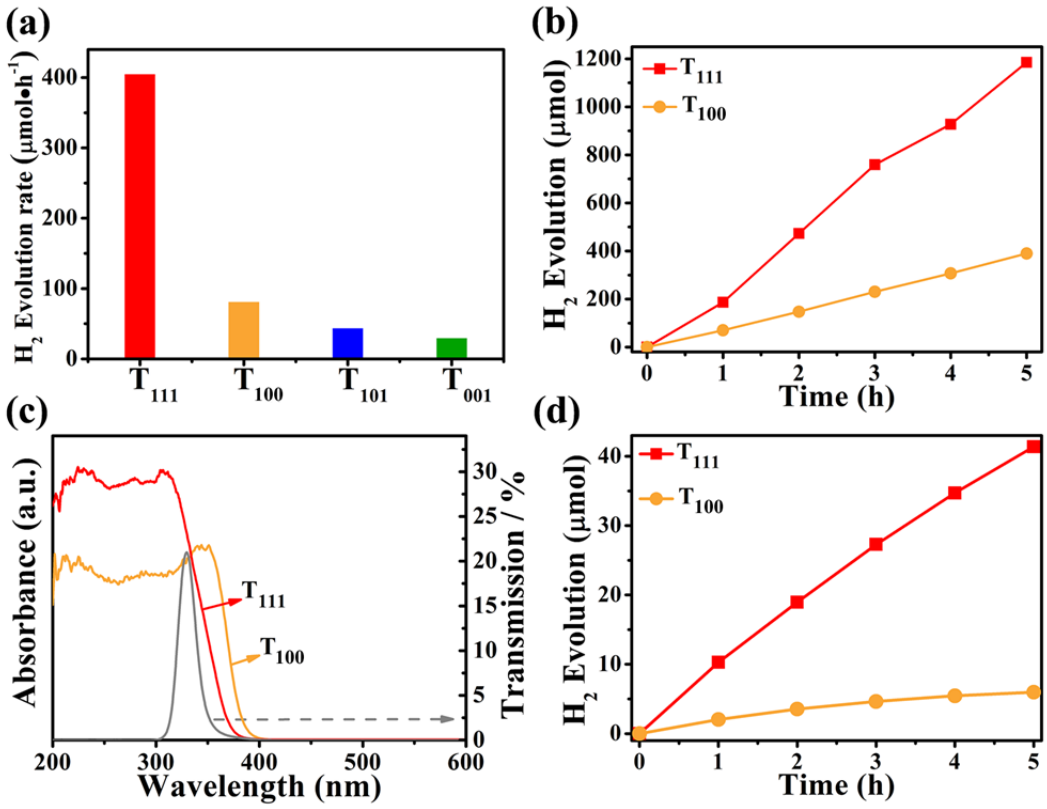

Figure 5.13 (a) Photocatalytic water splitting tests of the Pt-loaded (0.5%) TiO_2 samples with the same mass of 60 mg under UV-visible light irradiation (λ > 300 nm). (b) Comparison of photocatalytic activities between T_{111} (20 mg × 11.6 m^2/g = 0.232 m^2) and T_{100} (60 mg × 3.96 m^2/g = 0.237 m^2) with same surface area (ca. 0.23 m^2) under UV-visible light irradiation (λ > 300 nm). (c) UV-visible absorption spectra of T_{111} and T_{100}, and the light transmission spectrum of the monochromatic filter centered at a wavelength of 327.5 nm ($\Delta\lambda$ = ± 18.5 nm) (gray curve). (d) Comparison of photocatalytic activities between T_{111} and T_{100} with the same surface area of ca. 0.23 m^2 under the monochromatic light irradiation λ = 327.5 nm ($\Delta\lambda$ = ± 18.5 nm).

Furthermore, the photocatalytic H_2 evolution from an aqueous methanol solution was employed for evaluation of the photocatalytic property of T_{111} as well as the other TiO_2

samples (T_{100}, T_{101}, and T_{001}). As shown in Figure 5.13a, T_{111} exhibits obviously higher photocatalytic activity with the H_2 evolution rate of 405.2 μmol•h^{-1}, about 5 times of T_{100} (81.1 μmol•h^{-1}), 9 times of T_{101} (43.9 μmol•h^{-1}), and 13 times of T_{001} (29.9 μmol•h^{-1}). Among them, although Ti_{5c} is exposed 100% on the {001} surface and the surface energy of {001} facet is the second highest, the photocatalytic activity of T_{001} is the lowest. The low photocatalytic performance is resulted from its poor electronic band structure, which has been explained in detail in the previous report.[9] Herein, in this study, we only compared the photocatalytic performance between T_{111} and T_{100} (T_{100} was the most efficient photocatalyst in the previous study).

In general, the photocatalytic activity can be affected by various factors, such as crystallinity and surface area.[40] In this study, the crystallinity of the TiO_2 samples is hard to identify via the XRD patterns because of the preferential crystallographic orientation of each crystal facet. However, both T_{111} and T_{100} were heated at 600 ^oC in a static air atmosphere for 2 h to clean the surface before the photocatalytic test, thus the effect of crystallinity can be ignored based on the same calcination temperature. Moreover, considering the surface area, the Brunauer-Emmett-Teller (BET) specific surface areas are 11.6 and 3.96 m^2/g for T_{111} and T_{100}, respectively (Table 5.2). Taking the surface area into account, based on the data from Figure 5.13a, the photocatalytic activities are calculated to be 582.1 and 341.3 μmol•h^{-1}•m^{-2}) for T_{111} and T_{100}, respectively. In addition, we also experimentally tested the photocatalytic performance of the two photocatalysts (T_{111} and T_{100}) in the same surface area of ca. 0.23 m^2 (Figure 5.13b). In this case, the photocatalytic activity of T_{111} is about 3 times of T_{100} as shown in Figure 5b. Therefore, based on the above analysis, both the calculation and experimental results confirm that T_{111} exhibits higher specific activity than that of T_{100}.

Table 5.2 BET surface areas of the prepared TiO_2 samples.

	T_{111}	T_{100}	T_{101}	T_{001}	T_{O_2}
BET surface area (m^2/g)	11.6	3.9	1.9	1.3	10.8

Moreover, we should consider that the light absorption abilities for the two photocatalysts (T_{111} and T_{100}) under the UV-visible light irradiation are different (Figure 5.13c). The number of the absorbed photons between 300-400 nm were calculated to be 0.254 μmol/s and 0.367 μmol/s for T_{111} and T_{100}, respectively, via the method reported in our previous study.[41] It is apparent that the absorbed photons for T_{100} are approximately 1.5 times of T_{111}. Hence, their photocatalytic performances under monochromatic light centered at a wavelength of 327.5 nm ($\Delta\lambda = \pm 18.5$ nm) were also studied. As shown in Figure 5.13c, the light-absorption difference between T_{111} and T_{100} can be eliminated under this condition. In this way, it is worthy of note that T_{111} still exhibits a significantly higher photocatalytic activity (8.2 μmol•h^{-1}), more than 6 times of T_{100} (1.2 μmol•h^{-1}) (Figure 5.13d).

Finally, in order to investigate the contribution of oxygen vacancy worked on the enhancement of the photocatalytic activity, the control experiment related to the oxygen vacancy on T_{111} surface have been done. Instead of treating T_{111} into air atmosphere at 600 ^oC to clean the surface, we treated T_{111} into the pure O_2 atmosphere at 600 ^oC to obtain the oxygen-vacancy-free sample (denoted as T_{O_2}). The EPR spectra confirm that there is almost no oxygen vacancy existed on the T_{O_2} surface (Figure 5.14a). T_{O_2} exhibits a slightly better crystallinity (resulted from the oxygen-rich heat-treatment environment than that of T_{111}) (Figure 5.14b) and similar light absorption edge (Figure 5.14c) to that of T_{111}. The slightly higher absorption in the range of 500-800 nm for T_{111}

is ascribed to the small amounts of oxygen vacancy existed on the T_{111} surface (inset of Figure 5.14c). As shown in Figure 5.14d, it is revealed that the photocatalytic activity of T_{O_2} without oxygen vacancy is 0.75 times of T_{111} with small amount of oxygen vacancies, proving that the suitable amounts of oxygen vacancy existed on the T_{111} surface is indeed beneficial for the promotion of the photocatalytic performance.

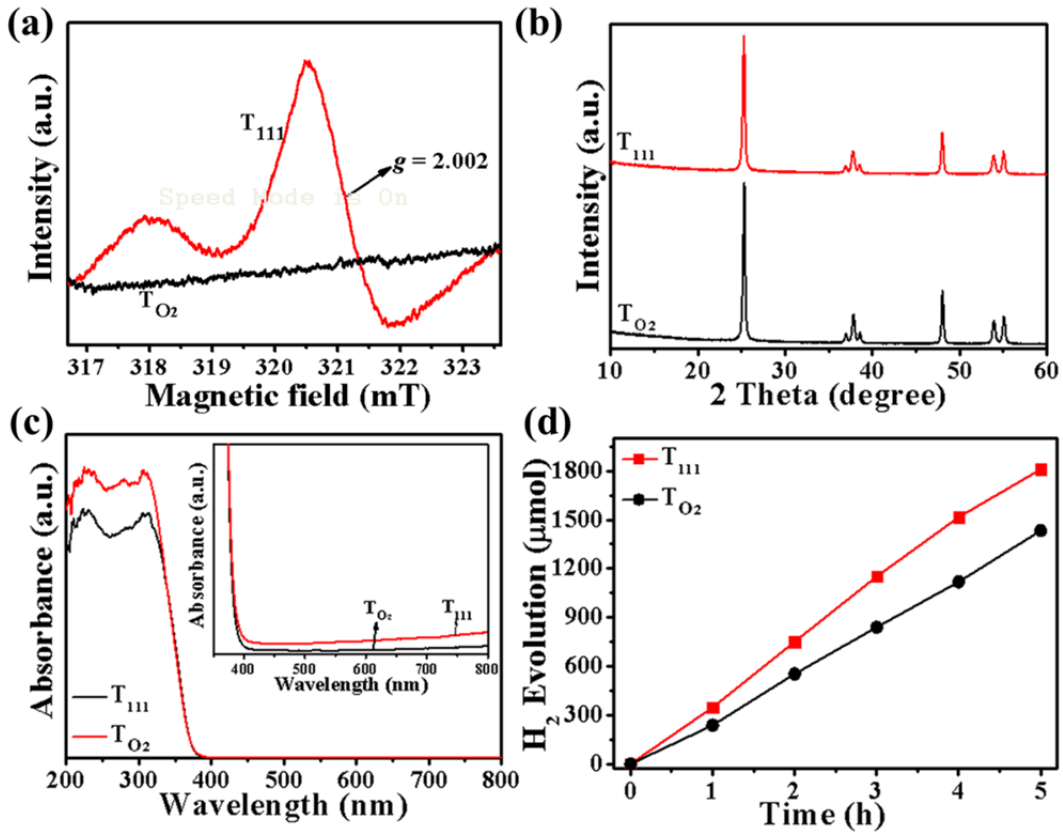

Figure 5.14 (a) EPR spectra of T_{111} (treated in the air atmosphere) in comparison with that of T_{O_2} (T_{111} treated in the O_2 atmosphere). (b) Comparison of XRD patterns between T_{111} and T_{O_2}. (c) UV-visible absorption spectra of the TiO_2 samples (T_{111} and T_{O_2}). (d) Comparison of photocatalytic activities between T_{111} and T_{O_2} under UV-visible light irradiation ($\lambda > 300$ nm).

5.3.5 Discussion about the Enhancement of Photocatalytic Activity

Based on the above theoretical analysis and experimental results, we can address that the vital factor for the higher photocatalytic performance of T_{111} is the superior surface properties owned by {111} facet. Because of its particular surface structure, the surface atomic coordination and arrangement of {111} facet are obviously different from other facets (Figure 5.6). Accordingly, TiO_2 sample with dominant {111} facet exposed exhibited good candidate characters in both surface atomic structure (the density of undercoordinated atoms) and electronic band structure for the excellent photoreactivity, which can be explained in detail as below.

The first property relevant to the photocatalytic activity is the surface atomic structure. It is reported that a facet with a higher percentage of undercoordinated atoms are usually more reactive in the heterogeneous reactions. These undercoordinated Ti atoms on the TiO_2 surface can act as the catalytically active sites for the photoreaction.[42,43] On the {111} surface, all Ti atoms are undercoordinated (25% Ti_{3c} and 75% Ti_{5c}). Compared with {100} (100% Ti_{5c}), {001} (100% Ti_{5c}), and {101} (50% Ti_{5c} and 50% Ti_{6c}), the photoreactivity of {111} surface is thus expected to be higher than those of other facets. What's more, the formation of oxygen vacancies on the {111} surface, which is facilitated by the presence of numerous undercoordinated O atoms (100% O_{2c}), can also offer more active sites on the {111} surface, thus enhance the photocatalytic activity.[35] Another key issue influencing the photocatalytic efficiency is the electronic band structure. Based on the deduced electronic band structures of the four TiO_2 samples (T_{111}, T_{100}, T_{101}, and T_{001}), the conduction band minimum of T_{111} is the highest, hence the more strongly reductive electrons can be produced then transferred to the surface Pt sites to reduce H^+ into H_2.[39] Thereby, compared with the previous report in which the photoreactivity only can be promoted by one or two times via facet control,[9] herein, via

optimizing both the surface atomic structure and electronic band structure, T_{111} exhibits the obviously higher photocatalytic activity, about five times of T_{100} (Figure 5.13a).

5.4 Conclusion

The well-defined {111} facets exposed TiO_2 single crystals are synthesized via both F^- and ammonia as the capping reagents. This TiO_2 sample exhibits an obviously higher photocatalytic activity in comparison to TiO_2 samples exposed with majority {001}, {101}, and {100} facets. The largely enhanced photocatalytic activity can be attributed to its superior surface atomic structure (large percentage of undercoordinated atoms on the TiO_2 surface to act as the active sites for the photoreaction) and electronic band structure (higher conduction band minimum on which more reductive electrons can be generated). This fundamental understanding shows that the facet control of semiconductors allows the optimization of both the surface atomic structure and electronic band structure, thus largely promotes the photocatalytic efficiency. This study evidences that the surface-structural engineering of semiconductors is an effective approach to achieve advanced and excellent performance over photocatalysts.

Reference:

(1) Yi, Z. G.; Ye, J. H.; Kikugawa, N.; Kako, T.; Ouyang, S. X.; Stuart-Williams, H.; Yang, H.; Cao, J. Y.; Luo, W. J.; Li, Z. S.; Liu, Y.; Withers, R. L. *Nature Mater.* **2010**, *9*, 559.

(2) Tong, H.; Ouyang, S. X.; Bi, Y. P.; Umezawa, N.; Oshikiri, M.; Ye, J. H. *Adv. Mater.* **2012**, *24*, 229.

(3) Ouyang, S. X.; Tong, H.; Umezawa, N.; Cao, J. Y.; Li, P.; Bi, Y. P.; Zhang, Y. J.; Ye, J. H. *J. Am. Chem. Soc.* **2012**, *134*, 1974.

(4) Tu, W. G.; Zhou, Y.; Liu, Q.; Tian, Z. P.; Gao, J.; Chen, X. Y.; Zhang, H. T.; Liu, J. G.; Zou, Z. G. *Adv. Funct. Mater.* **2012**, *22*, 1215.

(5) Tang, J. W.; Zou, Z. G.; Ye, J. H. *Angew. Chem. Int. Ed.* **2004**, *43*, 4463.

(6) Chen, J. S.; Tan, Y. L.; Li, C. M.; Cheah, Y. L.; Luan, D. Y.; Madhavi, S.; Boey, F. Y. C.; Archer, L. A.; Lou, X. W. *J. Am. Chem. Soc.* **2010**, *132*, 6124.

(7) Bi, Y. P.; Ouyang, S. X.; Umezawa, N.; Cao, J. Y.; Ye, J. H. *J. Am. Chem. Soc.* **2011**, *133*, 6490.

(8) Jiang, J.; Zhao, K.; Xiao, X. Y.; Zhang, L. Z. *J. Am. Chem. Soc.* **2012**, *134*, 4473.

(9) Pan, J.; Liu, G.; Lu, G. Q.; Cheng, H. M. *Angew. Chem. Int. Ed.* **2011**, *50*, 2133.

(10) Kresse, G.; Furthmuller, J. *Comput. Mater. Sci.* **1996**, *6*, 15.

(11) Perdew, J. P.; Burke, K.; Ernzerhof, M. *Phys. Rev. Lett.* **1996**, *77*, 3865.

(12) Howard, C. J.; Sabine, T. M.; Dickson, F. *Acta Crystallogr. Sect. B* **1991**, *47*, 462.

(13) Ohsaka, T.; Izumi, F.; Fujiki, Y. *J. Raman. Spectrosc.* **1978**, *7*, 321.

(14) Gong, X. Q.; Selloni, A. *J. Phys. Chem. B* **2005**, *109*, 19560.

(15) Yang, K.; Dai, Y.; Huang, B. B.; Feng, Y. P. *Phys. Rev. B* **2010**, *81*, 033202.

(16) Lazzeri, M.; Vittadini, A.; Selloni, A. *Phys. Rev. B: Condens. Matter* **2001**, *63*, 155409.

(17) Yang, H. G.; Sun, C. H.; Qiao, S. Z.; Zou, J.; Liu, G.; Smith, S. C.; Cheng, H. M.; Lu, G. Q. *Nature* **2008**, *453*, 638.

(18) Yang, H. G.; Liu, G.; Qiao, S. Z.; Sun, C. H.; Jin, Y. G.; Smith, S. C.; Zou, J.; Cheng, H. M.; Lu, G. Q. *J. Am. Chem. Soc.* **2009**, *131*, 4078.

(19) Liu, M.; Piao, L. Y.; Zhao, L.; Ju, S. T.; Yan, Z. J.; He, T.; Zhou, C. L.; Wang, W. J. *Chem. Commun.* **2010**, *46*, 1664.

(20) Liu, G.; Sun, C. H.; Yang, H. G.; Smith, S. C.; Wang, L. Z.; Lu, G. Q.; Cheng, H. M. *Chem. Commun.* **2010**, *46*, 755.

(21) Han, X.; Kuang, Q.; Jin, M. S.; Xie, Z. X.; Zheng, L. *J. Am. Chem. Soc.* **2009**, *131*, 3152.

(22) Liu, G.; Yang, H. G.; Wang, X. W.; Cheng, L. N.; Pan, J.; Lu, G. Q.; Cheng, H. M. *J.Am.Chem. Soc.* **2009**, *131*, 12868.

(23) Liu, G.; Sun, C. H.; Smith, S. C.; Wang, L. Z.; Lu, G. Q.; Cheng, H. M. *J. Colloid Interface Sci.* **2010**, *349*, 477.

(24) Wang, X. W.; Liu, G.; Wang, L. Z.; Pan, J.; Lu, G. Q.; Cheng, H. M. *J. Mater. Chem.* **2011**, *21*, 869.

(25) Zheng, Z. K.; Huang, B. B.; Qin, X. Y.; Zhang, X. Y.; Dai, Y.; Jiang, M. H.; Wang, P.; Whangbo, M. H. *Chem. Eur. J.* **2009**, *15*, 12576.

(26) Xiang, Q. J.; Yu, J. G.; Jaroniec, M. *Chem. Commun.* **2011**, *47*, 4532.

(27) Yu, J. G.; Qi, L. F.; Jaroniec, M. *J. Phys. Chem. C*, **2010**, *114*, 13118.

(28) Liu, S. W.; Yu, J. G.; Jaroniec, M. *J. Am. Chem. Soc.* **2010**, *132*, 11914.

(29) Lv, K. L.; Yu, J. G.; Fan, J. J.; Jaroniec, M. *CrystEngComm* **2011**, *13*, 7044.

(30) Alivov, Y.; Fan, Z. Y. *J. Phys. Chem. C* **2009**, *113*, 12954.

(31) Zheng, Z. K.; Huang, B. B.; Qin, X. Y.; Zhang, X. Y.; Dai, Y. *Chem. Eur. J.* **2010**, *16*, 11266.

(32) Ma, X. Y.; Chen, Z. G.; Hartono, S. B.; Jiang, H. B.; Zou, J.; Qiao, S. Z.; Yang, H. G. **2010**, *46*, 6608.

(33) Chen, J. S.; Tan, Y. L.; Li, C. M.; Cheah, Y. L.; Luan, D.; Madhavi, S.; Boey, F. Y. C.; Archer, L. A.; Lou, X. W. *J. Am. Chem. Soc.* **2010**, *132*, 6124.

(34) Liu, S. W.; Yu, J. G.; Jaroniec, M. *Chem. Mater.* **2011**, *23*, 4085.

(35) Linsebigler, A. L.; Lu, G. Q.; Yates, J. T. *Chem. Rev.* **1995**, *95*, 735.

(36) Anpo, M.; Che, M.; Fubini, B.; Garrone, E.; Giamello, E.; Paganini, M. C. *Top. Catal.* **1999**, *8*, 189.

(37) Butler, M. A. *J. Appl. Phys.* **1977**, *48*, 1914.

(38) Pan, J.; Wu, X.; Wang, L. Z.; Liu, G.; Lub, G. Q.; Cheng, H. M. *Chem.Commun.* **2011**, *47*, 8361.

(39) Inoue, T.; Fujishima, A.; Konishi, S.; Honda, K. *Nature* **1979**, *277*, 637.

(40) Hoffmann, M. R.; Martin, S. T.; Choi, W. Y.; Bahnemann, D. W. *Chem. Rev.* **1995**, *95*, 69.

(41) Ouyang, S. X.; Ye, J. H. *J. Am. Chem. Soc.* **2011**, *133*, 7757.

(42) Vittadini, A.; Selloni, A.; Rotzinger, F. P.; Gratzel, M. *Phys. Rev. Lett.* **1998**, *81*, 2954.

(43) Selloni, A. *Nat. Mater.* **2008**, *7*, 613.

Chapter 6 General Conclusion and Future Prospects

6.1 General Conclusion

In this thesis, the main goal is to design and develop advanced TiO_2 based materials for the superior photocatalytic properties via enhancing the light utilization efficiency, charge separation efficiency, and surface reactivity et al. The detailed study could be summarized as below:

1. A novel strategy of coupling Mie's scattering effect into the light absorption region of TiO_2 was developed to improve the light utilization efficiency. The scattering phenomenon has been applied in the DSSC before; however, to the best of our knowledge, it is the first time that we adopt this scattering effect into the photocatalytic H_2 evolution. In this study, TiO_2 spheres with different diameters (330-750 nm) were fabricated to investigate the correlation between the particle size and the scattering effect. Among those TiO_2 samples, the 380 nm sized TiO_2 exhibited the strongly efficient scattering effect in the light absorption region of TiO_2, thus leading to a higher light-utilization efficiency, followed with a considerable enhancement of the photocatalytic activity. This study provides a promising approach to effectively enhance the light utilization efficiency for other semiconductor photocatalysts, especially for the visible-light-driven photocatalysts with the optimized diameter.

2. To achieve better charge separation efficiency and CO_2 adsorption, porous-structured Cu_2O/TiO_2 nanojunction material was successfully prepared. The well-designed nanojunction structure can facilitate the charge separation between Cu_2O and TiO_2 in the CO_2 photoreduction; while the porous structure is beneficial for the CO_2 adsorption. Those combined properties endow the Cu_2O/TiO_2 nanojunction exhibits

marked photocatalytic performance in the CO_2 photoreduction tests. This study demonstrates that constructing of well-designed nanojunction into the porous-structured materials can not only largely enhance the charge separation efficiency but also facilitate the reactant adsorption, thus promote the photocatalytic performance in the potential application of environmental and energy fields.

3. Anatase TiO_2 nanosheets with 95% active {100} facets exposed and a relatively large surface area of 57.1 m^2/g were successfully prepared. This percentage (95%) is the highest among previously reported {100} facet exposed anatase TiO_2 so far. Due to the high ratio of {100} facets exposed as well as the large surface area, which can offer more active sites in the photocatalytic reaction, this sample showed marked photocatalytic activity in both H_2 evolution and CO_2 photoreduction. The present work motivates us to fine-tune the TiO_2 or other functional materials exposed with high percentage of active facets to achieve advanced and excellent properties.

4. For the first time, {111} facet exposed anatase TiO_2 single crystals were synthesized via both F^- and ammonia as the capping reagents. In comparison with the intensively investigated {001}, {100}, and {101} facets of anatase TiO_2, {111} facet owns a much higher surface energy of 1.61 J/m^2, in addition with the superior surface atomic structure and electronic configuration. Those superior surface properties make our prepared {111} facet exposed TiO_2 exhibit excellent photocatalytic properties in the H_2 evolution. This fundamental understanding shows that the facet control of semiconductors allows the optimization of both the surface atomic structure and electronic band structure, thus largely promotes the photocatalytic efficiency.

6.2 Future Prospects

6.2.1 TiO_2 Photocatalyst

TiO_2 is a typical environmental-friendly and high-stable photocatalyst, which has been practically used in Japan since the later 1990s.[1] For instance, the TiO_2-coated cleaning materials are used in the glass covers on highway tunnel[2] or window blinds of the building[3] to photo-decompose the adsorbed pollutants; the copper- and/or silver-deposited TiO_2 films[4] as antibacterial materials started full-scale manufacturing by TOTO Ltd. in 1995.[1] In addition, the photo-induced hydrophilicity markedly widened the application of TiO_2,[5] the photocatalytic exterior glass on which the stains adsorbed on the TiO_2 surface can easily be washed by water, with an area of 20,000 m^2, was installed in the terminal building of Chubu International Airport opened in 2005.[1] What's more, the anti-fogging function resulted from its photo-induced hydrophilicity can also be practically used in various glass products, such as eyeglasses and the side-view mirrors of the car.[1]

However, the wide band gap of TiO_2 limits that it only can absorb the light in the UV region, accounting for 5% of the solar spectrum. From the perspective of both chemistry and practical applications, it is undoubtedly important to develop the visible-light-driven photocatalysts. To achieve this goal, many strategies (including metal-ion[7] and nonmetal doping[8]) have been proposed to extend the light absorption of TiO_2 into the visible light region. However, the doped materials typically suffer from the thermal instability, photocorrosion, and fast e^--h^+ recombination rates.

Fortunately, the localized surface plasmon resonance (LSPR) photosensitization offers a new opportunity for the visible-light-driven photocatalysis. Particularly, when the semiconductor loaded with coinage metals (such as Au, Ag and Cu), it will exhibit visible-light activity. Those magic properties might be caused by the charge transfer

from photoexcited metal to the semiconductor and/or LSPR-induced electromagnetic fields in the vicinity of the plasmonic nanostructure.[9]

The metal loaded on the semiconductor can arouse the localized surface plasmon resonance (LSPR) photosensitization, which can not only make the photocatalyst visible-light-driven, but also can facilitate the O_2 evolution for TiO_2. The oxygen generation is frequently considered to be the bottleneck for the overall water splitting. Thermodynamically, it requires the holes having higher oxidation potential than 1.23 eV. When the metals (e.g. Au nanoparticles) are loaded on the TiO_2 particle, under the effect of the localized surface plasmon resonance (LSPR) photosensitization, Au/TiO_2 can evolve O_2 under visible light irradiation. Typically, metals are devoid of any oxidation activity. Nevertheless, small Au clusters (below 2 nm) can exhibit frontier HOMO/LUMO orbitals, and the holes in HOMO orbital can have higher oxidation potential than the larger Au particles. When the oxidation potential of those small Au nanoparticles fulfills the thermodynamic requirements (i.e. > 1.23 eV), the Au/TiO_2 could be able to oxidize water into oxygen.[10]

Therefore, to achieve the visible-light-driven photocatalysts, more attention should be paid on the localized surface plasmon resonance (LSPR) happened in the metal/TiO_2 in the future. Moreover, my PhD research is mainly focused on the H_2 evolution over TiO_2, the localized surface plasmon resonance (LSPR) effect happened in the metal/TiO_2 can also help me to further investigate the oxidation ability of the TiO_2 based materials.

6.2.2 CO_2 Photoreduction

CO_2 photoreduction is a promising solution to both the global warming and energy shortage. Recently, special attention has been paid on the photoreduction of CO_2 into

hydrocarbon fuels. In the investigation of the electrochemical CO_2 reduction, it is reported that the desired products can be selectively obtained by optimization of the electrocatalysts or the electrolytes.[11,12] The *sp* metals (e.g., Zn, Cd, Hg, In, Tl, Sn, Pb, and Bi) mainly generate formate in the aqueous conditions, while hydrocarbons are the main products with *d* metals (e.g., Pd, Pt, Cu, Ag, and Au); in addition, compared with the aqueous electrolyte, complex organic compounds (such as oxalic acid) are usually produced from the non-aqueous electrolytes in both electron configurations.[13] However, rarely scientific reports are focused on the selectivity of the semiconductor-based CO_2 photoreduction. Inspired by the results from the electrochemical CO_2 reduction, we anticipate that the selectivity of the products can also be achieved via varying the metal co-catalysts over our developed TiO_2 based materials. Therefore, the future study will mainly focus on the selectivity of the CO_2 photoreduction to meet the various demands of the human beings.

Reference:

(1) Hashimoto, K.; Irie, H.; Fujishima, A. *Japan. J. Appl. Phys.* **2005**, *44*, 8269.

(2) Watanabe, T.; Hashimoto, K.; Fujishima, A. *1st Int. Conf. TiO_2 Photocatalyst, ed. H. A1-Ekabi* **1992**.

(3) Honda, H.; Ishizaki, A.; Soma, R.; Hashimoto, K.; Fujishima, A. *J. Illum. Eng. Soc.* **1998**, 42.

(4) Sunada, K.; Watanabe, T.; Hashimoto, K. *Environ. Sci. Technol.* **2003**, *37*, 4785.

(5) Fujishima, A.; Hashimoto, K.; Watanabe, T. *TiO_2 Photocatalysis, Fundamentals and Applications (BKC, Tokyo)* **1999**.

(6) Asahi, R.; Morikawa, T.; Ohwaki, T.; Aoki, K.; Taga, Y. *Science* **2001**, *293*, 269.

(7) Choi, W.; Termin, A.; Hoffmann, M.R. *J. Phys. Chem.* **1994**, *98*, 13669.

(8) Asahi, R.; Morikawa, T.; Ohwaki, T.; Aoki, K.; Taga, Y. *Science*, **2001**, *293*, 269.

(9) Liu, L.Q.; Ouyang, S.X.; Ye, J.H. *Angew. Chem. Int. Ed.* **2013**, *52*, 1.

(10) Silva, C.G.; Juarez, R.; Marino, T.; Molinari, R.; Garcia, H. *J. Am. Chem. Soc.* **2011**, *133*, 595.

(11) Hori, Y.; Konishi, H.; Futamura, T.; Murata, A. Koga, O.; Sakurai, H.; Oguma, K. *Electrochim. Acta* **2005**, *50*, 5354.

(12) Azuma, M.; Hashimoto, K.; Hiramoto, M.; Watanabe, M.; Sakata, T. *J. Electrochem. Soc.* **1990**, *137*, 1772.

(13) Lee, J.; Kwon, Y.; Machunda, R.; Lee, H. *Chem. Asian J.* **2009**, *4*, 1516.

Acknowledgement

During the past few years, I have studied a lot, not only from the academic research, but also in my life. I am proud that I will become a PhD in the near future; I know this title means a lot. I sincerely appreciate everyone who gave me kind help during my study and daily life in Japan.

At first, I would like to express my great gratitude to my supervisor Prof. Jinhua Ye, who gave me this valuable chance to study in Hokkaido University. In my eyes, Prof. Ye is a great woman, teacher, and scientist. As a woman, she can handle the family affairs and work well; and she always encourages me when I meet difficulties. She sets a good example for all of the women who are willing to pursue the scientific study. As a teacher, she carefully instructs me how to do the research and give me valuable suggestions in the academic study. Besides study, she also teaches us how to raise a good character for the better prospects. As a scientist, she is concentrated on the photocatalysis; I am sincerely inspired by her serious scientific attitude, rigorous scholarship, and immense knowledge. Her warm encouragement, valuable instruction, and kind help support me to finish this dissertation.

I am also grateful to my supervisor Dr. Tetsuya Kako, who gave me lots of detailed and constructive suggestions on the basis of his immense knowledge in the photocatalysis field. Thank you very much for your every suggestions and kind help during my PhD study.

Then, I would like to thank all the members in the Catalytic Materials Group in NIMS. All of you are very friendly and pleasant. I wish to give thanks to Dr. Shuxin Ouyang, who gave me lots of kind instructions and selfless help in both study and daily

life. I also would like to thank Dr. Naoto Umezawa, Dr. Pakpoom Reunchan, and Dr. Hua Tong for your helpful suggestions in my academic study; and Mr. Takehiko Matsumoto, Dr. Yingpu Bi, Dr. Guangcheng Xi, Dr. Kui Xie, Dr. Lequan Liu, Dr. Qing Kang, Dr. Han Zhou, Dr. Xiaoqing Chen, Dr. Junyu Cao, Dr. Bing Yue, Dr. Peng Li, Dr. Ning Zhang, Mr. Zongwei Mei, Mr. Jianjun Guo, Mr. Xianguang Meng, Ms. Aya Hagino, Ms. Haruna Kurokawa, and Ms. Takako Tsubata, for your kind helps in both experiments and daily life.

At last, I would like to give my special thanks to my parents for their constant support and warm encouragement. They are always the driving force to push me forward.